THESIS FOR THE DEGREE OF LICENTIATE OF ENGINEERING

Grid Code Testing of Wind Turbines by Voltage Source Converter Based Test Equipment

NICOLÁS I. ESPINOZA R.

Department of Energy and Environment
CHALMERS UNIVERSITY OF TECHNOLOGY
Gothenburg, Sweden, 2015

Grid Code Testing of Wind Turbines by Voltage Source Converter Based Test Equipment
NICOLÁS I. ESPINOZA R.

Division of Electric Power Engineering
Department of Energy and Environment
Chalmers University of Technology
SE–412 96 Gothenburg
Sweden
Telephone +46 (0) 31–772 1000

Printed by Chalmers Reproservice
Gothenburg, Sweden, 2015

To my family and friends...

Grid Code Testing of Wind Turbines by Voltage Source Converter Based Test Equipment
NICOLÁS I. ESPINOZA R.
Department of Energy and Environment
Chalmers University of Technology

Abstract

Wind energy is expected to play a crucial role in the energy mix in the future society with limited access to fossil fuels. Wind turbines with larger power rating are being installed every year, making possible to extract more energy from wind. In countries where wind power has become a relevant part of the total generated electrical power production, transmission system operators (TSOs) have included in their grid codes specific technical requirements for interconnection of wind power plants. Today, grid code requirements are tested by using an impedance-based testing equipment which is limited to voltage dips and swells. For this reason, many of the requirements remain unverified. The use of fully controllable converter systems operated as test equipment allows for a wide variety of tests that can be carried out on the generating unit. For this reason, a different approach of grid code testing methodology is investigated in this thesis.
The investigated testing setup consists of a 4 MW wind turbine and an 8 MW testing equipment constituted by a set of voltage source converter (VSC) in back-to-back configuration. In particular, this thesis focuses in the Low Voltage Ride Through (LVRT) test of full-power converter (FPC) wind turbines. In this work, a detailed description of the technical requirements included in grid codes for interconnection of the wind power plant with the grid is given. The control algorithm that governs both the testing equipment and the wind turbine are derived in detail, with special focus on the control scheme of each VSC. The risk for poorly damped resonances and possible interaction between the testing equipment and the tested object is investigated through small signal analysis. The grid code testing methodolgy is then validated through time domain simulation where all the sub-systems that constitute the testing setup are integrated in one simulation model. The obtained results demonstrate the flexibility of the proposed approach in controlling the voltage at the wind turbine terminals, including the ability in emulating the short-circuit impedance of the grid at the connection point. Furthermore, laboratory experiments are carried out in order to verify the investigated methodology. Finally, field test of the actual testing facility in Gothenburg, Sweden are included in this thesis.

Index Terms: Grid Codes, Wind Power, Low Voltage Ride Through (LVRT), Voltage Source Converter (VSC), Discrete Control, Grid Emulation.

Acknowledgments

This work has been carried out within the Swedish Wind Power Technology Centre (SWPTC). The financial support provided by the academic and industrial partners including the Region Västra Götaland and the Swedish Energy Agency is gratefully acknowledged.

I would like to express my deepest and sincere gratitude to my supervisor Professor Massimo Bongiorno and my examiner Professor Ola Carlson fort their professional guidance, encouragement and invaluable help throughout the research work. I am also grateful to Sara Fogelström for her administrative support within the SWPTC. Special thanks to Massimo for his support in supervising and correcting this manuscript.

My acknowledgment to the members of ABB Corporate Research Center, especially Luca Peretti, Ville Sarkimaki, and to GE Global Research members Emad Ahmed and Christof Sihler for sharing their experience with me and for providing valuable data used in this model. I would like to thank Michael Lingren and Per Hjalmarsson (PROTOL) and Niklas Almgren and Christer Pettersson (Göteborg Energi) for their support in providing experimental data used in this thesis.

I take this opportunity to express my gratitude to all my colleagues at the Department of Electric Power Engineering at Chalmers for their friendship and good fika-times, especially to Georgios Stamatiou, Joackim Härsjö and Gustavo Pinares for the fruitful discussion and for their inputs in this project. Special gratitude to Pinar, Pavan, Pramod and Daniel for their company, their friendship and good support during this project. I would like to thank my friends Tomás and Giuseppe for their good friendship and support, as well as my friends Diego and Carlos who are in Chile.

Finally, my warm gratitude to my family for their love and encouragement, with special thanks to my beautiful and beloved fiancée Paola.

Sincerely,

Nicolás I. Espinoza R.
Gothenburg, Sweden
August, 2015

Preface

The Swedish Wind Power Technology Centre (SWPTC), placed at Chalmers University of Technology in Gothenburg, Sweden, focuses on developing knowledge of the design of wind turbines and optimizing maintenance and production costs.

One of the objectives of the Centre is to supply the industry with in-depth know-how within the field of wind power. Specific projects are being carried out within the Centre regarding the following topics: power and control system, turbine and wind load, mechanical power transmission and system operation, structure and foundation, maintenance and reliability, and operation in cold climate. Other research projects at Chalmers University of Technology are related to semiconductors and converter topologies and control for renewable energy sources.

Moreover, the wind turbine is seen as a complete system. Therefore, there is a strong co-operation between the mechanical, electrical and control departments within the University and the Centre. By integrating education, research and innovation, the Centre hope to contribute with competence, knowledge and experience that today's industry needs.

This project is part of Theme Group 1: Power and Control Systems.

SWPTC's work is funded by the Swedish Energy Agency, by three academic and thirteen industrial partners, including Göteborg Energi, ABB and General Electric. The Region Västra Götaland also contributes to the Centre through several collaboration projects.

Publications

1. N. Espinoza, M. Bongiorno and O. Carlson, "Grid Code Testing of Full Power Converter Based Wind Turbine Using Back-to-Back Voltage Source Converter System," in EWEA 2013 Annual Event Conference Proceedings. Feb. 2013.

2. Espinoza, N.; Bongiorno, M.; Carlson, O., "Novel LVRT Testing Method for Wind Turbines Using Flexible VSC Technology," *Sustainable Energy, IEEE Transactions on* , vol.6, no.3, pp.1140-1149, July 2015

List of Acronyms

IG	Inductor Generator
VSC	Voltage Source Converter
FPC	Full Power Converter
DFIG	Doubly-Fed Induction Generator
WT	Wind Turbine
TE	Testing Equipment
TSO	Transmission System Operator
PCC	Point of Common Coupling
LVRT	Low Voltage Ride Through
EWEA	European Wind Energy Association
SWPTC	Swedish Wind Power Technology Centre
FACTS	Flexible AC Transmission System
STATCOM	Static Compensator
HVDC	High Voltage Direct Current
HV	High Voltage
MV	Medium Voltage
LV	Low Voltage
LC	Inductive Capacitive
IGBT	Insulated Gate Bipolar Transistors
LPF	Low-Pass Filter
PWM	Pulse Width Modulation
OL	Open Loop
CL	Close Loop
PI	Proportional Integral
P	Proportional
PLL	Phase Locked Loop
IMC	Internal Model Control (IMC)

Contents

Chapter 1

Introduction

1.1 Background and motivation

Wind energy is a renewable source of energy that plays a key role towards a sustainable future. Wind parks are today being installed in large scale in many countries, while wind turbines with larger and larger power ratings are being produced every year. Among other factors, the reliability of the electrical grid depends on how well the generating units are prepared to withstand a grid fault. In the specific case of integration of renewable energy sources, transmission system operators (TSO) have included in their grid code specific technical requirements for interconnection of wind power plants with the electricity grid.

In general words, grid code specifies how a generating plant should behave during normal and abnormal condition. The continuous increase of electrical energy from wind power in the power system has lead TSOs to impose more and more stringent requirements. For instance, requirements for steady-state voltage and frequency range are given in a detailed manner. In addition, typical system disturbances such as voltage dip are specified in terms of retained voltage and duration, requiring that the generating plant should withstand them without disconnecting from the grid. Disconnection is possible in extreme cases and just when it is permitted by the grid code. In this regard, a wind turbine manufacturer has to ensure a safe operation of the wind farm and the grid by fulfilling all the technical requirements for interconnection. Moreover, the requirements are always a design criterion, thus, manufacturers are involved when reviewing these requirements with the authority. For this reason, it is crucial to develop testing methodologies for this type of technology in order to ensure a correct integration of wind energy into our actual electricity grids.

To evaluate the capability of the wind turbine to withstand grid disturbances, today tests are performed on the generating unit by using an impedance-based voltage dip generator. By developing further new testing methodologies, it will be possible to test for grid scenarios other than voltage dip, ensuring a reliable and fault-tolerant operation of the wind turbine system.

Furthermore, in the future, wind turbines will be required to participate more actively in the regulation of the grid. It is a common believe that standards and grid codes will contemplate a

wide variety of new requirements addressing a reliable operation of the wind power plant. Smart control algorithms will allow them to behave as any conventional energy source in terms of inertia, power oscillation damping and voltage/frequency support of the grid, contributing to the overall stability enhancement of the power system.

1.2 Purpose of the thesis and main contributions

The objective of this work is to develop methods for grid code testing of wind turbines using Voltage Source Converters (VSC) system. In this thesis, different grid codes have been analysed and specific technical requirements for interconnection of wind parks with the electricity grid have been identified. This study has been focused on the control and operation of VSC for its use in testing of wind turbines systems. Moreover, simulation of the complete testing system including a full power converter (FPC) based wind turbine model and the VSC-based testing equipment have been carried out. Here, the VSC will emulate different grid situations according to the grid codes.

The main contribution of this work is the analysis of the use of VSC-based testing equipment for grid code testing of wind turbine systems. With focus on FPC-based wind turbine, a mathematical model has been developed and computer simulations, laboratory experiment and filed test has been carried out. The results from this work has been used to evaluate the proposed methodology of testing. Finally, part of these results has been published in two scientific papers.

1.3 Structure of the thesis

In this thesis, a brief review of the development of wind power installation, including the interconnection of wind power plants with the electricity grid and the description of the most common wind turbine topologies is given in Chapter 2. In Chapter 3, a detailed description of the technical requirements included in grid codes for normal and faulty condition of the grid is given. Moreover, the methodology for testing wind turbine is also introduced in this chapter. Chapter 4 shows in detail the modelling and implementation of the VSC-based testing equipment and its control algorithms, including PCC voltage control and short-circuit impedance emulation. The modelling of the FPC wind turbine, including crow-bar protection and control strategy during fault, is also described here. In Chapter 5, the stability of the testing setup is analysed through sensitivity analysis. Here, the system-pole location is investigated against the variation of system parameters and control settings of both the testing equipment and the wind turbine. In Chapter 6, the investigated grid code testing methodology is validated through simulations. Laboratory experiments and field test results are also given in this chapter. Finally, in Chapter 7 it is given the conclusions as well as interesting ideas that need further investigation.

Chapter 2

Wind energy systems

2.1 Introduction

Wind parks are today being installed in large scale in many countries. Moreover, wind turbines with greater power are being produced every year, making possible to extract more energy from wind [1].

From a global perspective, the total installed wind power in the world in 2013 is 318 GW, growing with an average rate of 40 GW per year in the last 5 years. The main players are China, USA and western Europe. China has the biggest wind power installation in the world with 91 GW, behind USA and Germany with 61 GW and 34 GW installed, respectively. Spain posses 23 GW of wind capacity, followed by India with 20 GW and UK with 10 GW of wind power capacity [2].

Statistics data from the European Wind Energy Association (EWEA) [3] suggest that from year

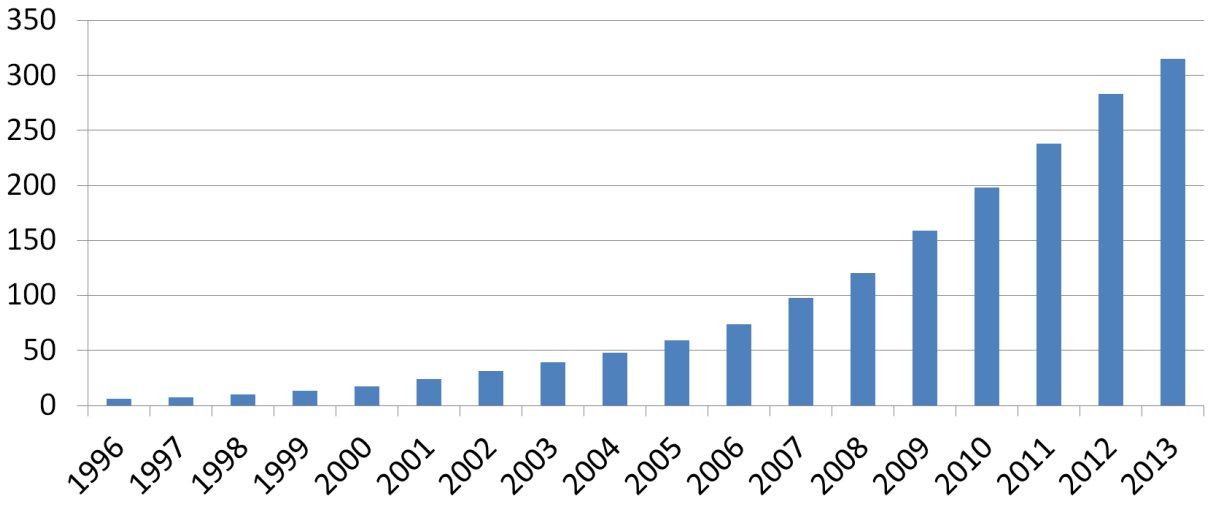

Fig. 2.1 Cumulative world installed wind capacity (values in GW per year) [3].

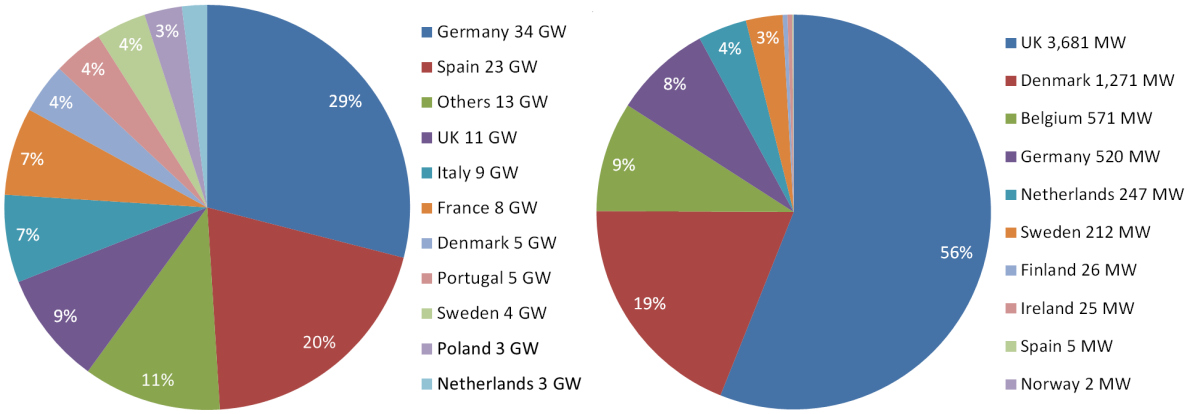

(a) (b)

Fig. 2.2 Share of the (a) total [3], and (b) off-shore [4] installed wind power capacity in EU in 2013.

2000 to 2012, the installed wind power capacity in Europe has increased from 12.9 GW to 117.3 GW, with a sustainable growth of approximately 10 GW per year [3].

In Fig. 2.2(a) is shown the total shared capacity among the European countries. Observe that nearly 50% of the total installed capacity is placed in Germany and Spain. Moreover, United Kingdom (UK) posses 9% of the total share. The remaining 42% is shared among the rest of the EU countries.

In particular for off-shore wind energy, with reference to Fig. 2.2(b), the largest capacity is installed UK with 56% of the total off-shore installed capacity, followed by Denmark with 19% of the share, Belgium with 9% and Germany with 8%.

There are 5.538 MW of off-shore wind energy capacity installed world-wide, 90% of which is in Europe, making the region by far the world leader in offshore wind. At the end of 2012, 509.5 MW of off-shore wind energy capacity was installed in China, mainly in shallow intertidal areas, and 33.8 MW in Japan, mostly near-shore [5].

2.2 Wind turbine systems

The increasing use of wind energy pushes the development of wind turbine systems in size and technology [1]. Wind turbines are mainly classified in fixed-speed and variable-speed operation. In the following, a brief description of wind turbine topologies is presented.

2.2.1 Fixed-speed wind turbine

A typical diagram of a fixed-speed wind turbine is given in Fig. 2.3. The induction generator (IG) is connected to the grid by a coupling transformer. The rotor of the IG can be either squirrel-cage or wounded type. The latter offers the possibility to access the rotor terminals and provide control over the rotor currents by the use of passive components or power electronics. Depending of the

poles in the stator, the rotor shaft can rotate at a nominal speed of 1000 rpm or 1500 rpm. For this reason, the wind turbine blades and hub are connected to the generator shaft by a step-up gearbox [6].

The fixed-speed wind turbine is a simple system in which the mechanical power is transformed into electrical power by means of a directly-connected IG. The applied stator voltage can be regulated by a series soft-starter, depicted in Fig. 2.3, when starting-up the IG. This is done by controlling the series thyristor in the soft-starter, and thereby limiting the inrush current. During normal operation of the wind turbine the soft-starter is bypassed [6].

Given the inductive nature of electrical machines, the IG consumes a significant amount reactive power during normal operation. This is not only related to the magnetization of the iron core, but also with the increasing of the speed and thus with the active power output. For this reason, a capacitor bank can be use to provide reactive power compensation, improving the power factor when interconnecting the wind turbine with the grid [8].

The direct coupling of the IG with the grid presents a number of disadvantages, especially during grid disturbances. For instance, when a sever grid fault occurs resulting in a low retained voltage at the terminals of the wind turbine, large fault current can be experienced due to the sudden demagnetization of the core. This event can activate the protection system, disconnecting the wind turbine from the grid. For this reason, the fulfilment of grid codes is a challenge for this kind of generating units; especially when disconnection of the wind farm, depending of the magnitude and duration of the voltage dip, might not be allowed by the TSO [9], [10], [11]. Finally, the narrow speed window where wind energy extraction is optimal is strictly related on the reduced slip range of the IG. Thus, mechanical stress across the turbine structure can be produced when coping with wind speed fluctuations. Therefore, the fix-speed wind turbine is less efficient in producing electrical power, as compared with variable-speed wind turbines [6].

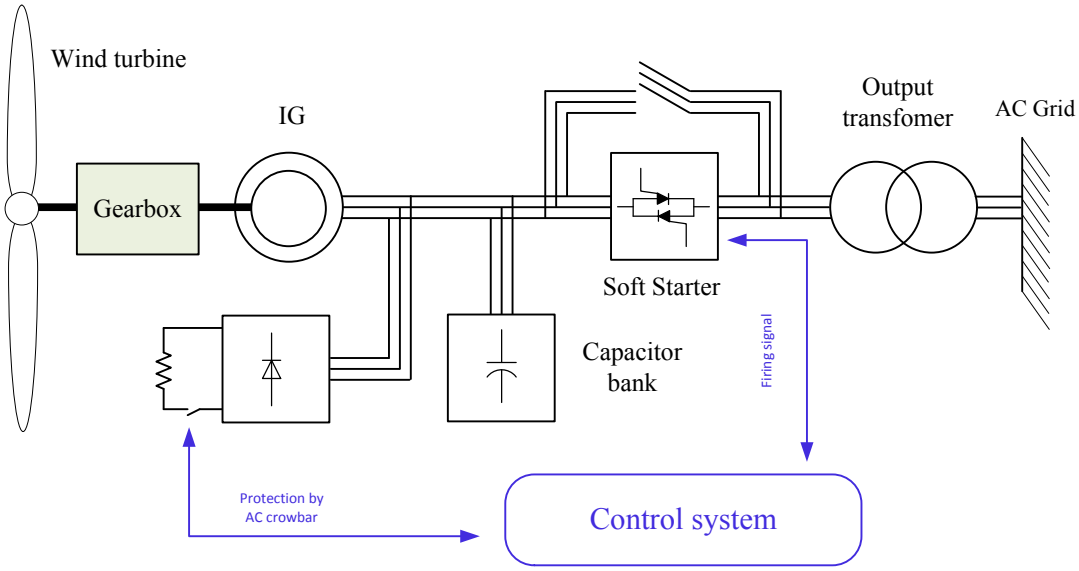

Fig. 2.3 Schematic representation of a fixed-speed wind turbine given in [7].

2.2.2 Doubly-Fed Induction Generator wind turbine

A typical scheme representation of the Doubly-Fed Induction Generator (DFIG) wind turbine is given in Fig. 2.4. The stator of the IG is usually a four-pole system [8], where the terminals of the stator are connected with the grid through a three-winding transformer. The rotor windings are accessible via slip rings and brushes, where a back-to-back VSC is connected. The grid-side VSC is connected to the low voltage (LV) side of the coupling transformer. The medium voltage (MV) side of the transformer can be either connected to the grid, or to a dedicated AC collector bus.

The use of the bi-directional VSC enables the absorption or injection of rotor currents. The VSC is typically rated 20% to 30% of the wind turbine power [12], meaning that one third of the power can circulate through the rotor circuit. This feature opens up the speed range operation of the wind turbine, as compared of the fixed-speed wind turbine described in Section 2.2.1. With the introduction of variable-speed operation of the IG, the turbine can extract energy from the wind more efficiently for a wider range of wind speed. In addition, it allows for a more precise control of the torque across the drive train, avoiding high mechanical stress [6].

Depending of the operation mode of the DFIG wind turbine, i.e.: sub-synchronous mode or super-synchronous mode, the power flow throughout the back-to-back VSC can be either toward the rotor or toward the grid [12]. Moreover, the speed of the turbine is controlled by the rotor-side converter by means of controlling the active current that flows in the rotor windings. The rotor-side converter also provides the reactive power needed for magnetizing the DFIG. Similarly, the

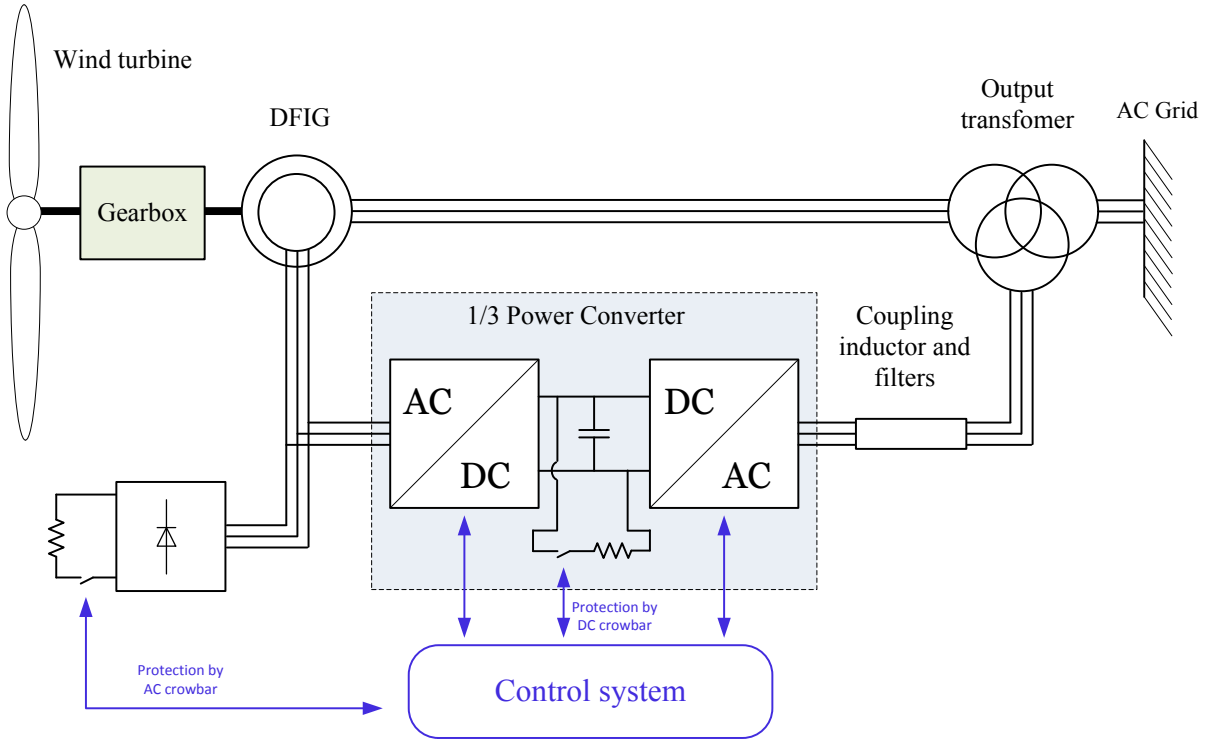

Fig. 2.4 Schematic representation of a DFIG wind turbine given in [7].

reactive power output of the wind turbine is controlled by the reactive current that is exchanged in the rotor windings.

The control structure of the grid-side converter is usually constituted by a speed or torque controller and a reactive power controller in cascade with an inner current control [13]. The valves of the VSC can be operated either by using Pulse Width Modulation (PWM) or by hysteresis control [12]. Similarly, the grid-side converter controls the DC-link voltage by exchanging active power with the grid. The control structure of the grid VSC is constituted by a DC voltage control in cascade with a current control [13]. The valves of the converter are also operated with PWM [12].

When a grid fault occurs resulting in a low voltage at the terminals of the wind turbine, the grid-side converter cannot inject the produced power into the grid without exceeding nominal current. Observe that power electronic devices are very sensitive to damage when an over-current is experienced [12]. In this scenario, the excess of energy produce by the turbine that cannot be delivered is then accumulated in the DC-link capacitor. When the instantaneous voltage exceeds a certain threshold, an over-voltage protection activates the DC crowbar, redirecting the generated power into a resistor. Through this protective action, the DC voltage is controlled within a safe margin. In a more severe event in which a DC-crowbar protection is not enough to burn the excess of energy produced i.e.: a voltage dip with an extremely low retained voltage at the terminals of the DFIG wind turbine; an extra degree of protection can be achieved by the use of a diode-rectifier based AC-crowbar at the terminals of the rotor circuit [12], as shown in Fig. 2.4. Similarly, an over-current protection activates the power electronic switch, when the rotor current exceeds the nominal current of the converter. The rotor windings are short-circuited and the additional rotor energy is dissipated in an resistor at the DC side of the rectifier [6], [13]. Finally, voltage support capabilities of a DFIG wind turbine can be enhanced by two set of actions: the grid-side VSC can be able to inject small amount of reactive power, if it is dimensioned accordingly; the rotor-side VSC can over-excite the rotor circuit increasing the magnitude of the back-EMF of the DFIG, thus, injecting reactive power into the grid through the stator circuit [12]. These protection and control measures enhances the LVRT capability of the DFIG wind turbine, allowing it to comply with actual grid codes (described later in Chapter 3).

2.2.3 Full power converter wind turbine

In a FPC wind turbine, the generator is connected to the grid through a full-power rated VSC in back-to-back, as depicted in Fig. 2.5. This configuration allows for an improved fault-tolerant capability of the wind turbine, as compared with the DFIG, avoiding severe transients in the generator when a grid fault occurs. Moreover, the grid-side converter of an FPC wind turbine can be designed and controlled in order to provide additional reactive power support, without having the need of over-magnetizing the generator core. However, the use of a fully rated power electronic interface increases the switching losses as compared a DFIG wind turbine [8].

As depicted in Fig. 2.5, a gearbox is typically used to step-up the rotational speed when coupling the wind turbine hub with the generator shaft. For a direct drive configuration i.e.: absence of the gearbox in the drive train, a dedicated low-speed multi-pole generator must be used in order

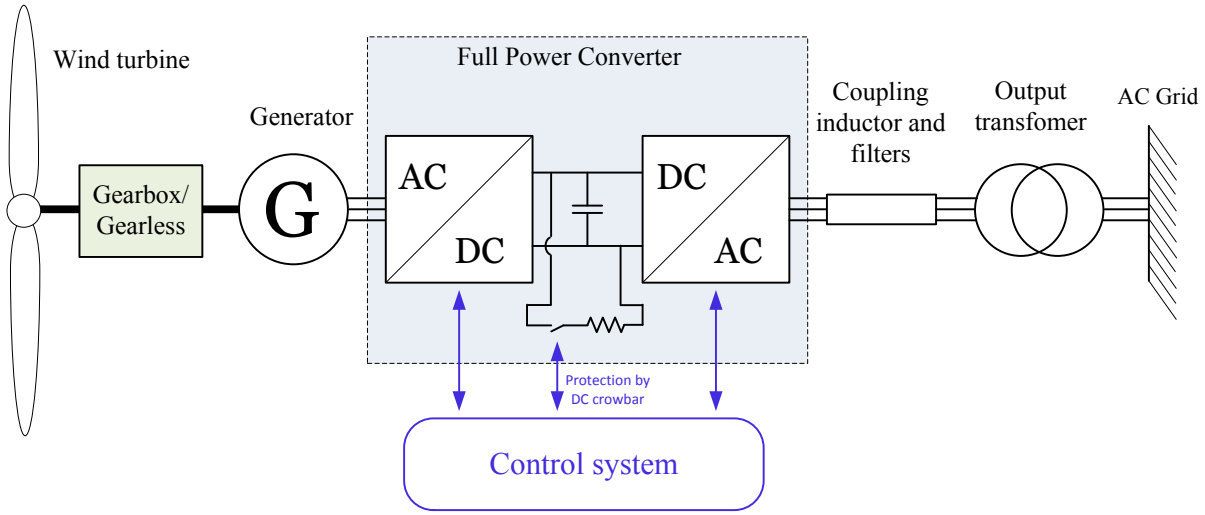

Fig. 2.5 Schematic representation of a FPC wind turbine given in [7].

to achieve the desired nominal frequency in the stator terminals. A filtering stage between the generator and the VSC can be used to reduce high-order transient in the generator current [8].

During normal operation of the wind turbine, the generator is fully decoupled from the grid as both VSC are connected in back-to-back configuration. The generator-side VSC is usually operated in torque control mode or speed control mode allowing the generated power to be injected into the DC-link [8]. The grid-side VSC controls the DC-link voltage by injecting active power into the grid. In addition, if reactive power exchange is allowed by the TSO, the grid-side converter can be operated either in voltage control mode or reactive power control. Finally, the wind turbine is grid-interfaced by using a step-up coupling transformer which increases the voltage from generator-level in LV to distribution-level in MV.

The use of fully rated back-to-back VSC for grid interconnection of wind turbine generators allows for a fast response during abnormal condition of the grid [14], [8]. For instance, during a voltage dip, the generated power cannot be delivered into the grid due to the absence of sufficient grid voltage. In this scenario, the grid-side-converter can quickly control the current output, avoiding feeding fault currents of large magnitude into the grid. Similarly, the generator-side converter provides quick control over the generator currents, preventing a possible overcharge of the DC-link capacitor. However, the latter method can produce undesired mechanical stress in the drive train.

Finally, the DC-link capacitor is protected by a DC-crowbar constituted by a parallel resistor and a power electronic switch. When the DC-link voltage exceeds a certain threshold, the excess of energy stored in the DC-link capacitor is redirected into a crowbar resistor, providing a fast protection during DC overvoltages. Further explanation of operation and control of the the FPC wind turbine is given in Chapter 4.

2.3 Wind power plants

A wind power plant (also called wind park or wind farm) is an arrangement of several individual wind turbines connected to the AC grid through a collector bus. The interconnected generating units are controlled by a main wind farm controller, which controls the active and reactive power set point of the whole generating plant. The wind park can be placed either on-shore as depicted in Fig. 2.6, or off-shore. The point of common coupling (PCC) is defined by the TSO as the first mesh connection point of the wind power plant with the electricity grid [15].

On-shore wind farms are grid-interfaced by using a common collector system in which the MV terminals of the wind turbine are connected. As depicted in Fig. 2.7, the collector bus is interfaced with the grid by using a high-power step-up transformer. The HV-side of the transformer is connected to the transmission system. Finally, the grid connection point of the wind plant is where the PCC is denoted.

Off-shore wind farms can be interconnected via AC submarine transmission lines, or by High Voltage Direct Current (HVDC) interconnection systems, enabling bulk energy transfer across

Fig. 2.6 Example of an on-shore wind farm located in Falkenberg, Sweden.

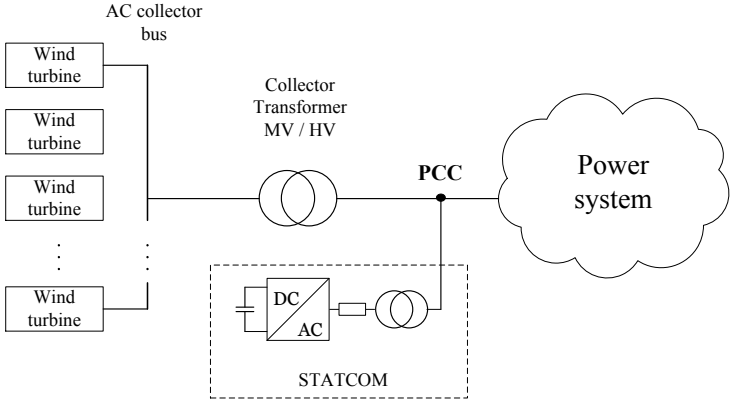

Fig. 2.7 Diagram representation of an on-shore wind farm.

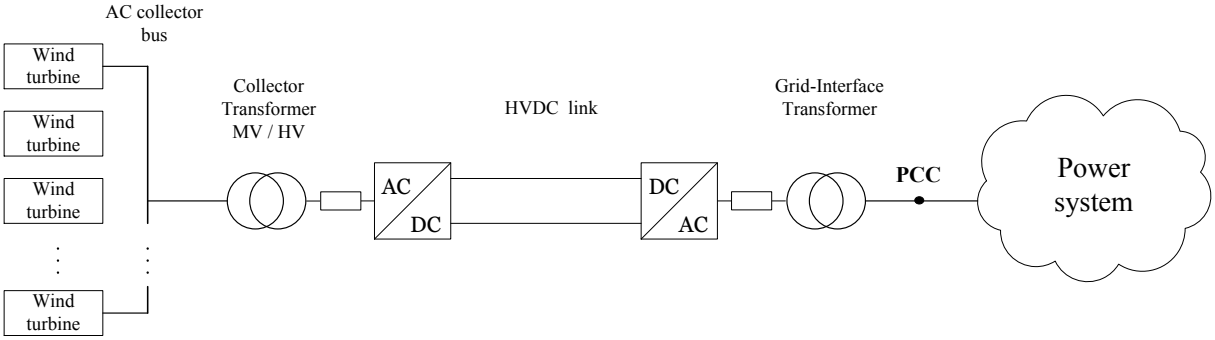

Fig. 2.8 Diagram representation of an off-shore wind farm.

long distances, as depicted in Fig. 2.8. The wind turbines are connected to an AC collector bus in MV level. Similarly, a high-power step-up transformer is used to interface the collector bus with the HVDC-VSC terminals. The grid-side VSC of the HVDC is interfaced with the AC transmission system by means of a high-power coupling transformer. The PCC is defined in its secondary side. Finally, in order to comply with power factor and voltage support requirements at the connection point with the grid, a Static Compensator (STATCOM) can be used in order to inject and absorb reactive power when needed [16]. An example of the connection layout of a STATCOM and an on-shore wind farm is included in Fig. 2.7.

2.4 Conclusions

In this chapter, the world wind energy scenario has been briefly discussed, with special focus on onshore and offshore wind power installations. In addition, three main topologies of wind turbine systems have been described. Finally, the schematic for interconnection with the electricity grid of onshore and offshore wind power plants has been introduced. In the following, an analysis of the selected European grid codes is given.

Chapter 3

Grid code analysis

3.1 Introduction

In grid codes it is specified how a generating plant should behave under both continuous and dynamic condition of the grid while maintaining a safe and reliable operation. Moreover, requirements for voltage, power and frequency operation range are given in a detailed manner. In addition, typical system disturbances are specified, so the generating plant should withstand them without disconnecting from the grid. In extreme cases, disconnection is also possible when it is allowed by the TSO.

When grid code applies specifically to wind parks, the wind turbine manufacturer have to ensure a safe operation of the wind farm by fulfilling all the technical requirements for interconnection of the generating plant. The requirements that cannot be tested experimentally are verified through software-aided simulation platforms.

In the following, an analysis of grid interconnection requirements included in the selected grid code is given and grid code testing devices are introduced.

3.2 Grid code selection

The grid codes considered in this thesis refer to countries that have high penetration of wind power into their national grid [3]. Consequently, these countries have developed detailed technical requirements for grid interconnection of wind power plants [9].

With focus on voltage and frequency operation band, voltage and reactive power dependencies, active power curtailment and LVRT requirements, the selected grid codes are: the German (E.ON) [17], [18]; British (National Grid) [19]; Spanish (REE) [20]; Irish (EirGrid) [21]; Danish (Energinet.dk) [22], Swedish (SvK) [23]; Nordic Countries (Nordel) [24]; and European grid code (ENTSO-E) [25].

A comparison of the different grid codes regarding interconnection of wind parks is given in [9], [10], [11] and [26]. A dedicated analysis of the German grid code is given in [27]. Finally,

control strategies developed for meeting grid code technical requirements have been documented in [13], [16] and [28].

In this chapter, the main focus of the grid code analysis is on the requirements during fault condition of the grid i.e.: comparison of different LVRT and requirements for grid support during a voltage dip. In the following, requirements for normal and abnormal operation of the grid will be briefly described; thus, requirements for fault condition of the grid will be presented.

3.3 Requirements during steady-state operation of the grid

The requirements for steady-state operation of the grid can be mainly categorized in three groups: reactive power requirements for normal voltage operation range; reactive power requirements during nominal active power production; and minimum operation time during long-term frequency deviations with active power curtailment. In the following, these three requirements are briefly explained.

3.3.1 Voltage and reactive power dependencies

A TSO can require reactive power injection from the wind farms to support overall system voltage control during normal operation. Usually, reactive power requirements are delimited inside a minimum power factor range that goes from 0.95 leading to 0.95 lagging for an active power set point between 0.05 pu and 1 pu; and within a nominal voltage that varies with a maximum deviation of ± 0.05 pu. A detailed grid code analysis conducted in this investigation is given in [9] (see Publication I).

3.3.2 Active and reactive power dependencies

Reactive power requirement are also dependent of the active power production of the wind farm. For instance, the Danish grid code states dependencies between voltage and reactive power, and between active and reactive power production [9]. Both requirements shall be complied simultaneously during normal operation of the wind farm. Moreover, reactive power injection can be controlled by either using a voltage control or power factor control. An extra option to define the reactive power production is to manually set the operating point. Remote control of reactive power allows TSO to control the voltage at a distance node, and in general, to control the total reactive power production of an entire grid [10].

3.3.3 Voltage and frequency dependencies

In grid codes, it is specified the steady state frequency and voltage operation range in which the wind turbine should operate continuously. Normal condition is considered for voltages close to 1.0 pu and frequency around 50 Hz, with deviation of approximately ± 0.05 pu of voltage

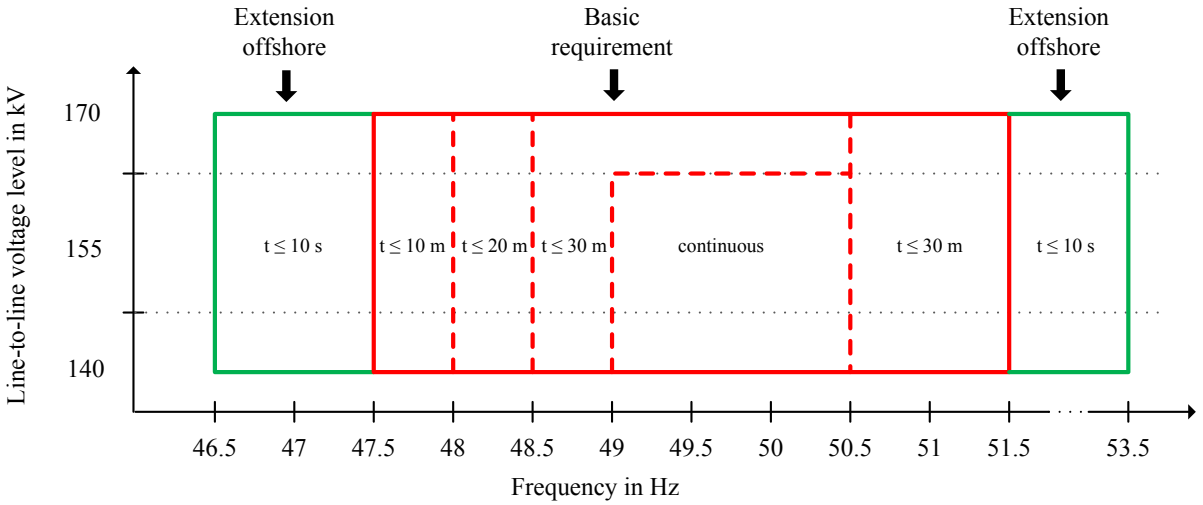

Fig. 3.1 Voltage-frequency requirements enforced by the German (offshore) grid code [18].

and ± 0.5 Hz of frequency, respectively. Any steady-state grid condition outside these values is defined with a minimum operational time, as shown in Fig. 3.1, and in some cases, followed by a control action for active or reactive power from the wind turbine side (explained in the following point), as enforced by the Danish [22], Irish [21] and German [17], [18] TSO.

3.3.4 Active power curtailment during frequency deviation

Frequency deviations can occur when the overall active power production does not match with the overall power system load. An increase of the system frequency is produce by a surplus of the instantaneous active power production compared to the demand of active power of the grid. This contingency occurs for instance, when a distant load suddenly is disconnected from the power system due to a fault in the grid. In the other hand, if a generation plant is disconnected, the frequency drops due to the surplus of the demanded active power.

When active power curtailment is demanded by the TSO in case of frequency deviations, the generation unit must vary its active power output in order to contribute to the overall regulation of the system frequency. In this case, a droop control strategy must be used when the frequency starts to deviate away from a specific dead-band, according to the characteristics given in the specific grid code. The active power variation are described as follows: active power must be increased if the system frequency drops from the dead-band, and active power must be reduced if the frequency increases above the dead-band. In a severe case scenario where the system frequency is outside the frequency operation band, the generating plant must disconnect.

An analysis on active power curtailment requirements is given in [9]. A well-documented strategy for frequency control is given in the Irish grid code [21], in the Danish grid code [22] as well as the German grid code for onshore and offshore wind turbines (references [17] and [18] respectively).

3.4 Requirements during dynamic condition of the grid

In this section, the interconnection requirements during dynamic condition of the grid are introduced. Here, the main focus is on the analysis of the requirement for LVRT and in voltage support in case of a grid fault.

3.4.1 Low voltage ride through requirements (LVRT)

In every grid code it is specified a voltage dip profile that the wind turbine should ride through without tripping. An exhaustive comparison of LVRT profiles is given in [10]. LVRT profiles characterization in terms of fault time, retained voltage and recovery ramp rates can be found in [11]. In Fig. 3.2 is shown a combination of the strictest LVRT profiles among the selected grid codes. In particular, the European grid code ENTSO-E [25] defines the guidelines to establish the LVRT profiles in each network inside EU. The requirements specified by ENTSO-E are enforced together with the local grid code.

When it is specified in the grid code, wind parks are required to support voltage restoration by injecting reactive power into the grid. In particular, the generating plant must provide voltage support by injecting a specific amount of reactive current during a voltage dip. For example, the Danish grid code [22] enforces a specific LVRT with retained voltage of 0.2 pu per 500 ms, as shown in Fig. 3.2, and demands for reactive power support during voltage restoration. Reactive current must be injected when voltage deviates below 0.9 pu. When the system voltage is lower than 0.5 pu, nominal reactive current injection must be reached. Active power production must be restored within 5 seconds after full recovery of the voltage within normal operation range. A graphical representation of the reactive power requirement during a LVRT event is given in Fig. 3.3.

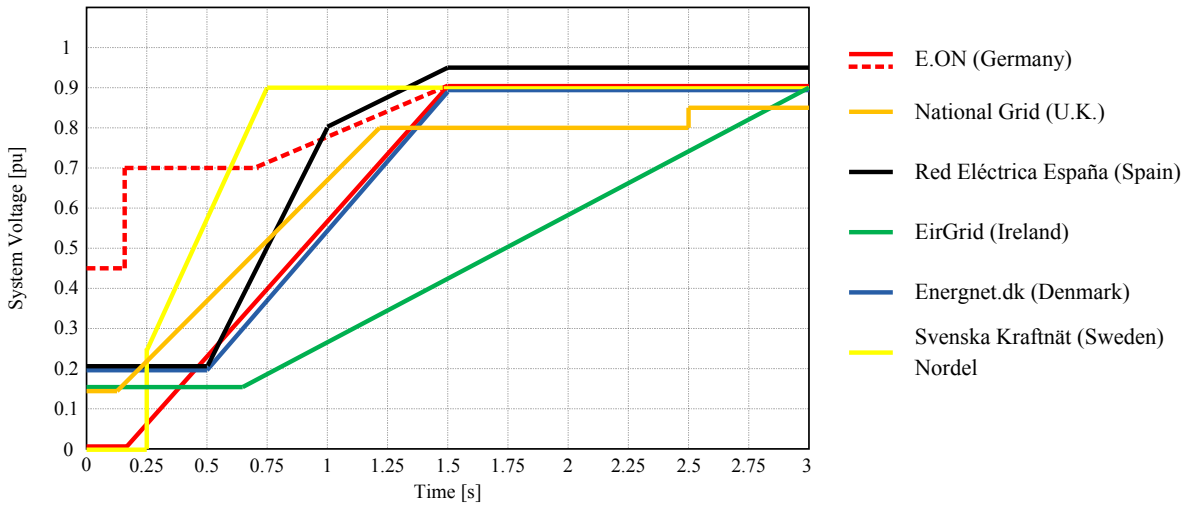

Fig. 3.2 Example of LVRT profiles from the selected grid codes.

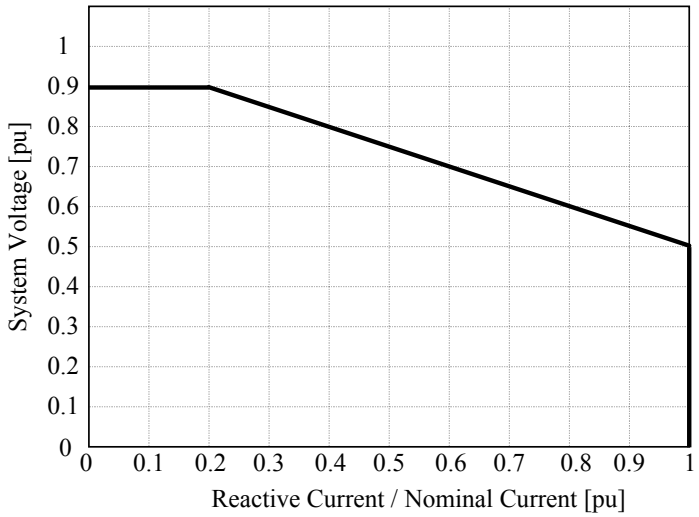

Fig. 3.3 Reactive power requirements during LVRT evet enforced by the Danish grid code [22].

According to the German grid code [17], an automatic voltage control must be activated within 20 ms if the grid voltage deviates more than 0.1 pu, and it must inject at least a reactive current of 0.02 pu for each percent of voltage deviation, as depicted in Fig. 3.4. For offshore wind farms [18], the voltage control must be activated at the PCC when grid voltage deviates 0.05 pu from its nominal value. Full reactive power output must be achieved when voltage drops more than 0.5 pu, similarly to the Danish grid code. After fault clearance, the automatic voltage control must still be active for another 500 ms after returning of the voltage within the normal operation band, in order to compensate for any voltage variation due to the action of an automatic

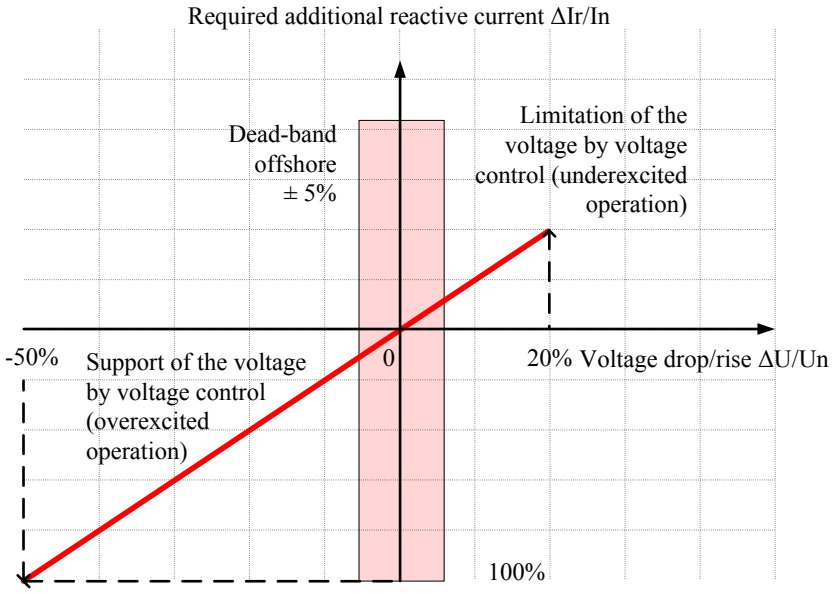

Fig. 3.4 Reactive power requirements during LVRT evet enforced by the German (onshore) grid code [17].

reclosure on an uncleared fault. Finally, the pre-fault set point of active power production must be reached with a gradient of at least 0.2 pu per second after returning of the voltage within the normal operation range.

A strict LVRT profile is defined in the Irish grid code [21], which enforces a minimum retained voltage of 0.15 pu for 650 ms, followed by a voltage recovery ramp for 3 seconds. During the voltage dip, the wind farm shall provide active power in proportion to retained voltage while maximizing reactive current injection into the grid, for at least 600 ms or until the voltage recovers to its normal operational range. In addition, the wind farm must be able to reach 90% of its available active power production within one second after total voltage recovery. The Irish grid code enforces reactive current injection of 0.04 pu, per each percentage of voltage drop when the voltage is lower than 0.9 pu. Maximum reactive power should be injected when the voltage drops below 0.75 pu.

The Swedish grid code [23] defines a retained voltage value of 0 pu for 250 ms, followed by voltage a ramp up to 0.9 pu for one second. The reactive power exchanged between the generating unit and the power system is strictly defined in 0 pu for the whole event.

3.5 Harmonization and future trend in grid code requirement

The grid code analysis given in [9], [11] and [26] highlight that the interconnection requirements differ substantially between TSOs. These differences are somewhat acceptable due to the fact that each requirement is strictly related to the particular technical and operational characteristic of each power system. For instance, it is acceptable that LVRT recovery ramp rates of weakly interconnected system such as the Irish or Danish grid are slower than an strongly interconnected system like the Spanish grid, as illustrated in Fig. 3.2. In this regard, exact values for parameters considered for normal or abnormal condition such as range limits, dead-bands, set points, etc., cannot be fully standardized, since they depend on system characteristics e.g.: faster frequency response will be necessary for systems with a low inertia [10].

These natural differences between grid codes impose great challenges on wind turbine manufacturers, which are constantly adapting and developing their current products according to the latest requirements imposed by different TSOs [10]. Although this exercise contributes to bring forward the state of the art of wind turbines technology, a vast diversification of grid code requirements creates, at the same time, a narrow market-based development trend among different countries. For this reason, in the last decade, TSO associations and power generating facility owners including wind turbine manufacturers have joint efforts in order to find standardization in technical and operational requirements [26].

The European grid code ENTSO-E Network Code [25] has been developed with close cooperation of power generating facility manufacturers with their relevant TSO. The code defines a common framework of grid connection requirements for interconnecting generating plants including synchronous power generating modules, solar and onshore wind power plants as well as offshore installations with the European electricity grid. Similarly, the TSOs in Denmark, Finland, Norway and Sweden have joint efforts in developing a Nordic Grid Code [24], in which the LVRT profile

and voltage/frequency dependencies are specified, among other requirements.

The European Wind Energy Association (EWEA) has also urged European TSOs to achieve consistency in their future grid codes in order to harmonized regulations throughout the global market. This action will allow wind turbine manufacturers to move from market-oriented products to universal solutions, in order to adapt their hardware and software design with a globally optimized criteria [11].

Finally, the trend in grid code development for power electronic interfaced generating units will be focused on its contribution of increasing the overall reliability of the power system. As discussed in [11] and [26], future wind farms will be required to provide e.g.: reactive power support during faults (as today it is required, for example, by the German and Danish TSO, but not by the Swedish TSO); to emulate the inertia response of synchronous generators (varying the active power set point by implementing a control strategy capable of suppress frequency deviations present in the grid [26]); and to provide power oscillation damping capabilities.

3.6 Grid code testing of wind turbines

The IEC 61400-21 standard issued by International Electrotechnical Commission (IEC) defines the methodology to test part of the requirement stated in grid codes for interconnection of wind turbines [15]. In addition, as described in [29], different test methods exist today to verify the LVRT ability of renewable energy sources. For example, these type of devices include the use of autotransformer with controllable tap changer, controllable shunt reactances to rapidly vary the voltage at the connection point, synchronous generator with a controllable excitation circuit, or series-connected VSC [30], [31].

Moreover, in order to fulfil the standard criteria, specialized testing equipment has been developed. In the following, an introduction of existing solutions for grid code testing of wind turbines is given. The most common testing device for LVRT test of wind turbine is the impedance-based voltage sag generator [14], [28], [32] , which will be briefly described in the following section.

3.6.1 Impedance-based testing equipment

A widely used testing equipment for LVRT test of wind turbines is shown in Fig. 3.5. The impedances that constitute the testing device are arranged in order to form a voltage divider at the terminals of the tested object, when the circuit-breaker is series with Z_{shunt} is closed during the test. By a proper selection of the impedances Z_{grid} and Z_{shunt}, the amplitude and phase angle of the applied voltage can be controlled as desired.

The simple and robust design of this testing device is a great advantage, specially when handling high short-circuit current from the tested object. Moreover, the testing device is modular and can be placed inside a container. It is easy to transport and can be use to perform on-site test of installed wind turbines. A more detailed description of the impedance-based LVRT testing device including field test results of a 2 MW wind turbine is given in [32].

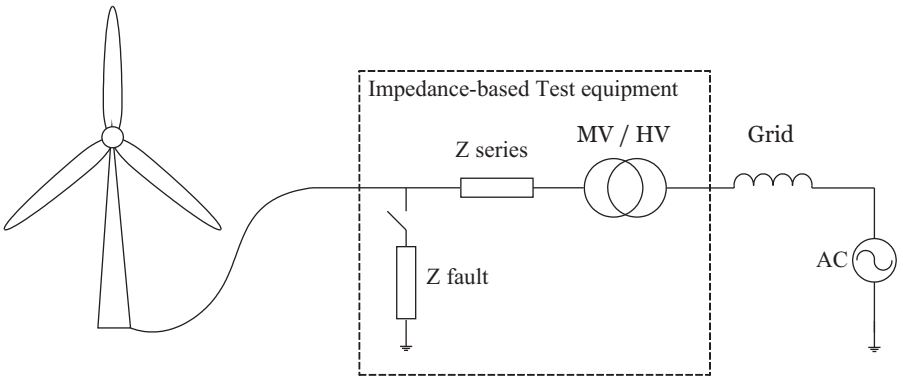

Fig. 3.5 Single line diagram of the standard LVRT test equipment.

One of the main drawbacks of this testing device is the fact that it is only able to apply voltage steps variations due to the closing/opening action of the breaker when connecting the shunt impedance at the terminals of the wind turbine. Therefore, is unable to perform the voltage recovery ramp that exist in the majority of the grid codes. In addition, when performing the test, the device is highly dependent of the short-circuit power at the connection point with the grid, which will also impact the resulting wind turbine voltage [32].

Moreover, the use of circuit breakers introduces uncontrollable delays when emulating the fault and can give rise to high harmonic content into the voltage profile applied to the test object [29], [33]. For this reason, a variant of this device, mainly including the use of power electronic switched shunt impedance, has been proposed in [34]. In the proposed prototype, as a difference of the scheme given in Fig. 3.5, the impedance Z_{shunt} is replaced with a variable tap shunt transformer, in which the retained voltage applied to the test object can be selected by varying its turns ratio. In addition, the circuit-breaker is substituted by a bi-directional power electronic switch.

3.6.2 Other kind of voltage sag generator

Different kind of voltage sag generators have been proposed in addition to the impedance-based test equipment described in the previous section [29], [33]. Some of this testing devices include the use of transformer with selective voltage output, as shown in Fig. 3.6. In this setup, the primary of the transformer is connected to an AC grid while the generating unit is connected to the secondary side. Observe that the secondary winding is divided into two sets of three-phase transformed voltages. During no-fault operation of the test, the generating unit is connected at full-rated voltage by closing the switch S1 while S2 remains open. The voltage dip is performed by reconnecting the generating unit to a different transformed voltage for a short period of time. In order to achieve this, S1 is opened and S2 is closed. The recovery of the voltage is performed by bringing S1 and S2 to its previous state.

The benefits of using this kind of sag generator is that is relatively cheap, it uses standard components such as transformer and contactor, in addition to a relatively simple control system of

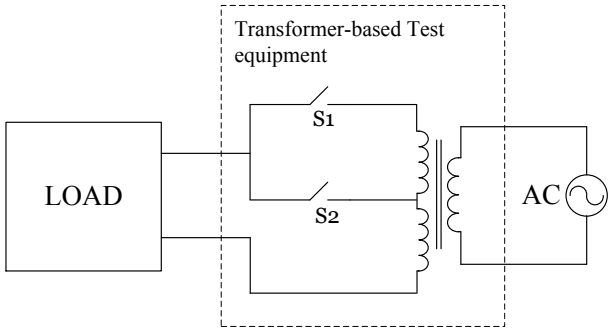

Fig. 3.6 Single-phase diagram of a transformer-based testing device.

the test-bench. For these reasons, this setup is found to be suitable for laboratory experiment [31].

One of the main drawback of this prototype is that the operation time of the contactors cannot be fully controlled and thus voltage and current transient might occur, damaging, for example, the power-electronic converters included in a typical wind turbine system [35]. Similarly to the previous case, a variant of this transformer-based testing device has been proposed in [35], which includes the use of a power electronic switching stage. This solution is transient-friendly due to the inclusion of fully-controlled Insulated Gate Bipolar Transistors (IGBT). However, the use of only two pre-defined voltage levels of the secondary winding limits the output voltage to be controlled with step variations only. In addition, the testing equipment is coupled directly to the grid, therefore, it is fully dependent on the short-circuit ratio at the point of connection. In addition, it is incapable of varying the frequency of the applied voltage. Finally, for wind power applications, the weigh and scale of a multi-MW transformer can be very bulky, difficulting its transportation when on-site LVRT test is needed.

Finally, in [35] and [36] it is discussed the use of generator-based voltage sag generator. In order to generate an output voltage of the machine, a diesel motor is mechanically coupled in the rotor-shaft. The voltage dip is then performed by varying the excitation field in the rotor circuit. In this setup, the applied frequency can be fully controlled. However, its functionality is basically limited to symmetrical voltage dip with a relatively long response time due to the dynamic of the back-EMF in the generator. Moreover, a bulky multi-MW diesel stand-alone generator system can be very expensive and difficult to transport [36]. For these reasons, this kind of voltage sag generator is unsuitable for on-site LVRT test of wind turbines.

3.6.3 VSC-based testing device

Another solution to realize a voltage sag generator is to use fully-rated VSC in back-to-back configuration. By controlling the turbine-side output of the converter system, all kind of grid fault can be emulated [31]. Thanks to the full controllability of the applied voltage in terms of magnitude, phase and frequency, the use of VSC-based testing equipment, shown in Fig. 3.7, provides more flexibility as compared with the standard impedance-based test equipment [9], [32], and also brings more advantages in terms of size and weight [29], [36]. In addition, the AC grid is decoupled from the tested object when performing the test; meaning that the strength of the

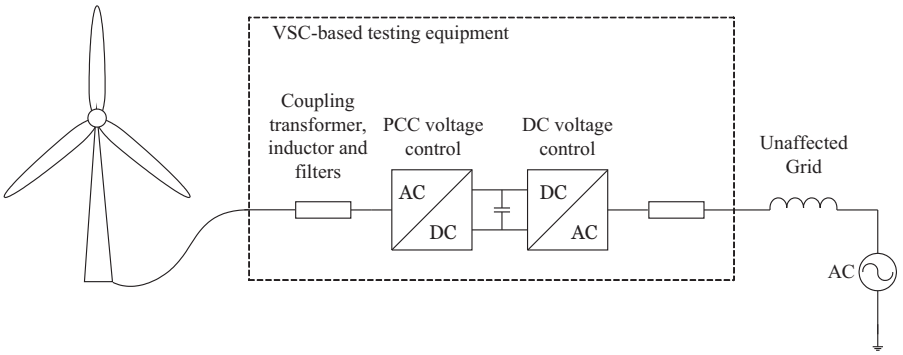

Fig. 3.7 Single line diagram of a VSC-based test equipment.

grid is not a limitation, if a proper control strategy of the gird-side VSC of the test equipment is implemented.

Moreover, the LVRT profile given in grid code can be fully tested including the recovery ramp [9]. Similarly, a phase-angle jump can be easily performed by manually adding a phase shift in the applied voltage. In addition, the fully controllability of the voltage allows for the emulation of any kind of grid scenario applied to the tested object i.e.: it can emulate either an infinite grid [9], or a grid with a predefined short circuit power, as explored later in this thesis. This particular feature is useful when testing, for example, voltage support capabilities of wind turbines.

Its precise control allows for more possibilities of tests that can be carried out. For instance, frequency characterization of wind turbines can be performed by introducing asynchronous frequency content into the applied voltage while observing the equivalence admittance at the PCC. Additionally, frequency support capacity of the tested object can be evaluated by performing a test where the frequency applied at the PCC is varied. In the same way, with a proper emulation of the synchronous generator including its poor mechanical damping, power oscillation damping capability of wind turbine can also be tested.

The main drawback of this technology is the fact that is more expensive than using the standard testing devices introduced in the previous section. In addition, the control algorithm needed to implement such arrangement of VSC is more complex because of the use of software-driven power electronics. Moreover, to emulate grid fault as realistically as possible, a high dynamic performance controller of the output voltage of the VSC is necessary [37].

This concept has been also investigated in previous work. For instance, open-loop control for this test equipment to perform voltage dip test on wind turbine has been investigated in [38] and in [37]. In these examples, the VSC-based testing equipment is treated as an infinite bus and no insight on the stability of the system is given. In a different subjects, close-loop control of VSC-HVDC systems with virtual impedance emulation is given in [39] and also discussed in [40]. However, this approach has never been implemented for testing procedures. For these reasons, a new approach of grid code testing of wind turbines using VSC-based testing equipment is investigated in this Thesis.

3.7 Conclusion

In this chapter, a comparison of grid requirements regarding interconnection of wind turbine was given. The dependencies between system voltage, grid frequency, and active reactive power production during steady-state operation of the grid were introduced. In addition, requirements for LVRT and voltage support during fault were described in detail. Finally, different grid code testing devices have been described including the standard impedance-based, transformer-based, generator-based and finally VSC-based test equipments which will be further investigated in this thesis.

Chapter 4

Modeling of the FPC wind turbine and back-to-back VSC-based testing device

4.1 Introduction

In this chapter, the derivation of the control algorithms that govern both the testing device and the wind turbine will be described. First, the electrical model of the collector and grid VSC of the testing equipment is shown in detail, with special focus in the control scheme of each VSC. The electrical model of the wind turbine system and the control of the wind turbine VSC will also be described, with special focus on the implemented LVRT control strategy.

4.2 Layout of the testing setup

The investigated setup is constituted by a 4 MW FPC wind turbine and 8 MW back-to-back VSC system. The model presented in this work resembles an actual testing setup located in Gothenburg, Sweden [41]. The schematic of the wind turbine connected to the VSC-based testing device is depicted in Fig. 4.1.

The wind turbine is rated in 4 MW, 0.69 kV. The generator is directly connected to the back-to-back VSC. A filtering stage between the generator and the VSC can be used to reduce high-order transient dynamics in the generator current. The VSC, operated in torque or speed control mode, injects the generated power into the DC-link capacitor. The grid-side VSC of the wind turbine controls the DC-link voltage. Finally, the output transformer of the wind turbine steps-up the voltage from 0.69 kV to 10 kV.

The test equipment is rated in 8 MVA, 10 kV. The wind turbine is coupled to the testing device through a coupling transformer. In the secondary of the transformer, a filter bank is placed in order to remove the harmonic content produced by the VSC. The collector-side VSC controls the voltage at the PCC, while the grid-side converter is controlling the DC-link voltage. Finally, the testing equipment is interfaced with the grid by means of filter bank and coupling transformer.

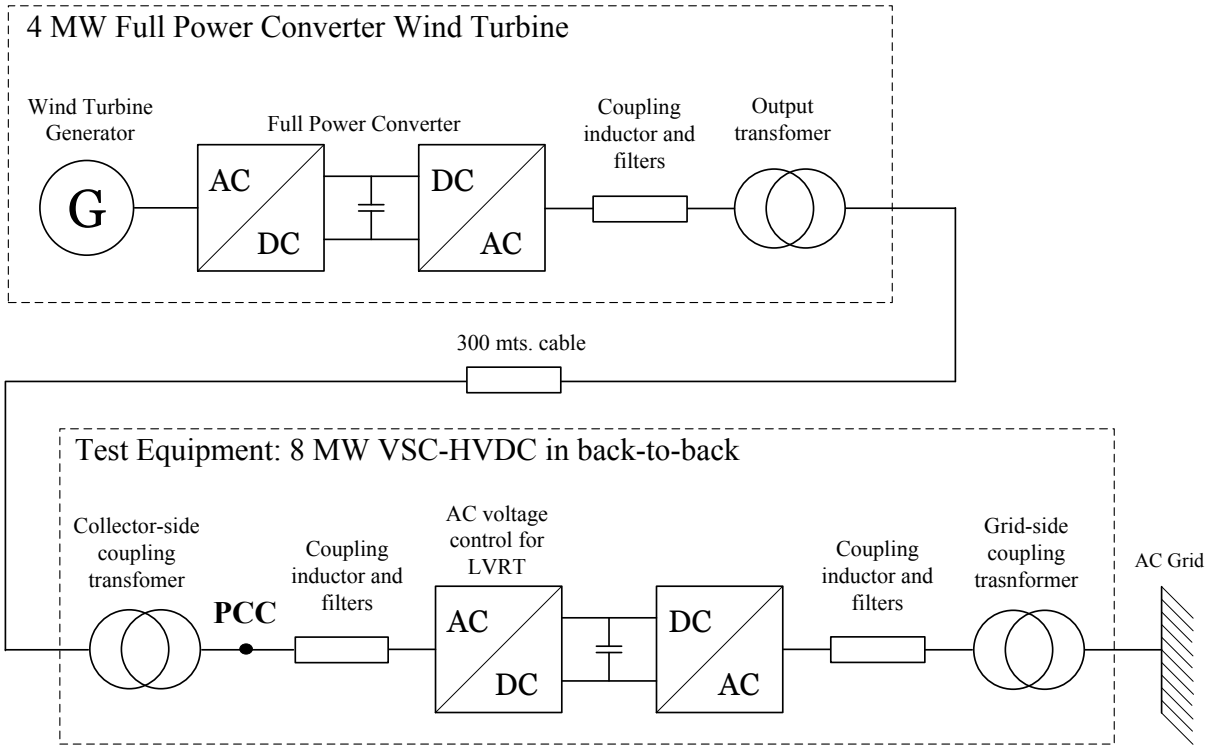

Fig. 4.1 Schematic of the testing setup.

4.3 Modeling of the VSC-based testing equipment

The circuital scheme of the back-to-back VSC-based testing equipment, including power electronic switches, filter bank and coupling transformer is given in Fig. 4.2. The grid-coupling transformer $T2$ of the testing equipment is connected to the AC grid, here represented by a infinite bus denoted with the three-phase voltages $e_{\mathrm{s,a}}(t)$, $e_{\mathrm{s,b}}(t)$ and $e_{\mathrm{s,c}}(t)$. An interface inductor is placed between the terminals of the grid-VSC and the transformer where the current $i_{\mathrm{tg,a}}(t)$, $i_{\mathrm{tg,b}}(t)$ and $i_{\mathrm{tg,c}}(t)$ is measured. The grid interface inductor is here represented by the series inductive filter $L_{\mathrm{f,g}}R_{\mathrm{f,g}}$. Moreover, the voltage $e_{\mathrm{g,a}}(t)$, $e_{\mathrm{g,b}}(t)$ and $e_{\mathrm{g,c}}(t)$ is measured where a filter bank tuned for suppressing the switching harmonics is placed. Finally, the grid VSC is a two-level VSC constituted by 6 IGBTs with their corresponding anti-parallel diode. The three-phase voltage at the terminal of the grid-VSC are denoted as $u_{\mathrm{g,a}}(t)$, $u_{\mathrm{g,b}}(t)$ and $u_{\mathrm{g,c}}(t)$.

The DC-link voltage across the capacitor C_{DC} is denoted as $u_{\mathrm{DC}}(t)$ and the measured DC current is labelled $i_{\mathrm{DC}}(t)$. No DC filters or DC crowbar have been included in the model of the test equipment. The switching signals are calculated by Pulse Width Modulation (PWM) technique [13].

The collector-side VSC and its interface inductor including the filter bank and coupling transformer are also depicted in Fig. 4.2. The labelling of the electrical variables and components of the collector circuit resembles the structure given in the previous paragraph. The collector-VSC is

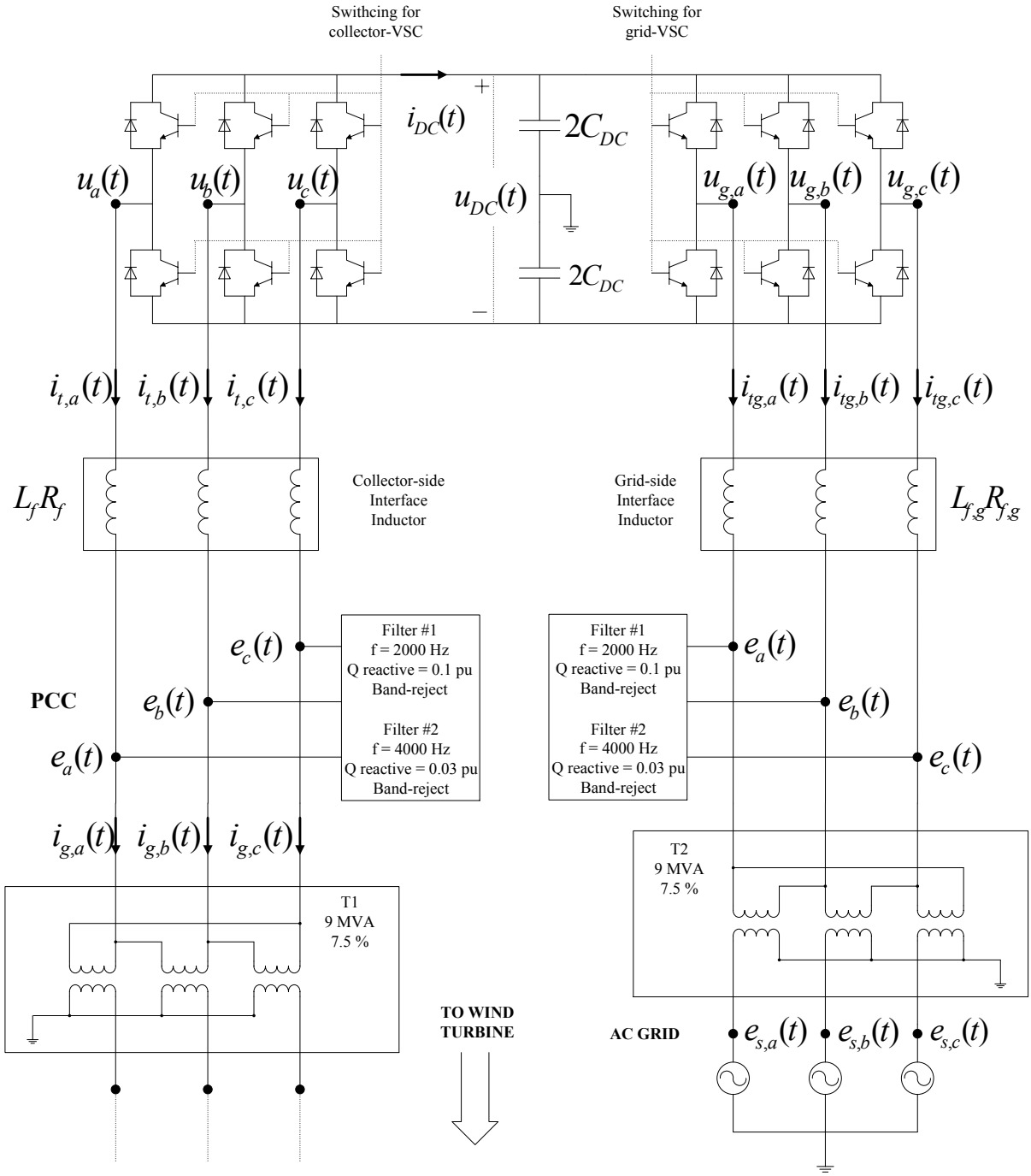

Fig. 4.2 Main circuit of the back-to-back VSC testing equipment.

a two-level IGBT-based VSC, again modulated with PWM. The three-phase terminal voltage of the collector-VSC is denoted as $u_{\mathrm{a}}(t)$, $u_{\mathrm{b}}(t)$ and $u_{\mathrm{c}}(t)$, and the three-phase terminal current are labelled as $i_{\mathrm{t,a}}(t)$, $i_{\mathrm{t,b}}(t)$ and $i_{\mathrm{t,c}}(t)$. The interface inductor is represented by the series inductive filter $L_{\mathrm{f}}R_{\mathrm{f}}$. Similarly, a filter bank tuned for suppressing the switching harmonics has been also

modeled. The three-phase PCC voltage is denoted as $e_{\mathrm{a}}(t)$, $e_{\mathrm{b}}(t)$ and $e_{\mathrm{c}}(t)$.

Finally, the output three-phase current from the PCC into the secondary of the coupling transformer $T1$ is here denoted as $i_{\mathrm{g,a}}(t)$, $i_{\mathrm{g,b}}(t)$ and $i_{\mathrm{g,c}}(t)$. Finally, the test object is connected at the primary of the coupling transformer $T1$, as shown in Fig. 4.1. In the following, the control system of the testing equipment is presented.

4.4 Control of the collector-VSC of the testing equipment

The simplified single-line diagram representation of the circuit given Fig. 4.2 is shown in Fig. 4.3. Here, only the capacitive effect of the collector filter bank and grid filter bank have been represented by the shunt capacitors C_{f} and $C_{\mathrm{f,g}}$, respectively. Moreover, the inductive and resistive components that constitute the interfacing inductor at the collector-side of the test equipment are here represented by the inductance L_{f} in series with its internal resistance R_{f}. Similarly, as shown in Fig. 4.3, the filter inductance and internal resistance of the grid series inductor are here denoted as $L_{\mathrm{f,g}}$ and $R_{\mathrm{f,g}}$, respectively. The parameters of the modelled testing equipment are given in Table 4.1.

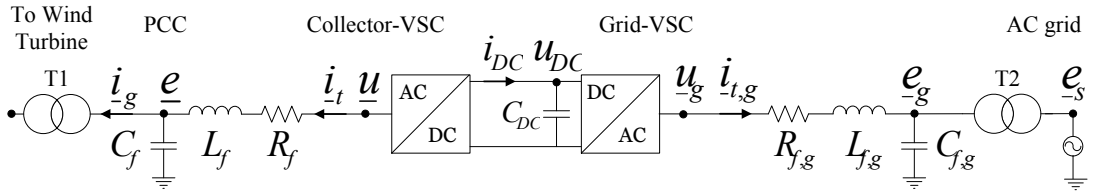

Fig. 4.3 Simplified single-line diagram of the testing equipment.

With focus on the collector-side VSC of the testing equipment, the main control blocks that constitute the implemented discrete controller are shown in Fig. 4.4. The control has been developed in the synchronously rotating dq frame [42]. In Appendix A is found the adopted

TABLE 4.1. TESTING EQUIPMENT PARAMETERS.

Base values		8 MVA, 10 kV, 50 Hz
Grid-VSC filter inductance	$L_{\mathrm{f,g}}$	0.15 pu
Grid-VSC filter internal resistance	$R_{\mathrm{f,g}}$	0.015 pu
Grid-VSC filter capacitance	$C_{\mathrm{f,g}}$	7.5 pu
Transformer T2 impedance	$X_{\mathrm{tr,2}}$	0.08 pu
Collector-VSC filter inductance	L_{f}	0.15 pu
Collector-VSC filter internal resistance	R_{f}	0.015 pu
Collector-VSC filter capacitance	C_{f}	7.5 pu
Transformer T1 impedance	$X_{\mathrm{tr,1}}$	0.08 pu
DC-link capacitor size	C_{DC}	2 pu
VSC switching frequency	f_{sw}	2000 Hz
Sampling period	t_{s}	0.25 ms

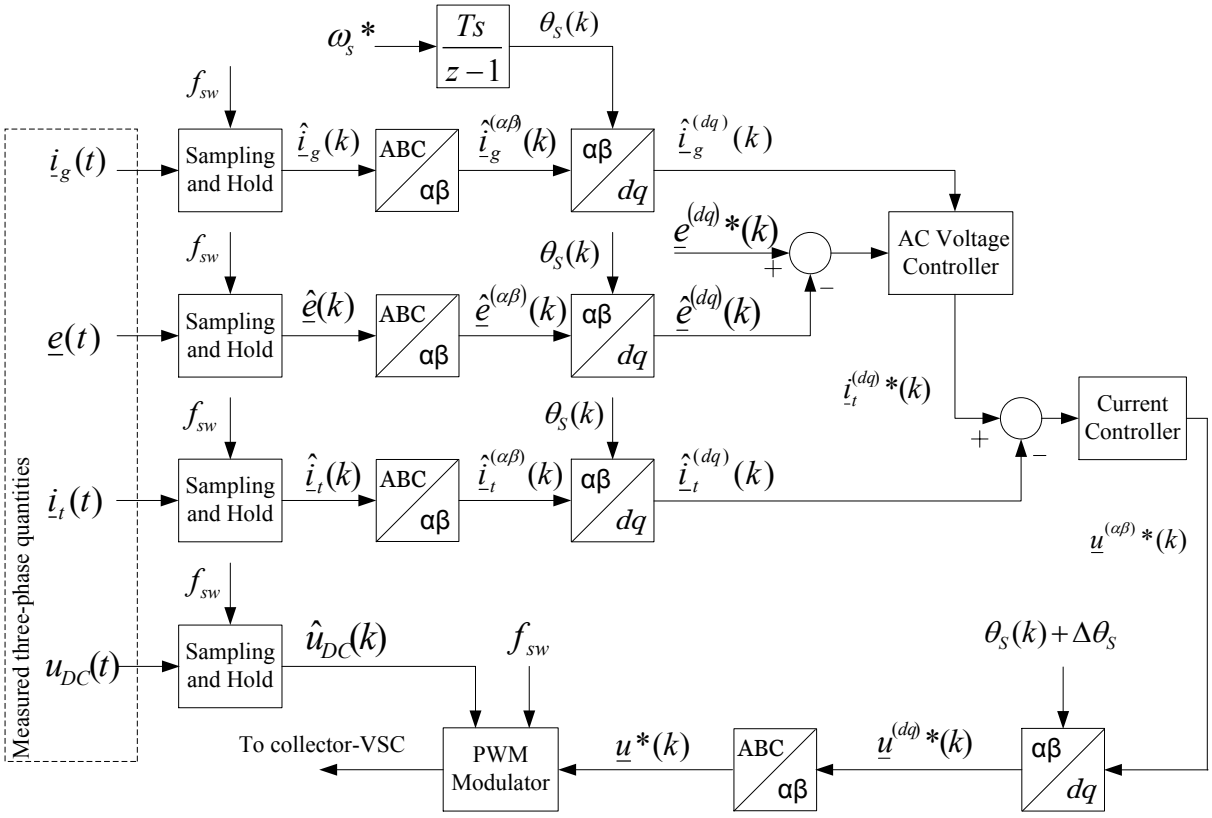

Fig. 4.4 Block diagram of the cascaded vector controller for the collector-VSC of the testing equipment.

amplitude-invariant Clark's Transformation from three-phase to $\alpha\beta$ stationary reference frame, and Park's Transformation from $\alpha\beta$ to dq rotating reference frame, and vice versa.

In the control algorithm of the collector-VSC of the test equipment, a dedicated PCC voltage control is implemented. The role of this controller is to generate the reference current for the inner-current controller of the converter. The structure of the cascaded current controller is shown in Fig. 4.4. The output of the controller is the reference value for the output voltage of the VSC. The calculated voltage is then transformed from dq-reference frame into three-phase quantities. Finally, a PWM modulator is used to compute the switching signals of the converter. In the following, the implemented cascaded control strategy will be described in detail.

4.4.1 Inner current controller

Considering the circuit given in Fig. 4.3, the dynamics of the current $\underline{i}_\mathrm{t}$ that flows between the terminals collector-VSC and the PCC can be described in the dq-frame as:

$$\frac{d\underline{i}_\mathrm{t}^{(dq)}}{dt}L_\mathrm{f} + j\omega_\mathrm{s}L_\mathrm{f}\underline{i}_\mathrm{t}^{(dq)} + R_\mathrm{f}\underline{i}_\mathrm{t}^{(dq)} = \underline{e}^{(dq)} - \underline{u}^{(dq)} \tag{4.1}$$

In order to derive the current control, (4.1) needs to be transformed into Laplace form [12]. Moreover, by rearranging the transformed equation, the open-loop transfer function $G_{\mathrm{I}}(s)$ is obtained:

$$\frac{\underline{i}_{\mathrm{t}}^{(dq)}(s)}{\underline{e}^{(dq)}(s) - \underline{u}^{(dq)}(s)} = \frac{1}{R_{\mathrm{f}} + j\omega_{\mathrm{s}}L_{\mathrm{f}} + sL_{\mathrm{f}}} = G_{\mathrm{I}}(s) \tag{4.2}$$

Derivation of the current controller

The controller has been derived using the Internal Model Control (IMC) method given in [43] and [44]. By assuming perfect knowledge of the parameters, the effect of the voltage drop across the coupling term $j\omega_{\mathrm{s}}L_{\mathrm{f}}$ is cancelled in steady-state via feed-forward when deriving the current control loop [44]. The open-loop transfer function $G_{\mathrm{I_{OL}}}(s)$ is constituted by the controller $F_{\mathrm{C_I}}(s)$ in cascade with the decoupled plant $G'_{\mathrm{I}}(s)$ as

$$G_{\mathrm{I_{OL}}}(s) = F_{\mathrm{C_I}}(s)G'_{\mathrm{I}}(s) \tag{4.3}$$

where $G'_{\mathrm{I}}(s)$ in (4.3) is the reduced transfer function of the filter impedance in Laplace form given in (4.2) without the cross-coupling term, expressed in full form as

$$G'_{\mathrm{I}}(s) = \frac{1}{R_{\mathrm{f}} + sL_{\mathrm{f}}} \tag{4.4}$$

In Fig. 4.5 it is found a graphical representation of the devised transfer function. The transfer function of the PI controller $F_{\mathrm{C_I}}(s)$ for the current control is:

$$F_{\mathrm{C_I}}(s) = k_{\mathrm{p_I}} + \frac{k_{\mathrm{i_I}}}{s} \tag{4.5}$$

The closed-loop transfer function $G_{\mathrm{I_{CL}}}(s)$ from $\underline{i}_{\mathrm{t}}^{(\mathrm{dq})^*}$ to $\underline{i}_{\mathrm{t}}^{(\mathrm{dq})}$ can be expressed as

$$G_{\mathrm{I_{CL}}}(s) = \frac{\underline{i}_{\mathrm{t}}^{(\mathrm{dq})}}{\underline{i}_{\mathrm{t}}^{(\mathrm{dq})^*}} = \frac{G_{\mathrm{I_{OL}}}(s)}{1 + G_{\mathrm{I_{OL}}}(s)} \tag{4.6}$$

by substituting (4.4) and (4.5) in (4.6), and shaping the close-loop trasnfer function as a first order low-pass filter i.e.:

$$G_{\mathrm{I_{CL}}}(s) = \frac{F_{\mathrm{C_I}}(s)G'_{\mathrm{I}}(s)}{1 + F_{\mathrm{C_I}}(s)G'_{\mathrm{I}}(s)} = \frac{\alpha_{\mathrm{cc}}/s}{1 + \alpha_{\mathrm{cc}}/s} \tag{4.7}$$

where α_{cc} is the selected bandwidth of the close-loop system $G_{\mathrm{I_{CL}}}(s)$, the control parameters $k_{\mathrm{p_I}}$ and $k_{\mathrm{i_I}}$ can be determined. In Fig. 4.5 it is shown a block diagram representation of the cascaded transfer functions. By arranging (4.7) into the form

$$F_{\mathrm{C_I}}(s) = \frac{\alpha_{\mathrm{cc}}}{s} G'_{\mathrm{I}}(s)^{-1} \tag{4.8}$$

and further developing (4.8), the PI control parameters $k_{\mathrm{p_I}} = \hat{L}_{\mathrm{f}}\alpha_{\mathrm{cc}}$ and $k_{\mathrm{i_I}} = \hat{R}_{\mathrm{f}}\alpha_{\mathrm{cc}}$ are found. Observe that the parameters $\hat{L}_{\mathrm{f}}$ and $\hat{R}_{\mathrm{f}}$ are the estimated filter inductance and resistance, respectively. Moreover, when deriving the final control law, the feedforward of the cross-coupling term $j\omega_{\mathrm{s}}\hat{L}_{\mathrm{f}}$ allows to independently control the direct and quadrature axis component of the estimated terminal current, $\hat{i}_{\mathrm{t_d}}$ and $\hat{i}_{\mathrm{t_q}}$, respectively. Finally, (4.9) shows the implemented controller in Laplace form:

$$\underline{u}^{(\mathrm{dq})^*} = \underline{\hat{e}}^{(\mathrm{dq})} + j\omega_{\mathrm{s}}\hat{L}_{\mathrm{f}}\underline{\hat{i}}_{\mathrm{t}}^{(\mathrm{dq})} + (k_{\mathrm{p_I}} + \frac{k_{\mathrm{i_I}}}{s})(\underline{i}_{\mathrm{t}}^{(\mathrm{dq})^*} - \underline{\hat{i}}_{\mathrm{t}}^{(\mathrm{dq})}) \tag{4.9}$$

where $\underline{\hat{e}}^{(\mathrm{dq})}$ is the estimated grid voltage. The computed voltage $\underline{u}^{(\mathrm{dq})^*}$ is the reference output voltage of the collector-side VSC. As given in Table 4.1, the sampling frequency of the VSC is 4 kHz and its bandwidth is 25132 [rad/s]. As suggested in [43], the sampling of the electrical quantities should be much faster than the inner control loop, i.e.: a separation of at least one decade. Thus, the bandwidth of the current control α_{cc} is selected to be 2500 [rad/s]. The discrete implementation of the current controller is further discussed in Section 4.4.1

Implementation of the anti-windup in the current controller

So far, the current controller has been derived assuming that the VSC has a limitless voltage rating in its output; thus, the controller is able to generate any desired voltage, i.e.: $\underline{u}^{(\mathrm{dq})} = \underline{u}^{(\mathrm{dq})^*}$. Although this approach is useful when calculating for instance the PI parameters, the voltage at the VSC terminals is limited within its rating. When using an integrator term in the control loop, a windup of the integrator output might occur in case of controller saturation, i.e.: $\underline{u}^{(\mathrm{dq})^*} > \underline{u}_{\mathrm{max}}^{(\mathrm{dq})}$.

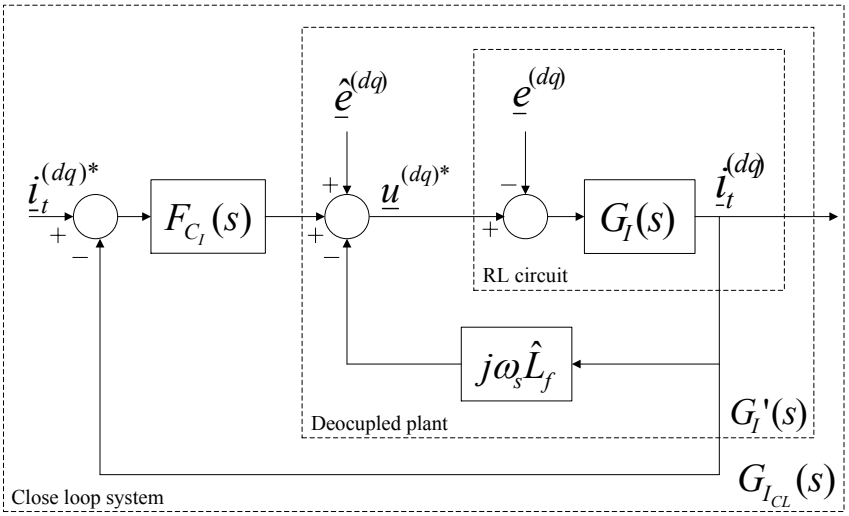

Fig. 4.5 Block diagram of the current controller and RL filter transfer functions in close-loop.

In this case, the error input of the integrator must be limited. By defining the current control error $\underline{\epsilon_{\mathrm{I}}}^{(\mathrm{dq})}$ as

$$\underline{\epsilon}_{\mathrm{I}}^{(\mathrm{dq})} = (\underline{i}_{\mathrm{t}}^{(\mathrm{dq})^*} - \hat{\underline{i}}_{\mathrm{t}}^{(\mathrm{dq})}) \tag{4.10}$$

and substituting (4.10) in (4.9), assuming a non saturation of the controller, the unlimited reference voltage is obtained:

$$\underline{u}^{(\mathrm{dq})^*} = \hat{\underline{e}}^{(\mathrm{dq})} + j\omega_{\mathrm{s}}\hat{L}_{\mathrm{f}}\hat{\underline{i}}_{\mathrm{t}}^{(\mathrm{dq})} + k_{\mathrm{p_I}}\underline{\epsilon}_{\mathrm{I}}^{(\mathrm{dq})} + \frac{k_{\mathrm{i_I}}}{s}\underline{\epsilon}_{\mathrm{I}}^{(\mathrm{dq})} \tag{4.11}$$

When the controller requests a voltage that is greater than the converter rating, the saturated output voltage reference becomes

$$\underline{u}_{\mathrm{sat}}^{(\mathrm{dq})^*} = \hat{\underline{e}}^{(\mathrm{dq})} + j\omega_{\mathrm{s}}\hat{L}_{\mathrm{f}}\hat{\underline{i}}_{\mathrm{t}}^{(\mathrm{dq})} + k_{\mathrm{p_I}}\underline{\epsilon}_{\mathrm{I_{sat}}}^{(\mathrm{dq})} + \frac{k_{\mathrm{i_I}}}{s}\underline{\epsilon}_{\mathrm{I_{sat}}}^{(\mathrm{dq})} \tag{4.12}$$

where $\underline{\epsilon}_{\mathrm{I_{sat}}}^{(\mathrm{dq})}$ is the extra error signal added into the integrator when the controller is saturated. Subtracting (4.11) from (4.12), the term $\underline{\epsilon}_{\mathrm{I_{sat}}}^{(\mathrm{dq})}$ is found:

$$\underline{\epsilon}_{\mathrm{I_{sat}}}^{(\mathrm{dq})} = \underline{\epsilon}_{\mathrm{I}}^{(\mathrm{dq})} + \frac{\underline{u}_{\mathrm{sat}}^{(\mathrm{dq})^*} - \underline{u}^{(\mathrm{dq})^*}}{k_{\mathrm{p_I}}} \tag{4.13}$$

Observe in (4.13) that when the controller is not saturated, $\underline{\epsilon}_{\mathrm{I_{sat}}}^{(\mathrm{dq})} = \underline{\epsilon}_{\mathrm{I}}^{(\mathrm{dq})}$ and the VSC is operated within its limits.

Discrete implementation

In the previous section the current controller has been derived in the frequency domain. However, in applications such as discrete-time simulation and implementation of a digital control in a laboratory environment, the control law given in (4.13) needs to be discretized. In order to derive the current controller in discrete form, the following assumptions are made:

- The capacitor voltage $\hat{\underline{e}}^{(\mathrm{dq})}$ changes slowly and can be considered to be constant over the sampling period t_{s}, thus:

$$\frac{\hat{\underline{e}}^{(\mathrm{dq})}(k+1) + \hat{\underline{e}}^{(\mathrm{dq})}(k)}{2} = \hat{\underline{e}}^{(\mathrm{dq})}(k) \tag{4.14}$$

- The variation of the current $\hat{\underline{i}}_{\mathrm{t}}^{(\mathrm{dq})}$ across the filter inductor L_{f} is linear:

$$avg(\hat{\underline{i}}_{\mathrm{t}}^{(\mathrm{dq})}(k, k+1)) = \frac{\hat{\underline{i}}_{\mathrm{t}}^{(\mathrm{dq})}(k+1) + \hat{\underline{i}}_{\mathrm{t}}^{(\mathrm{dq})}(k)}{2} \tag{4.15}$$

- The voltage $\underline{u}^{(\mathrm{dq})}$ delivered by the VSC is, in average, equal to the reference value $\underline{u}^{(\mathrm{dq})^*}$ during the period t_s

$$avg(\underline{u}^{(\mathrm{dq})}(k, k+1)) = \underline{u}^{(\mathrm{dq})^*}(k) \tag{4.16}$$

Under these assumption, equation (4.11) can be expressed in discrete form as:

$$\underline{u}^{(\mathrm{dq})^*}(k) = \underline{\hat{e}}^{(\mathrm{dq})}(k) + j\omega_\mathrm{s}\hat{L}_\mathrm{f}\underline{\hat{i}}_\mathrm{t}^{(\mathrm{dq})}(k) + k_\mathrm{pI}\underline{\epsilon}_\mathrm{I}^{(\mathrm{dq})}(k) + \underline{I}_\mathrm{I}(k) \tag{4.17}$$

with

$$\underline{\epsilon}_\mathrm{I}^{(\mathrm{dq})}(k) = \underline{i}_\mathrm{t}^{(\mathrm{dq})^*}(k) - \underline{\hat{i}}_\mathrm{t}^{(\mathrm{dq})}(k) \tag{4.18}$$

as the current error in discrete form at the instant k. Moreover, $\underline{\hat{e}}^{(\mathrm{dq})}(k)$ and $\underline{\hat{i}}_\mathrm{t}^{(\mathrm{dq})}(k)$ are the grid voltage and filter current, respectively, at the sampling instant k . The term $\underline{u}^{(\mathrm{dq})^*}(k)$ is the reference converter voltage at instant k, and $\underline{I}_\mathrm{I}(k)$ is the integrator state during the instant k. With forward-Euler method, the integrator function in discrete form is calculated as:

$$\underline{I}_\mathrm{I}(k+1) = \underline{I}_\mathrm{I}(k) + k_{\mathrm{i_I}}T_\mathrm{s}\left(\underline{\epsilon}_\mathrm{I}^{(\mathrm{dq})}(k) + \frac{\underline{u}_\mathrm{sat}^{(\mathrm{dq})^*}(k) - \underline{u}^{(\mathrm{dq})^*}(k)}{k_\mathrm{pI}}\right) \tag{4.19}$$

Equations (4.17), (4.18) and (4.19) summarize the implemented discrete current controller for the collector-side VSC of the back-to-back VSC-based testing equipment. In Fig. 4.6 it is shown a step response of the current controller. Here, the simulation platform PSCAD/EMTDC v4.2 [45] has been used.

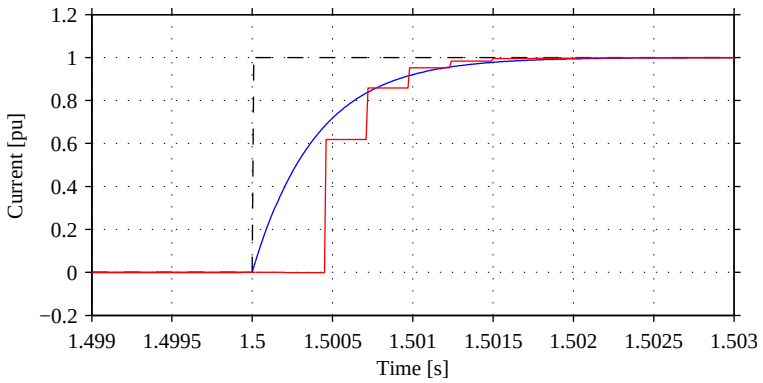

Fig. 4.6 Normalized step response of the current controller: current reference (black dashed), response of system $G_{\mathrm{I_{CL}}}(s)$ (blue) and sampled current $\hat{i}_{\mathrm{t_d}}$ (red).

Observe the similarities between the response of the transfer function $G_{\mathrm{I_{CL}}}(s)$ and the sampled current $\hat{i}_{\mathrm{t_d}}$. With a bandwidth of 2500 [rad/s], a rise time 0.9 ms is expected, as shown in the figure.

4.4.2 PCC voltage controller

The PCC voltage control is in the outer loop of the collector-side VSC control shown in Fig. 4.4. The input of the controller is the reference PCC voltage denoted as $\underline{e}^{(\mathrm{dq})^*}$ and it calculates the necessary current reference $\underline{i}_{\mathrm{t}}^{(\mathrm{dq})^*}$, which are sent into the current controller.

With reference to Fig. 4.3, the current that flows in the capacitor C_{f} can be derived by applying Kirchhoff's law at the PCC

$$\underline{i}_{\mathrm{C_f}}^{(\mathrm{dq})} = \underline{i}_{\mathrm{t}}^{(\mathrm{dq})} - \underline{i}_{\mathrm{g}}^{(\mathrm{dq})} \tag{4.20}$$

Similarly, the dynamic of the current $\underline{i}_{\mathrm{C_f}}^{(\mathrm{dq})}$ is expressed in (4.21)

$$C_{\mathrm{f}} \frac{d\underline{\mathrm{e}}^{(dq)}}{dt} + j\omega_{\mathrm{s}} C_{\mathrm{f}} \underline{e}^{(dq)} = \underline{i}_{\mathrm{C_f}}^{(\mathrm{dq})} \tag{4.21}$$

By simply combining (4.20) and (4.21), the dependency of the PCC voltage $\underline{\mathrm{e}}^{(dq)}$ with the converter terminal current $\underline{i}_{\mathrm{t}}^{(\mathrm{dq})}$ and the grid current $\underline{i}_{\mathrm{g}}^{(\mathrm{dq})}$ can be obtained:

$$C_{\mathrm{f}} \frac{d\underline{\mathrm{e}}^{(dq)}}{dt} + j\omega_{\mathrm{s}} C_{\mathrm{f}} \underline{e}^{(dq)} = \underline{i}_{\mathrm{t}}^{(\mathrm{dq})} - \underline{i}_{\mathrm{g}}^{(\mathrm{dq})} \tag{4.22}$$

The transfer function needed to devise the voltage controller is obtained by transforming (4.22) into Laplace form:

$$\frac{\underline{\mathrm{e}}^{(dq)}(s)}{\underline{i}_{\mathrm{t}}^{(\mathrm{dq})}(s) - \underline{i}_{\mathrm{g}}^{(\mathrm{dq})}(s)} = \frac{1}{sC_{\mathrm{f}} + j\omega_{\mathrm{s}} C_{\mathrm{f}}} = G_{\mathrm{E}}(s) \tag{4.23}$$

where $G_{\mathrm{E}}(s)$ is the open-loop transfer function of the impedance across the capacitor C_{f}. By applying the same methodology (ICM) given in Section 4.4.1. The voltage controller can be derived.

Proportional controller

The close-loop transfer function for the voltage control loop can be expressed as

$$G_{\mathrm{E_{OL}}}(s) = F_{\mathrm{C_E}}(s) G'_{\mathrm{E}}(s) \tag{4.24}$$

where $F_{\mathrm{C_E}}(s)$ is the transfer function of the controller and $G'_{\mathrm{E}}(s)$ is the transfer function of the modified plant which does not include the cross-coupling term $j\omega_{\mathrm{s}} C_{\mathrm{f}}$ in (4.23). By shaping the close-loop transfer function of the voltage controller into a first-order low-pass filter, i.e.:

$$G_{\mathrm{E_{CL}}}(s) = \frac{F_{\mathrm{C_E}}(s) G'_{\mathrm{E}}(s)}{1 + F_{\mathrm{C_E}}(s) G'_{\mathrm{E}}(s)} = \frac{\alpha_{\mathrm{e}}/s}{1 + \alpha_{\mathrm{e}}/s} \tag{4.25}$$

and further rearranging (4.25) into the form

$$F_{\mathrm{C_E}} = \frac{\alpha_{\mathrm{e}}}{s} G'_{\mathrm{E}}(s)^{-1} \tag{4.26}$$

and evaluating $F_{\mathrm{C_E}} = k_{\mathrm{p_E}}$ as a proportional controller with bandwidth $\alpha_{\mathrm{e}} \leq 0.1\alpha_{\mathrm{cc}}$ [43], the gain of the proportional controller is found to be $k_{\mathrm{p_E}} = \alpha_{\mathrm{e}}\hat{C}_{\mathrm{f}}$ with α_{e} is selected to be 250 [rad/s], where $\hat{C}_{\mathrm{f}}$ is the estimated filter capacitance given in Table 4.1. Finally, the control law can be written as

$$\underline{i}_{\mathrm{t}}^{(\mathrm{dq})^*} = k_{\mathrm{p_U}}\underline{\epsilon}_{\mathrm{E}}^{(\mathrm{dq})} + j\omega_{\mathrm{s}}\hat{C}_{\mathrm{f}}\underline{\hat{e}}^{(\mathrm{dq})} + \underline{\hat{i}}_{\mathrm{g}}^{(\mathrm{dq})}\left(\frac{\alpha_{\mathrm{fil}}}{s+\alpha_{\mathrm{fil}}}\right) \tag{4.27}$$

with the voltage error signal defined as

$$\underline{\epsilon}_{\mathrm{e}}^{(\mathrm{dq})} = \underline{e}^{(\mathrm{dq})^*} - \underline{\hat{e}}^{(\mathrm{dq})} \tag{4.28}$$

In order to reject high frequency disturbances, a low pass filter (LPF) with bandwidth α_{fil} = 2500 [rad/s] has been added when feed-forwarding the measured current $\underline{\hat{i}}_{\mathrm{g}}^{(\mathrm{dq})}$ in (4.27). For a digital implementation, the voltage controller given in (4.27) needs to be written in discrete form. With similar approach given in Section 4.4.1, (4.29) shows the discretized voltage controller based on proportional controller and LPF filter:

$$\underline{i}_{\mathrm{t}}^{(\mathrm{dq})^*}(k) = k_{\mathrm{p_E}}\underline{\epsilon}_{\mathrm{E}}^{(\mathrm{dq})}(k) + j\omega_{\mathrm{s}}C_{\mathrm{f}}\underline{\hat{e}}^{(\mathrm{dq})}(k) + \underline{\hat{i}}_{\mathrm{g,fil}}^{(\mathrm{dq})}(k) \tag{4.29}$$

where the discrete voltage error signal is

$$\underline{\epsilon}_{\mathrm{E}}^{(\mathrm{dq})}(k) = \underline{e}^{(\mathrm{dq})^*}(k) - \underline{\hat{e}}^{(\mathrm{dq})}(k) \tag{4.30}$$

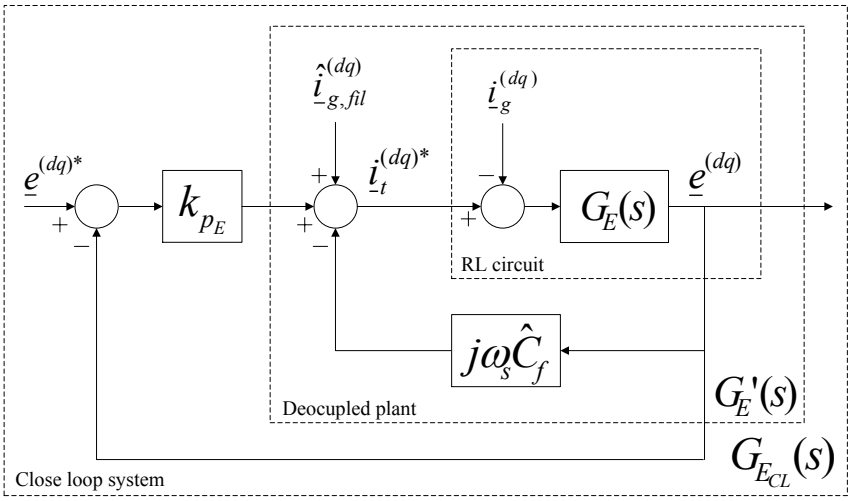

Fig. 4.7 Block diagram of the PCC voltage control based on proportional controller with LPF.

and the filtered grid current $\hat{\underline{i}}^{(\mathrm{dq})}_{\mathrm{g,fil}}(k)$ is calculated as

$$\hat{\underline{i}}^{(\mathrm{dq})}_{\mathrm{g,fil}}(k+1) = (1 - T_\mathrm{s}\,\alpha_\mathrm{fil})\,\hat{\underline{i}}^{(\mathrm{dq})}_{\mathrm{g,fil}}(k) + T_\mathrm{s}\,\alpha_\mathrm{fil}\,\hat{\underline{i}}^{(\mathrm{dq})}_{\mathrm{g}}(k) \tag{4.31}$$

Finally, in Fig. 4.7 it is shown a graphical representation of the implemented PCC.

Proportional and integral controller with active damping

The capacitor C_f in Fig. 4.3 represents the capacitive properties of a filter bank connected to the VSC. A non-accurate knowledge of the filter parameters i.e.: actual capacitance, filter losses, etc, can lead to a steady state error between the reference voltage $\underline{e}^{(\mathrm{dq})^*}$ and the measured voltage $\hat{\underline{e}}^{(\mathrm{dq})}$ at the PCC. For this reason, an integral term can be included in the control law described in (4.27). In order to derive a suitable gain $k_{\mathrm{i_E}}$ for the integrator and at the same time increase the robustness of the control system against voltage disturbances, an active damping term, as suggested in [42] and [44] has been introduced. The principle of active damping is to include a virtual resistor G_A in (4.22); while an integral part is included in the control algorithm to preserve the bandwidth of the close-loop transfer function. The modified equation becomes:

$$C_\mathrm{f}\frac{d\underline{e}^{(dq)}}{dt} + j\omega_\mathrm{s}C_\mathrm{f}\underline{e}^{(dq)} + G_\mathrm{A}\underline{e}^{(dq)} = \underline{i}^{(\mathrm{dq})}_\mathrm{t} - \underline{i}^{(\mathrm{dq})}_\mathrm{g} \tag{4.32}$$

By transforming (4.32) into Laplace form, the open-loop transfer function of the capacitor voltage including the active damping term G_A can be formulated as

$$G_{\mathrm{E,A}}(s) = \frac{1}{sC_\mathrm{f} + j\omega_\mathrm{s}C_\mathrm{f} + G_\mathrm{A}/\widehat{C}_\mathrm{f}} \tag{4.33}$$

when introducing the decoupling term $j\omega_\mathrm{s}\widehat{C}_\mathrm{f}$ in the control law, as shown in Fig. 4.8, a decoupled plant $G'_{\mathrm{E,A}}(s)$ can be devised. As suggested in [44], it is desired that the plant $G'_{\mathrm{E,A}}(s)$ has the same bandwidth as the voltage regulator, previously selected as α_e equal to 250 [rad/s], i.e.:

$$G'_{\mathrm{E,A}}(s) = \frac{1}{sC_\mathrm{f} + G_\mathrm{A}/C_\mathrm{f}} = K_{G'_{\mathrm{E,A}}}\frac{\alpha_\mathrm{e}}{s+\alpha_\mathrm{e}} \tag{4.34}$$

yielding to

$$G_\mathrm{A} = \alpha_\mathrm{e}\widehat{C}_\mathrm{f} \tag{4.35}$$

Similarly, with the approach given in Section 4.4.2, i.e.: devising the close-loop transfer function of the voltage controller and shaping it into a first-order low pass filter, the following equivalence can be established:

$$G_{\mathrm{E,A}_{\mathrm{CL}}}(s) = \frac{F_{\mathrm{C_{E,A}}}(s)G'_{\mathrm{E,A}}(s)}{1 + F_{\mathrm{C_{E,A}}}(s)G'_{\mathrm{E,A}}(s)} = \frac{\alpha_\mathrm{e}/s}{1+\alpha_\mathrm{e}/s} \tag{4.36}$$

which can be rearranged as

$$F_{\mathrm{C_{E,A}}} = \frac{\alpha_{\mathrm{e}}}{s} G'_{\mathrm{E,A}}(s)^{-1} \tag{4.37}$$

By evaluating (4.37) with $F_{\mathrm{C_{E,A}}} = k_{\mathrm{p_E}} + k_{\mathrm{i_E}}/s$, the parameter of the PI controller are found to be $k_{\mathrm{p_E}} = \alpha_{\mathrm{e}}\hat{C}_{\mathrm{f}}$ and $k_{\mathrm{i_E}} = \alpha_{\mathrm{e}}^2\hat{C}_{\mathrm{f}}$.

Finally, the control law of the voltage controller in Laplace form including integrator and active damping is written as follow:

$$\underline{i}_{\mathrm{t}}^{(\mathrm{dq})^*} = (k_{\mathrm{p_E}} + \frac{k_{\mathrm{i_E}}}{s})\underline{\epsilon}_{\mathrm{E}}^{(\mathrm{dq})} + (j\omega_{\mathrm{s}}\widehat{C}_{\mathrm{f}} - G_{\mathrm{A}})\underline{\hat{e}}^{(\mathrm{dq})} + \underline{\hat{i}}_{\mathrm{g}}^{(\mathrm{dq})}\left(\frac{\alpha_{\mathrm{fil}}}{s+\alpha_{\mathrm{fil}}}\right) \tag{4.38}$$

where the voltage error $\underline{\epsilon}_{\mathrm{E}}^{(\mathrm{dq})}$ is defined in (4.28).

Similarly, in order to be implemented the devised control law in a digital controller, (4.38) must be written in discrete form. Equation (4.39) shows the PI-based discrete voltage controller, including active damping and filtering of grid current.

$$\underline{i}_{\mathrm{t}}^{(\mathrm{dq})^*}(k) = k_{\mathrm{p_E}}\underline{\epsilon}_{\mathrm{E}}^{(\mathrm{dq})}(k) + \underline{I}_{\mathrm{E}}(k) + (j\omega_{\mathrm{s}}\widehat{C}_{\mathrm{f}} - G_{\mathrm{A}})\underline{\hat{e}}^{(\mathrm{dq})}(k) + \underline{\hat{i}}_{\mathrm{g,fil}}^{(\mathrm{dq})}(k) \tag{4.39}$$

Observe that in (4.39), the discrete voltage error $\underline{\epsilon}_{\mathrm{E}}^{(\mathrm{dq})}(k)$ is defined in (4.30), and the filtered grid current $\underline{\hat{i}}_{\mathrm{g,fil}}^{(\mathrm{dq})}(k)$ is defined in (4.31). The integral term $\underline{I}_{\mathrm{E}}(k)$, including the needed anti-windup function, is given by:

$$\underline{I}_{\mathrm{E}}(k+1) = \underline{I}_{\mathrm{E}}(k) + k_{\mathrm{i_E}}T_{\mathrm{s}}\left(\underline{\epsilon}_{\mathrm{E}}^{(\mathrm{dq})}(k) + \frac{\underline{i}_{\mathrm{t,sat}}^{(\mathrm{dq})^*}(k) - \underline{i}_{\mathrm{t}}^{(\mathrm{dq})^*}(k)}{k_{\mathrm{p_E}}}\right) \tag{4.40}$$

where $\underline{i}_{\mathrm{t,sat}}^{(\mathrm{dq})^*)}$ is the reference current limited within the ratings of the converter. Finally, in Fig. 4.8 is shown a graphical representation of the implemented PCC voltage controller, based on PI controller and active damping and LPF.

Open loop control

Another option in controlling the imposed voltage at the terminals of the wind turbine is to directly select the output voltage of the testing equipment. That is, by manually varying the voltage $\underline{u}^{(\mathrm{dq})^*}(k)$ according to the LVRT profiles given in the grid codes. In order to avoid step variation of the modulation index, a predefined ramp-rate limiter can be used when calculating the reference voltage of the converter.

$$\underline{u}^{(\mathrm{dq})^*} = \underline{e}_{\mathrm{LVRT}}^{(\mathrm{dq})^*} \tag{4.41}$$

Optionally, by taking into consideration the voltage equation given in (4.1). The steady-state voltage drop over L_{f} and R_{f} can be easily compensated. This allows for an accurate open-loop

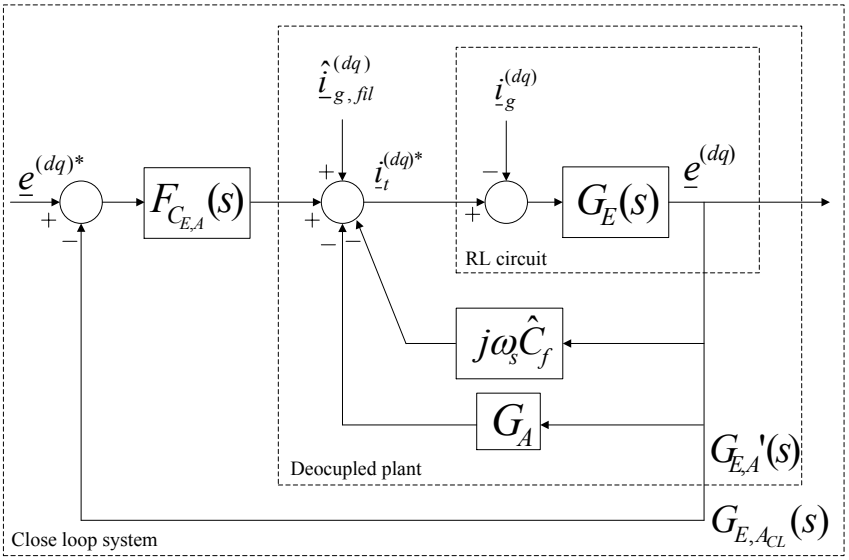

Fig. 4.8 Block diagram of the PCC voltage control based PI controller and active.

control of the PCC voltage $\underline{e}$ shown in Fig. 4.3 in steady-state. In order to avoid feeding high-frequency current transients into the reference voltage when calculating the voltage drop over the interface inductor, a LFP can be placed when feed-forwarding the terminal current. In this control mode, the terminal voltage of the converter can be calculated as:

$$\underline{u}^{(\mathrm{dq})^*} = \underline{e}_{\mathrm{LVRT}}^{(\mathrm{dq})^*} + \hat{\underline{i}}_{\mathrm{t}}^{(\mathrm{dq})}\left(\frac{\alpha_{\mathrm{fil}}}{s+\alpha_{\mathrm{fil}}}\right)(\hat{R}_{\mathrm{f}} + j\omega_{\mathrm{s}}\hat{L}_{\mathrm{f}}) \tag{4.42}$$

where α_{fil} is the bandwidth of the LPF. Similarly, a discrete form of the open loop voltage controller including filter compensation is written as follows:

$$\underline{u}^{(\mathrm{dq})^*}(k) = \underline{e}_{\mathrm{LVRT}}^{(\mathrm{dq})^*}(k) + \hat{\underline{i}}_{\mathrm{t,fil}}^{(\mathrm{dq})}(k)(\hat{R}_{\mathrm{f}} + j\omega_{\mathrm{s}}\hat{L}_{\mathrm{f}}) \tag{4.43}$$

where $\hat{\underline{i}}_{\mathrm{t,fil}}^{(\mathrm{dq})}(k)$ is the estimated converter terminal current passed through a low bandwidth LPF, (see Section 4.4.2 for the derivation of a discrete first-order LPF).

Observe that when the parameters of the interface inductor are used in (4.43), the voltage is controlled where the PCC is defined in Fig. 4.3, thus, upstream from the terminal voltage $\underline{u}$. Moreover, if the current $\underline{i}_{\mathrm{g}}$ is measured, the same approach can be used when the voltage at the primary of the transformer T1 needs to be controlled in steady-state. For simplicity, (4.41) will be used later in this thesis when open-loop control is adopted.

Comparison of the devised PCC voltage controllers

Finally, in Fig. 4.7 it is given a graphical comparison between the step response of the devised close-loop voltage control transfer functions when using both P-based controller and PI-based

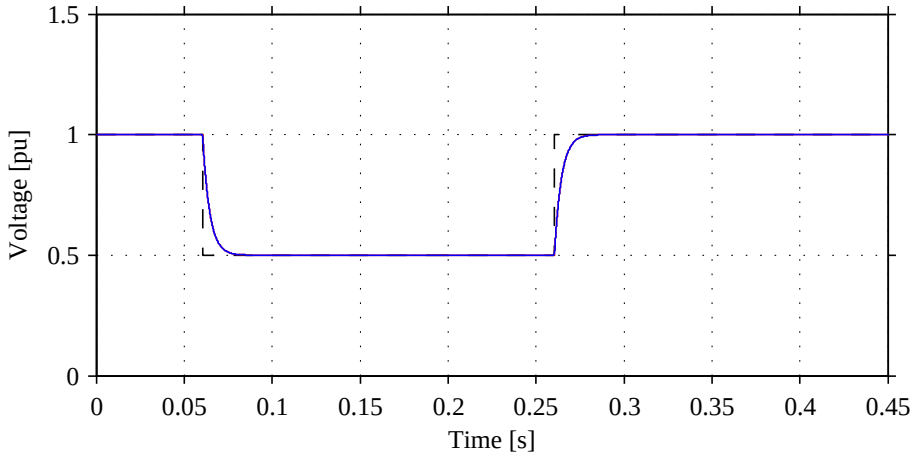

Fig. 4.9 Step response of an ideal close-loop voltage controller trasnfer functions: reference voltage (dashed balck); controlled voltage using proportional controller (blue); and controlled voltage using PI controller with active damping (red).

controller with active damping. The results shown in this section are obtained by using the simulation software PSCAD/EMTDC v4.2 [45].

From Fig. 4.9, it is noticeable that ideally both controller shows the same response. This is expected, as both controllers were devised by shaping the close-loop system into a first order system with bandwidth α_{e}, as given in (4.25) and in (4.36).

In Fig. 4.10(a) is given the step response of the implemented PCC voltage controller when the test equipment is operating with no load ($\underline{i}_{\mathrm{g}}$ = 0 pu). The blue traces in Fig. 4.10(a) represent the PCC voltage when the open-loop voltage controller given in Section 4.4.2 is used. Observe that in order to give a step reference to the voltage controller, no LPF or ramp-rate limiter is used over the reference voltage $\underline{e}^{*}$. When using open-loop control directly in the collector-VSC of the test equipment, the three-phase current $\underline{i}_{\mathrm{t}}$ defined in Fig. 4.2 flows freely across the interface inductor $L_{\mathrm{f}}R_{\mathrm{f}}$ without any control action from the VSC. On the other hand, the band-reject filter bank at the PCC is constituted by two arrays of RLC circuits. For these reason, the interaction between the inductive and capacitive components at collector circuit gives, as a result, a poorly damped oscillatory response at 415 Hz in the PCC voltage, as shown with blue traces in Fig. 4.10(a).

With reference to Fig. 4.10(a), the green traces correspond to the response of the PCC voltage when the proportional controller given in (4.39) is used. It is of interest to observe that the pre-event and post-event PCC voltage does not reach 1 pu. Observe that only the capacitive effect of the filter bank depicted in Fig. 4.2 has been considered when modelling the simplified system shown in Fig. 4.3 for deriving the proportional PCC voltage controller. For this reason a steady-state error is always present in the controlled voltage. Note that when controlling a non loss-less system, the assumption made in Section 4.4.2 when deriving a pure proportional controller does not represent the actual the physical system. For this reason, the step response of the close-loop system $G_{\mathrm{E_{CL}}}(s)$ is not shaped as a first order LPF. Moreover, the step response of the voltage at 0 s and 0.2 s are not as expected to be, taking a considerable 20 ms to reach steady state compared with the theoretical value of 9 ms (given for a controller bandwidth of $\alpha_{\mathrm{e}} = 250$

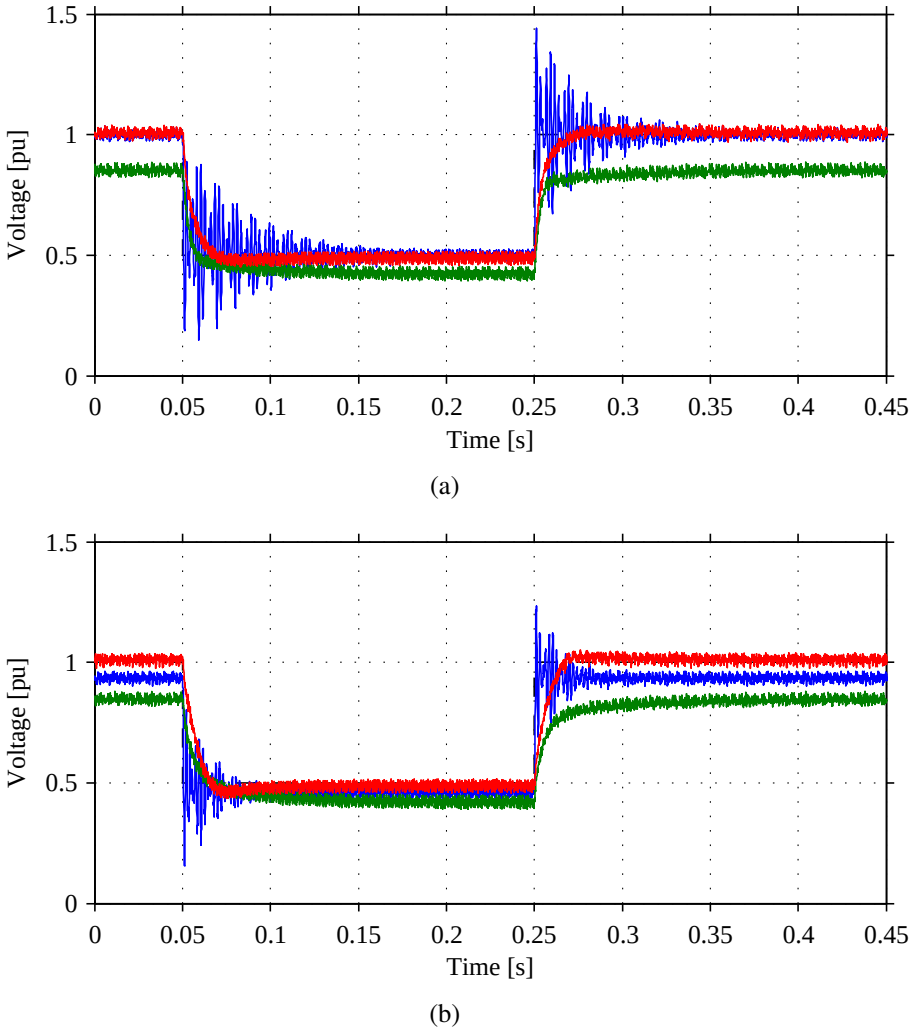

Fig. 4.10 Step response of the PCC voltage when using discrete voltage controller with: (a) no load at the collector-VSC ($\underline{i}_g = 0$) and (b) an RL load ($\underline{i}_g$ is nominal). In plots: reference voltage (dashed balck); controlled voltage using open-loop control (blue); controlled voltage using proportional controller (green); and controlled voltage using PI controller with active damping (red).

[rad/s]), meaning that the system became over-damped.

The red traces in Fig. 4.10(a) correspond of the step response of the PCC voltage when the PI controller and active damping Ga given in (4.39) is implemented. The use of the integrator removes the steady-state error, fixing the actual voltage to its reference in steady-state. Moreover, the step response has a rise time of 12 ms, which is close to the theoretical value of 9 ms. This difference is due to the fact that the controller has no knowledge of the filter losses present in the filter bank connected at the PCC. However, the use of integrator and virtual resistor in the control-loop results in a more accurate first order step response.

In the following, an RL load is connected at the collector-side VSC. Here, the effect of the feed-forward of the current $\hat{\underline{i}}_g$ is investigated. The response of the PCC voltage when an RL load is connected at the primary of the transformer T1 (see Fig. 4.3) is depicted in Fig. 4.10(b). The

RL load is set in order to demand rated current from the VSC, according to the data given in Table 4.1. Observe that both P and PI controller show slightly different response as compared with Fig. 4.10(a) when RL load is not connected. These 3 to 5 extra milliseconds in the rise-time of the response of the PCC voltage is due to the delay introduced by the sampling of the current $\hat{\underline{i}}_{\mathrm{g}}$ in (4.40) and (4.29). Observe that the filtered current becomes part of the current reference for the inner current controller, which also introduces delay when controlling the actual current.

When using OL control over in the test equipment, the resonance between the filters still is present in the dynamic response of the voltage, however, the resonance is much more damped as compare with the no-load test. Here, it is expected that the current needed to charge the capacitor C_{f} is small compared to the currents $\underline{i}_{\mathrm{t}}$ and $\underline{i}_{\mathrm{g}}$ that flow into the load. Moreover, the resistive part of the load also contributes to the damping at the LC equivalent circuit formed between the filter capacitance C_{f} and the interface inductor L_{f} at the collector-side VSC.

It is of interest to observe in Fig. 4.10(b) that the P-base controller exhibits the same performance as in Fig. 4.10(a) and that the same steady-state error is seen in the controlled voltage. This is due to the fact that the filter losses have not been taken into account by the controller, independently of the current $\underline{i}_{\mathrm{g}}$. Finally, note that when the OL-controller (blue traces) without steady-state filter compensation, a steady-state error is seen at the PCC voltage. Moreover, the sign of the error is strictly dependent of the power flow at the collector-VSC. If the current $\underline{i}_{\mathrm{g}}$ changes direction, a slight over-voltage is expected at the PCC.

4.5 Control of the grid-VSC of the testing equipment

In this section the focus is on the grid-side VSC of the testing equipment. The main control blocks that constitute the implemented discrete controller are the DC voltage control and the inner current controller. Similar to the previous sections, the controller has been developed in the synchronously rotating dq frame [42] by applying the IMC method.

The structure of the cascaded controller structure is shown in Fig. 4.11. In this case, a DC voltage control generates the reference current for the inner-current controller of the converter. Similarly, the output of the current controller is the reference value for the output voltage of the VSC. In the following, the implemented cascaded control strategy will be described in detail.

4.5.1 Current control in grid-side VSC

The current control in the grid-side VSC share the same structure of the current control for the collector-side VSC. Similar to (4.1), the dynamics of the current that flows in the filter $L_{\mathrm{f,g}}$ can be expressed as

$$\frac{d\underline{i}_{t,g}^{(dq)}}{dt} L_{\mathrm{f,g}} + \left(j\omega_{\mathrm{g}} L_{\mathrm{f,g}} + R_{\mathrm{f,g}}\right) \underline{i}_{\mathrm{t,g}}^{(dq)} = \underline{e}_{\mathrm{g}}^{(dq)} - \underline{u}_{\mathrm{g}}^{(dq)} \tag{4.44}$$

from (4.44), and by applying the same IMC method including discretization of the controller and

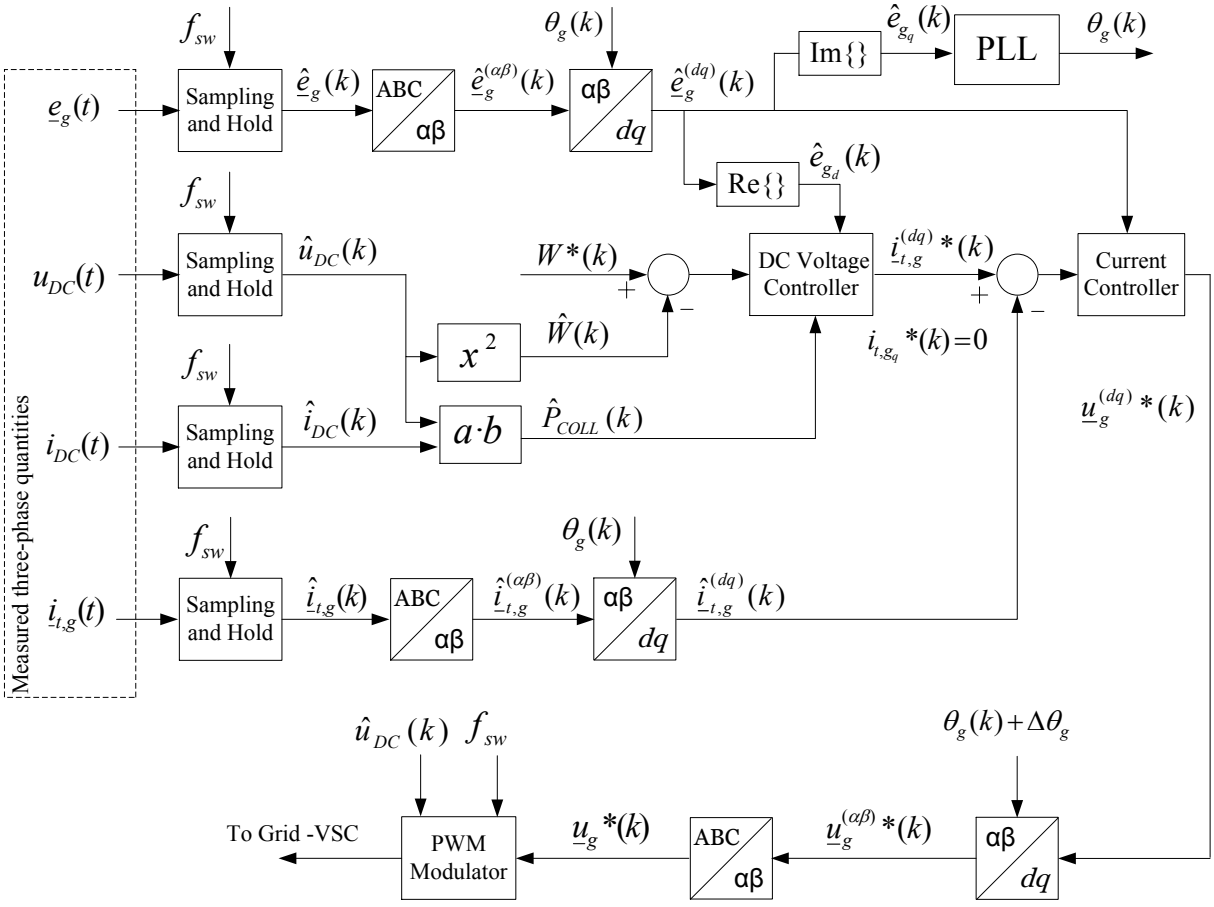

Fig. 4.11 Block diagram of the cascaded vector controller for the grid-VSC of the testing equipment.

anti-windup function for the integrator, as described in Section 4.4.1, the following control law is found:

$$\underline{u}_{\mathrm{g}}^{(\mathrm{dq})^*}(k) = \underline{\hat{e}}_{\mathrm{g}}^{(\mathrm{dq})}(k) + j\omega_{\mathrm{g}}\hat{L}_{\mathrm{f,g}}\underline{\hat{i}}_{\mathrm{t,g}}^{(\mathrm{dq})}(k) + k_{\mathrm{p_{Ig}}}\underline{\epsilon}_{\mathrm{Ig}}^{(\mathrm{dq})}(k) + \underline{I}_{\mathrm{Ig}}(k) \tag{4.45}$$

with

$$\underline{\epsilon}_{\mathrm{Ig}}^{(\mathrm{dq})}(k) = \underline{i}_{\mathrm{t,g}}^{(\mathrm{dq})^*}(k) - \underline{\hat{i}}_{\mathrm{t,g}}^{(\mathrm{dq})}(k) \tag{4.46}$$

as the current error in discrete form at the instant k, where $\underline{u}_{\mathrm{g}}^{(\mathrm{dq})^*}$ is the reference grid-side converter voltage and $\underline{\hat{e}}_{\mathrm{g}}^{(\mathrm{dq})}$ is the estimated grid voltage at the secondary of the grid-coupling transformer $T2$.

Finally, the PI controller gain are $k_{\mathrm{p_{Ig}}} = \alpha_{\mathrm{cc,g}} L_{\mathrm{f,g}}$ and $k_{\mathrm{i_{Ig}}} = \alpha_{\mathrm{cc,g}} R_{\mathrm{f,g}}$, with $\alpha_{\mathrm{cc,g}}$ = 2500 [rad/s]

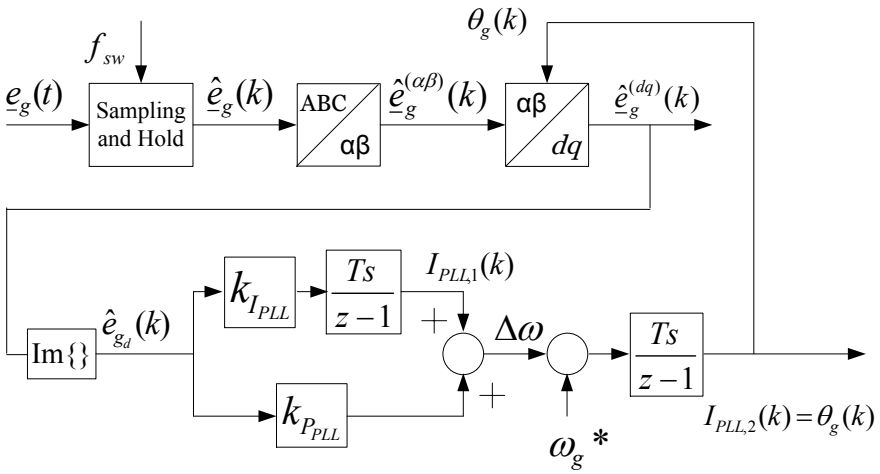

Fig. 4.12 Block diagram of the implemented PLL in the grid-side VSC of the test equipment.

4.5.2 Phase locked loop

In the grid-VSC of the testing device, a Phase Locked Loop (PLL) such as the one described in [42] is used to synchronize the VSC with the grid voltage $\underline{e}_{\mathrm{g}}^{(dq)}$. With reference to the system shown in Fig. 4.3 and calling $\omega_{\mathrm{g}}^{*} = 2\pi 50$ [rad/s] the reference angular frequency of the grid, the equations that governs the PLL in Laplace form can be formulated as

$$\theta_{\mathrm{g}} = \frac{1}{s}(\omega_{\mathrm{g}}^{*} + \Delta\omega_{\mathrm{g}}) \tag{4.47}$$

where θ_{g} is the instantaneous position of the estimated grid voltage vector $\underline{\hat{e}}_{\mathrm{g}}^{(dq)}$, and $\Delta\omega_{\mathrm{g}}$ is expressed as

$$\Delta\omega_{\mathrm{g}} = \left(k_{\mathrm{pPLL}} + \frac{k_{\mathrm{iPLL}}}{s}\right)\hat{e}_{\mathrm{gd}} \tag{4.48}$$

As suggested in [42], the parameter of the PI controller are selected as $k_{\mathrm{pPLL}} = 2\alpha_{\mathrm{PLL}}$ and $k_{\mathrm{iPLL}} = \alpha_{\mathrm{PLL}}^2$, where $\alpha_{\mathrm{PLL}} = 0.1\omega_{\mathrm{g}}^{*}$. Observe that the selection of the bandwidth of the PLL is a trade-off between fast detection of the voltage angle and the ability of rejecting grid disturbances. Moreover, a reduced bandwidth is sufficient since this PLL is on the grid-side of the testing equipment, assuming that the grid voltage is stable during the test.

The discrete calculation of the instantaneous position θ_{g} is written as follows:

$$\theta_{\mathrm{g}}(k) = I_{\mathrm{PLL},2}(k) \tag{4.49}$$

$$I_{\mathrm{PLL},2}(k+1) = I_{\mathrm{PLL},2}(k) + Ts(\omega_{\mathrm{g}}^{*} + \Delta\omega_{\mathrm{g}}(k)) \tag{4.50}$$

where $I_{\mathrm{PLL},2}$ is the result of the discrete integration of the angular reference frequency added to the output of the PI controller $\Delta\omega_{\mathrm{g}}(k)$ expressed as

$$\Delta\omega_{\mathrm{g}}(k) = k_{\mathrm{p_{PLL}}}\hat{e}_{\mathrm{g_d}}(k) + I_{\mathrm{PLL},1}(k) \tag{4.51}$$

with $I_{\mathrm{PLL},1}$ as output of the discrete integrator of the PI controller described as

$$I_{\mathrm{PLL},1}(k+1) = I_{\mathrm{PLL},1}(k) + Tsk_{\mathrm{i_{PLL}}}\hat{e}_{\mathrm{g_d}}(k) \tag{4.52}$$

The block scheme of the implemented PLL is shown in Fig. 4.12.

4.5.3 DC voltage control

The DC voltage controller of the test equipment is placed at the grid-side VSC. The DC-link voltage v_{DC} is controlled by exchanging active power with the AC grid. The voltage across the capacitor C_{DC} is controller by varying the energy stored E_{DC} [42]. The stored energy can be formulated as

$$E_{\mathrm{DC}} = \frac{1}{2}C_{\mathrm{DC}}v_{\mathrm{DC}}^2 \tag{4.53}$$

By deriving 4.53, it is possible to define the variation of energy store in the capacitor in terms of the difference between the input and output power flow in the DC-link. Hence, the variation of energy content will depend on the transferred power from the collector-side VSC of the test equipment P_{COLL} into the DC-link, and the active power P_{GRID} delivered from the DC-link into the AC network. Substituting $W = v_{\mathrm{DC}}^2$ in (4.53), we get:

$$\frac{1}{2}C_{\mathrm{DC}} = \frac{dW}{dt} = P_{\mathrm{COLL}} - P_{\mathrm{GRID}} \tag{4.54}$$

By transforming 4.54 into Laplace form, the transfer function between the capacitor power and W can be written as:

$$\frac{W(s)}{P_{\mathrm{COLL}}(s) - P_{\mathrm{GRID}}(s)} = \frac{2}{sC_{\mathrm{DC}}} \tag{4.55}$$

As suggested in [42], a proportional controller is used to keep the close-loop transfer function as a first order system. The error is defined as the difference between the square of the reference voltage i.e.: $W^* = (v_{\mathrm{DC}}^*)^2$ and the square of the estimated capacitor voltage $\widehat{W}$. By applying the IMC method, the complete control law is found to be:

$$P_{\mathrm{GRID}}^* = (W^* - \widehat{W})k_{\mathrm{p_{DC}}} + \widehat{P}_{\mathrm{COLL}} \tag{4.56}$$

where P_{GRID}^* is the active power reference of the testing equipment, $\widehat{P}_{\mathrm{COLL}} = \hat{v}_{\mathrm{DC}}\hat{i}_{\mathrm{DC}}$ and $k_{\mathrm{p_{DC}}} = -\alpha_{\mathrm{DC}}\widehat{C}_{\mathrm{DC}}/2$. As suggested in [43], the bandwidth of the DC voltage controller is

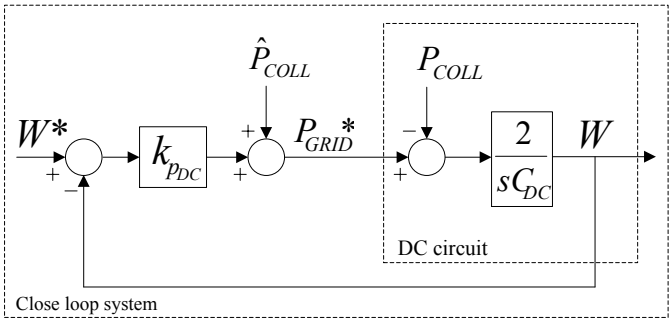

Fig. 4.13 Block diagram of the implemented DC-link voltage controller in the grid-side VSC of the test equipment.

selected to be 10 times smaller than the bandwidth of the current controller $\alpha_{\mathrm{cc,g}}$, thus α_{DC} = 250 [rad/s]. A block diagram of the implemented DC voltage controller is given in Fig. 4.13.

Finally, the direct-axis current reference of the grid-side VSC using amplitude-invariant Clark's Transformation (see Appendix A) is calculated as:

$$i^*_{\mathrm{t,g_d}} = \frac{2}{3}\frac{P^*_{\mathrm{GRID}}}{\hat{e}_{\mathrm{g_d}}} \tag{4.57}$$

where $\hat{e}_{\mathrm{g_d}}$ is the direct component of the estimated grid voltage vector $\underline{\hat{e}}^{(dq)}_{\mathrm{g}}$.

The discretization of the DC voltage controller has been done with the same procedure given in Section 4.4.1 and Section 4.4.2. The discrete control law is written as follows.

$$P^*_{\mathrm{GRID}}(k) = (W^*(k) - \widehat{W}(k))k_{\mathrm{pDC}} + \widehat{P}_{\mathrm{COLL}}(k) \tag{4.58}$$

and

$$i^*_{\mathrm{tg_d}}(k) = \frac{2}{3}\frac{P^*_{\mathrm{GRID}}(k)}{\hat{e}_{\mathrm{g_d}}(k)} \tag{4.59}$$

As suggested in [42], In order to remove steady-state error in the DC-link voltage, an integrator term with a relatively small gain (compared with the time constant of the DC-link capacitor) has been used.

Figure 4.14 shows the step-response of the estimated voltage $\hat{v}_{\mathrm{DC}}$. From the figure, it is observable that the mathematical model is accurate, and that the actual voltage follows the reference accordingly. Finally, the reactive current reference of the grid-side VSC is controlled in zero, thus, $i^*_{\mathrm{t,g_q}}(k) = 0$.

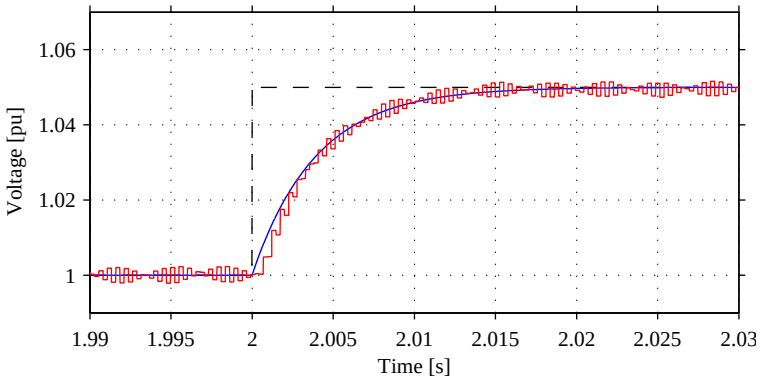

Fig. 4.14 Normalized step response of the DC-link voltage controller: voltage reference (black dashed); voltage output of the mathematical model (blue); and simulated voltage $\hat{v}_{\mathrm{DC}}$ of the test equipment (red).

4.6 Wind turbine modeling

In this section, the modeling of the wind turbine is presented. A general description of an FPC wind turbine is found in Section 2.2.3. In this thesis, only the DC-link and collector-side of the wind turbine has been modeled. A schematic of the implemented wind turbine model is shown in Fig. 4.15.

Reference [6] provides actual measurements of a 4 MW FPC wind turbine rotor speed with its corresponding wind speed over a 300 s window. The generated power is also measured over the same time period. Here it is assumed that, due to the large rotor inertia, the rotational speed of the wind turbine is kept constant if a voltage dip occurs at its terminals [6]. For this reason, the generator and generator-side VSC are modeled by a current source in parallel with the DC-link capacitor. The reference of the controlled current source is set according to an equivalent generated power P^*_{GEN} delivered by the generator-VSC into the DC-link. The magnitude of the DC current source can be calculated by the simple expression

$$i^*_{\mathrm{s}} = \frac{P^*_{\mathrm{GEN}}}{\hat{v}_{\mathrm{DC,w}}} \tag{4.60}$$

where P^*_{GEN} is the reference generator power, and $v_{\mathrm{DC,w}}$ is the voltage across the wind turbine DC-link capacitor $C_{\mathrm{DC,w}}$. The collector-side VSC of the wind turbine is modeled with a 3-phase VSC with ideal switches triggered by a PWM modulator, as shown in Fig. 4.15. The converter is interfaced with the imposed AC grid through a filter inductor $L_{\mathrm{f,w}}$ with internal resistance $R_{\mathrm{f,w}}$, and shunt capacitor $C_{\mathrm{f,w}}$, where the voltage $\underline{e}_{\mathrm{w}}$ is measured. The VSC voltage is labelled as $\underline{u}_{\mathrm{w}}$ and the VSC terminal current is labelled as $\underline{i}_{\mathrm{t,w}}$. Additionally, the generating unit is interconnected with the test equipment in the secondary side of the wind turbine transformer. Here, the voltage $\underline{e}_{\mathrm{w,g}}$ and the current $\underline{i}_{\mathrm{w,g}}$ are defined.

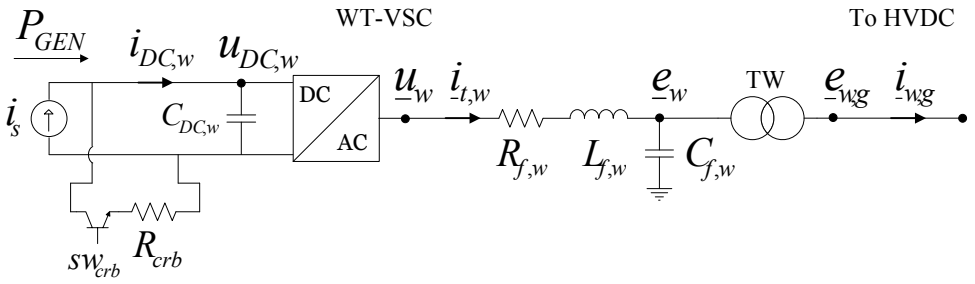

Fig. 4.15 Simplified single-line diagram of the modeled FPC wind turbine.

4.6.1 Control of the FPC wind turbine

With reference to Fig. 4.15, the controller has been developed in the synchronously rotating dq frame; the control structure is shown in Fig. 4.16. It is constituted by a DC voltage controller that maintains the DC-voltage to its reference value and a LVRT control strategy that reacts by injecting reactive current in case of a voltage dip. In the inner loop there is the classical current controller also described in Section 4.4.1. The switching frequency is $f_{\mathrm{sw,w}}$ = 2500 [Hz], and the sampling frequency is $f_{\mathrm{s,w}}$ = 5000 [Hz]. A PLL similar to the one described in Section 4.5.2 is used to maintain synchronism with the imposed voltage. The PLL bandwidth $\alpha_{\mathrm{PLL_w}}$ is set to 30 [rad/s]. The parameters of the modelled wind turbine are given in Table 4.2.

Current control

The current control of the wind turbine model including discretization and anti-windup for the integrator function have been also implemented with the same methodology given in Section 4.4.1. In (4.61) is written the discrete form of the wind turbine current controller.

$$\underline{u}_{\mathrm{w}}^{(\mathrm{dq})^*}(k) = \underline{\hat{e}}_{\mathrm{w}}^{(\mathrm{dq})}(k) + j\omega_{\mathrm{s}}\hat{L}_{\mathrm{f,w}}\underline{\hat{i}}_{\mathrm{t,w}}^{(\mathrm{dq})}(k) + k_{\mathrm{pI_w}}\underline{\epsilon}_{\mathrm{Iw}}^{(\mathrm{dq})}(k) + \underline{I}_{\mathrm{Iw}}(k) \tag{4.61}$$

with

TABLE 4.2. WIND TURBINE PARAMETERS.

Base values		4.5 MVA, 10 kV
WT-VSC filter inductance	$L_{\mathrm{f,w}}$	0.15 pu
WT-VSC filter internal resistance	$R_{\mathrm{f,w}}$	0.015 pu
WT-VSC filter capacitance	$C_{\mathrm{f,w}}$	7.5 pu
Transformer TW impedance	$X_{\mathrm{tr,w}}$	0.08 pu
DC-link capacitor size	$C_{\mathrm{DC,w}}$	0.015 pu
DC-link crowbar resistor	R_{crb}	1 pu
VSC switching frequency	$f_{\mathrm{sw,w}}$	2500 Hz
Sampling time	$t_{\mathrm{s,w}}$	0.2 ms

$$\underline{\epsilon}_{\mathrm{Iw}}^{(\mathrm{dq})}(k) = \underline{i}_{\mathrm{t,w}}^{(\mathrm{dq})^*}(k) - \underline{\hat{i}}_{\mathrm{t,w}}^{(\mathrm{dq})}(k) \tag{4.62}$$

as the current error.

By using the same methodology when deriving the current control given in the previous section, the PI controller gains are found to be $k_{\mathrm{p_{Iw}}} = \alpha_{\mathrm{cc,w}} L_{\mathrm{f,w}}$ and $k_{\mathrm{i_{Iw}}} = \alpha_{\mathrm{cc,w}} R_{\mathrm{f,w}}$, with $\alpha_{\mathrm{cc,w}}$ = 3000 [rad/s].

Finally, the reference voltage $\underline{u}_{\mathrm{w}}^{(\mathrm{dq})^*}(k)$ is transformed into three-phase quantities and sent into a PWM modulator to calculate the switching signal of the wind turbine VSC.

DC voltage control

The discrete control of the DC voltage controller has been derived with the same procedure given in Section 4.5.3. Calling $W_{\mathrm{w}} = v_{\mathrm{DC,w}}^2$, the power reference $P_{\mathrm{WT}}^*(k)$ of the wind turbine converter is:

$$P_{\mathrm{WT}}^*(k) = (W_{\mathrm{w}}^*(k) - \widehat{W_{\mathrm{w}}}(k)) k_{\mathrm{p_{DC,w}}} + P_{\mathrm{GEN}}(k) \tag{4.63}$$

The active current reference $i_{\mathrm{tw_d}}^*(k)$ is calculated as

$$i_{\mathrm{t,w_d}}^*(k) = \frac{2}{3} \frac{P_{\mathrm{WT}}^*(k)}{\hat{e}_{\mathrm{w_d}}(k)} \tag{4.64}$$

where P_{GEN}^* is the active power reference used to calculate the reference current i_{s}^* in (4.60). The proportional gain is $k_{\mathrm{p_{DC,w}}} = -\alpha_{\mathrm{DC,w}} \widehat{C}_{\mathrm{DC,w}}/2$, and the bandwidth of the DC voltage controller is set to ten times smaller than the bandwidth of the current control, thus, $\alpha_{\mathrm{DC,w}}$ = 300 [rad/s]. Finally, the complete control scheme is shown in Fig. 4.16.

4.6.2 LVRT strategy

When a grid fault occurs in the power system resulting in a sudden voltage variation at the connection point of the wind power plant, modern wind turbines must be capable to ride-through the corresponding voltage dip seen at its terminals, if the disturbance is within the specification of the LVRT profile given in the grid code. In this scenario, the TSO requires that the wind power plant remains in service.

The control strategies implemented in modern wind turbines can be classified in two main actions: hardware protection of the converter, and AC voltage support by current control [13].

Current control during LVRT

The wind turbine modelled in this thesis is equipped with a current control strategy that provides reactive power support during a voltage dip. Depending on the retained voltage at the PCC, the

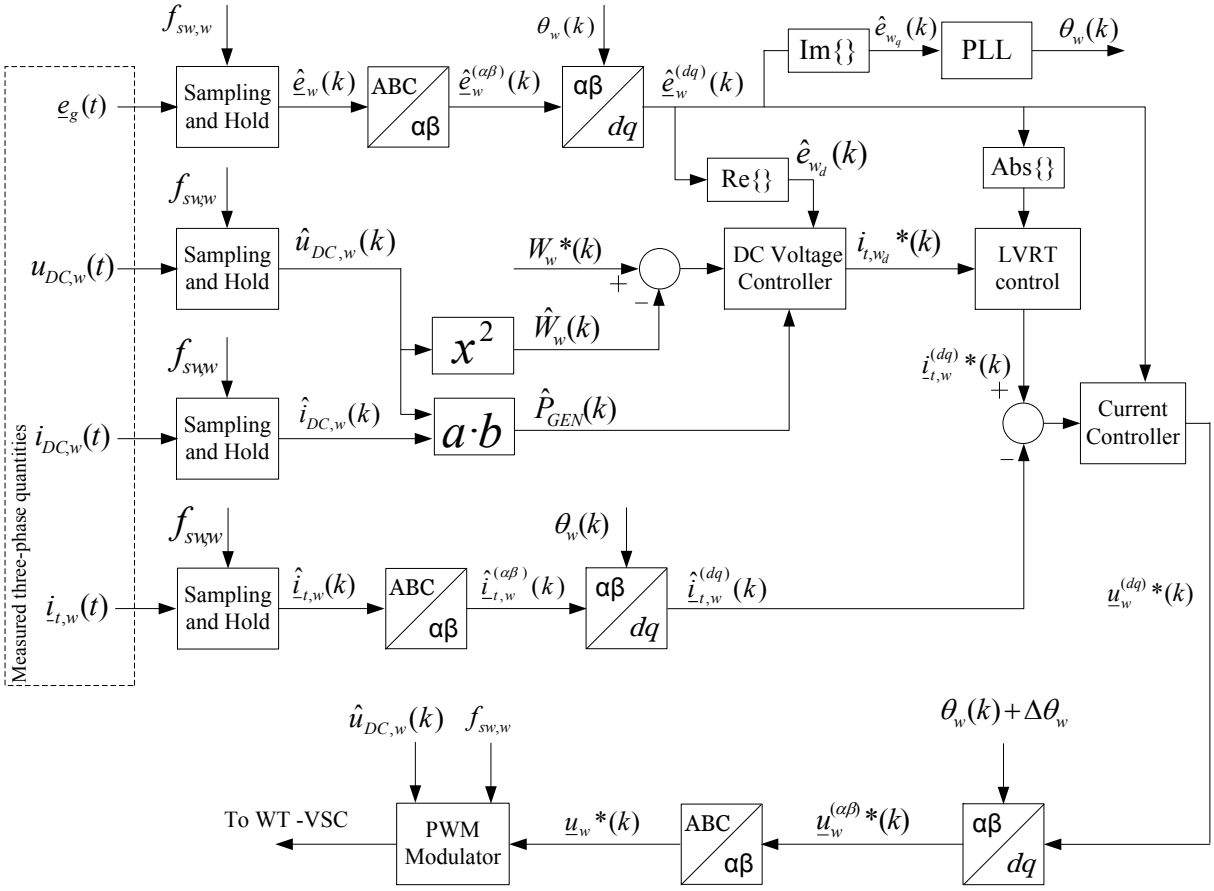

Fig. 4.16 Block diagram of the cascaded vector controller for the FPC wind turbine.

active current reference $i^*_{\mathrm{t,w_d}}$ can be limited in order to give room for the pre-calculated reactive current $i^*_{\mathrm{t,w_q}}$. In case of a severe voltage dip, the current contribution into the fault can be rapidly controlled by the grid-side VSC of the FPC-based wind turbine.

Here, a predefined voltage/current profile is used to calculate the reactive current reference. The set value of the current is dependent on the retained voltage at the terminals of the wind turbine. For instance, in the German grid code [17] and Danish grid code [22] it is specified that 1 pu of reactive current must be injected when the system voltage is below 0.5 pu.

When the voltage is restored within the normal operation range, voltage support must be maintained for an additional 500 ms, for example, according to the German grid code [17]. Once the reactive current reference is set to its pre-fault value, the LVRT control slowly removes the limitation in the active current, restoring normal active power production of the wind turbine. Finally, in case that reactive power production is not allowed by the TSO during a voltage dip [23], the active current must be controlled within the current limits of the VSC.

Hardware protection

Hardware protection is used to limit the energy stored in the DC capacitor in the wind turbine back-to-back converter, thus, preventing dangerous over-voltages in the DC-link of the wind turbine [13]. The protection system is provided by crowbars connected to the DC-link, as shown in Fig. 4.15.

The crowbar, also called DC chopper, is constituted by a braking resistor which dissipates the excess of energy delivered by the generator into the DC-link. A power electronic switch (typically, a set of IGBTs) allows the current i_{s} to deviate through the resistor R_{crb}.

An hysteresis control is used to generate the gate signal of the power electronic switch. The protection system of the wind turbine is constantly monitoring the instantaneous voltage $\hat{v}_{\mathrm{DC,w}}$. A control is activated when the voltage exceeds its maximum safe value (typically 1.2 pu) [13], allowing the capacitor $C_{\mathrm{DC,w}}$ to be immediately discharged into the resistor. By this means, the capacitor $C_{\mathrm{DC,w}}$ can be protected.

The resistor is dimensioned in such way that it can dissipate full power production of the wind turbine for approximately one second. Here, its impedance is calculated so the current that flows through the switch is in proximity to the nominal current of the VSC.

4.7 Conclusion

In this chapter the control functions of the wind turbine and the test equipment have been given in detail, with special focus on the AC voltage control of the applied voltage at the PCC, and on the LVRT control strategy implemented in the wind turbine model.

Finally, it is of importance to ensure a safe interaction between the wind turbine and the converter-based test equipment. For this reason, a stability analysis of the system in steady state condition is presented in Chapter 5. Moreover, the transient stability of the testing method is discussed in Chapter 6.

Chapter 5

Stability analysis

5.1 Introduction

In the investigated testing setup, the VSC-based testing equipment is a controllable voltage source, and it is required to present a stable operation both dynamically and under steady-state conditions. This is of high importance, especially when considering that different wind turbine manufacturers have implemented their own control settings as well as control strategies for operation during a voltage dip.

A potential risk of interaction does not only relate to unstable condition of the system, but also to situations when poorly damped resonances can be triggered in a specific operating condition. For this reason, it is of interest to investigate the stability of the system under consideration. Moreover, the analysis presented in this chapter aims to address the overall stability of the investigated system. Observe that this analysis is strictly dependent on the system parameters and in the control structure of the tested object. Here, the analysis is focused on the risk of interaction between the two investigated controllers of the wind turbine and testing equipment, and to identify the control parameters that mainly impact the location of the system poles.

5.2 Reduced model of the test system

In order to represent the main equations that govern the system dynamics, a reduced electrical model of the testing setup has been derived. As shown in Fig. 5.1, only the collector-side converter of the wind turbine and the collector-side of the test equipment have been considered for the analysis. The DC current source of the wind turbine model and the interface impedance between the testing device and the generation have been also included. Moreover, the output transformer of the wind turbine TW, the AC cable and the coupling transformer T1 of the testing equipment have been represented by the equivalent inductance and resistance L_{eq} and R_{eq}, respectively. The testing equipment VSC is sourced by a fix DC voltage at its DC bus, meaning that the DC-link voltage controller of the grid-VSC of the test equipment is considered ideal and infinitely fast.

With reference to Fig. 5.1, the system parameters are reported in Table 5.1; observe that “WT” and

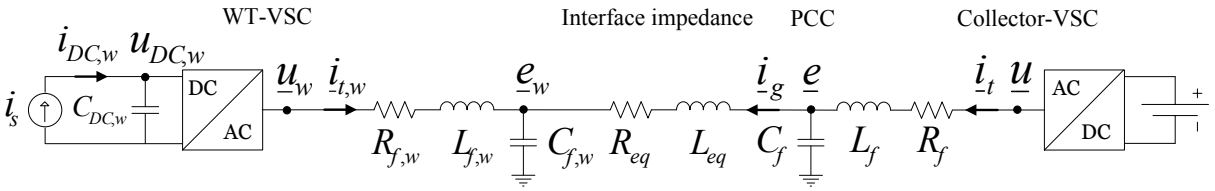

Fig. 5.1 Reduced electrical model of the testing seutp.

"VSC" are used to denote wind turbine and VSC-based test equipment parameters, respectively.

TABLE 5.1. REDUCED SYSTEM MODEL PARAMETERS.

Base values		4.5 MVA, 10 kV
VSC filter inductance	L_{f}	0.06 pu
VSC filter internal resistance	R_{f}	0.006 pu
VSC filter capacitance	C_{f}	4.0 pu
Equivalent interface inductance	L_{eq}	0.14 pu
Equivalent interface resistance	R_{eq}	0.014 pu
WT filter inductance	$L_{\mathrm{f,w}}$	0.15 pu
WT filter internal resistance	$R_{\mathrm{f,w}}$	0.015 pu
WT filter capacitance	$C_{\mathrm{f,w}}$	7.5 pu
PCC voltage control bandwidth in VSC	α_{e}	250 [rad/s]
Current control bandwidth in VSC	α_{cc}	2500 [rad/s]
DC voltage control bandwidth in WT	$\alpha_{\mathrm{dc,w}}$	300 [rad/s]
Current control bandwidth in WT	$\alpha_{\mathrm{cc,w}}$	3000 [rad/s]

The differential equations that describe the physical system shown in Fig. 5.1, and control strategies given in the previous chapter have been linearised around an operating point and represented in state-space form as:

$$\begin{aligned} \dot{\underline{x}}(x) &= A\underline{x}(t) + B\underline{u}(t) \\ \underline{y}(x) &= C\underline{x}(t) + D\underline{u}(t) \end{aligned} \tag{5.1}$$

where matrices A, B, C and D are dependent on the systems parameters, on the control algorithms and on the operating conditions.

The state vector $\underline{x}(t)$ is here represented with vector quantities as:

$$\underline{x}(t) = \begin{bmatrix} \underline{i}_{\mathrm{t}} \\ \underline{e} \\ \underline{i}_{\mathrm{g}} \\ \underline{i}_{\mathrm{g,fil}} \\ \underline{e}_{\mathrm{w}} \\ \underline{i}_{\mathrm{t,w}} \\ W_{\mathrm{DC}} \\ \underline{I}_{\mathrm{I}} \\ \underline{I}_{\mathrm{E}} \\ \underline{I}_{\mathrm{I,w}} \\ \theta_{\mathrm{w}} \\ I_{\mathrm{PLL,w}} \end{bmatrix} \tag{5.2}$$

Similarly, the input vector $\underline{u}(t)$ can be expressed as:

$$\underline{u}(t) = \begin{bmatrix} \underline{e}^* \\ P^*_{\mathrm{GEN}} \\ W^*_{\mathrm{DC}} \\ i^*_{\mathrm{t,w_q}} \end{bmatrix} \tag{5.3}$$

Two operating point $\underline{x}_0$ are found after evaluating the mathematical model of the system shown Fig. 5.1, when the reference generator power defined in (4.60) is set at P^*_{GEN} = 0 pu and P^*_{GEN} = 0.9 pu (4 MW). The reference voltage of the PCC voltage controller $\underline{e}^*$ is set at 1 pu. The reference for the DC-link voltage controller W^*_{DC}=$(v^*_{\mathrm{DC}})^2$ is set at 1 pu (DC) and reference for the reactive current $i^*_{\mathrm{t,w_q}}$ of the grid-side VSC of the wind turbine is set at 0 pu.

The output vector $\underline{y}(t)$ gives information about the value of all states, including the reference active power and active current of the wind turbine, P^*_{WT} and $i^*_{\mathrm{t,w_d}}$, respectively, and the reference current $\underline{i}^*_{\mathrm{t}}$ for the current control of the test equipment. In the following, the impact of the variation of system parameters on the location of the system poles will be analysed and discussed.

Here, the linearised model has been obtained through the software Wolfram Mathematica 8 [46] and evaluated in the simulation software MATLAB 2013b [47]. In the plots, the star represent the initial location of the system poles and the trace represents its displacement when a selected parameter is varied.

5.3 Dependency of system poles with respect to control parameters of the test equipment

The bandwidth of the closed-loop AC voltage controller of the test equipment α_{e} sets the speed of response of the overall system when varying the PCC voltage. Moreover, as described in Section 4.4.2, the close-loop PCC voltage control can either be based on proportional controller

or PI controller. Thus, it is of interest to identify the pole location when selecting a particular control with a given bandwidth α_e.

5.3.1 Impact of the topology of the PCC voltage controller

In (4.27) is given the control law of the PCC voltage controller based on proportional controller with gain $k_{pE} = \alpha_e \hat{C}_f$. Similarly, in (4.34) is given the control law of the PCC voltage controller based on PI controller with gains $k_{pE} = \alpha_e \hat{C}_f$ and $k_{iE} = \alpha_e^2 \hat{C}_f$.

Figure 5.2(a) shows the pole displacement of the investigated system when using PI-based controller and the bandwidth of the voltage controller of the test equipment α_e is varied from 250 to 2500 [rad/s]. The plot show the resulting pole location for two different operating point of the wind turbine: the blue traces correspond to the operating point P^*_{GEN}= 0 pu, and the red traces correspond to the operating point when P^*_{GEN}= 0.9 pu. When increasing the bandwidth α_e maintaining P^*_{GEN} at 0 pu, two pair of complex poles immediately become poorly damped. Observe at the red traces that these two complex poles located in the proximity to the 45 degrees line are located near the origin when the wind turbine operates at full power output. The results in Fig. 5.2(a) also shows that these two pole are within the well damped area when P^*_{GEN}= 0.9 pu for values α_e below 700 [rad/s]. Due to the cascaded structure of the implemented controller illustrated in Fig. 4.4, two complex poles appear to move toward the non-stable region when α_e is in proximity to the current control bandwidth at 2500 [rad/s]. Finally, observe that in the two scenarios shown in Fig. 5.2(a), two complex-poles moves across the real axis when the bandwidth increases.

In Fig. 5.2(b) it is shown the pole location of the system when using proportional controller

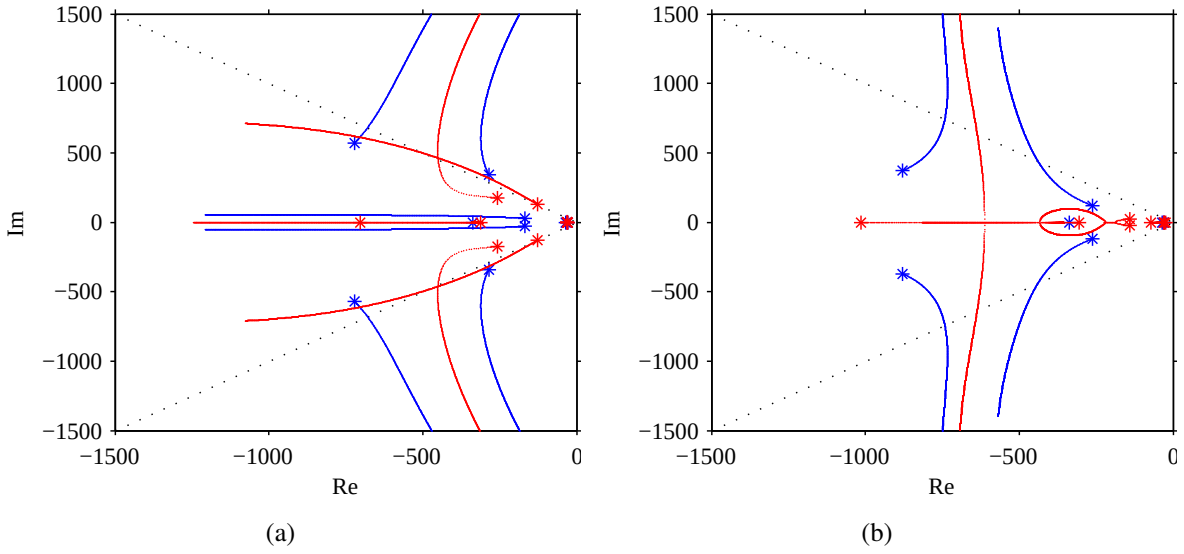

Fig. 5.2 Pole displacement when increasing the bandwidth α_e from 250 [rad/s] to 2500 [rad/s]: Plot (a): using PI controller; Plot (b): using P controller; when the testing equipment is with no load (blue traces) and full load (red traces).

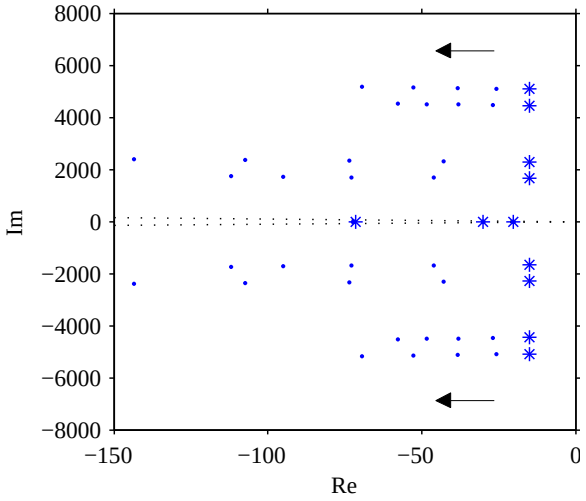

Fig. 5.3 Pole displacement when increasing the power of the wind turbine from 0 pu to 1 pu using open-loop controller in collector-VSC.

for the same sweeping of the bandwidth α_e. Observe that for α_e = 250 [rad/s], the location of the poles for P^*_{GEN} = 0 pu and P^*_{GEN} = 0.9 pu is always below the 45 degrees line. For no-load operation of the turbine (blue traces), two pair of complex poles moves away from the well damped area when α_e increases. For full power operation of the wind turbine at α_e = 250 [rad/s], the system poles are located in proximity to the origin, changing their characteristic frequency and damping. However, when α_e increases at 1000 [rad/s], two of complex pole become poorly damped and continue to move in parallel to the imaginary axis when α_e increases. Finally, it is of interest to observe that for values of α_e close to 250 [rad/s], the use of proportional controller gives a more damped system as compared with PI controller, for the two selected operating point of the wind turbine.

As discussed in Section 4.4.2, an open-loop control of the PCC voltage has been also presented. Observe that for this analysis, the cascaded control structure shown in Fig. 4.4 is not implemented. Therefore, the input vector $\underline{e}^{(dq)^*}$ of the state-space model is here fed as the VSC voltage $\underline{u}^{(dq)}$ shown in Fig. 5.1. The location of the poles is shown for different operating point of the wind turbine from P^*_{GEN} = 0 pu to P^*_{GEN} = 0.9 pu (4 MW). The results are shown in Fig. 5.3.

Observe that for non-load operation, 4 pair of high-frequency complex pole appear in parallel to the imaginary axis. When the wind turbine increases its power output, these poles are moving toward the left-hand side, meaning that the system becomes more damped. This result goes in hand with the results given in Fig. 4.10(a), where the three topologies of PCC voltage controllers are compared. Observe that in both analysis, the system becomes more damped when the current $\underline{i}_g$ (see Fig. 5.1) is nominal.

5.3.2 Impact of the active damping term in PI-based PCC voltage controller

The active damping term contributes to the controllability of the PCC voltage by improving the performance of the controller against voltage disturbances. At the same time, the addition of the virtual resistor G_{A} in the control-loop leads to an increment of the gain of the integrator term in the PI controller. This action could lead to instability, if either the bandwidth α_{e} of the close-loop controller or the size of the virtual resistor are not properly selected.

In Fig. 5.4 it is shown the pole location when varying the bandwidth α_{e} from 250 [rad/s] to 2500 [rad/s], for two different sizes of the virtual resistor: 50% of G_{A} and 10% of G_{A}, corresponding to the blue traces and red traces, respectively. The results are shown in Fig. 5.4. Here, the wind turbine power is set at 0.9 pu.

With focus on the pole location when α_{e} is set at 250 [rad/s], two pairs of complex poles appear to be relocated in proximity to the origin, when the active damping term is varied from 10% to 50% of its value. Observe in Fig. 5.4 that when the active damping G_{A} is set to 50% of $\alpha_{\mathrm{e}}C_{\mathrm{f}}$, the displacement of the poles when varying α_{e} is similar to the case when the full PI controller is used, depicted with red traces Fig. 5.2(a). As expected, when decreasing the damping term to 10% of G_{A}, the pole displacement resembles the case when using the P controller, as depicted in Fig. 5.2(b).

Finally, here it is found that the system is stable for any given value of active damping between 0 and $\alpha_{\mathrm{e}}C_{\mathrm{f}}$. However, as discussed in Section 4.4.2, the virtual resistor plays a key role when deriving an integrator term capable of removing the steady-state error while controlling the PCC voltage in close-loop. Moreover, the addition of active damping in the control-loop improves the robustness of the system against voltage disturbances. For this reason, a virtual resistor of $G_{\mathrm{A}} = \alpha_{\mathrm{e}}C_{\mathrm{f}}$ is recommended.

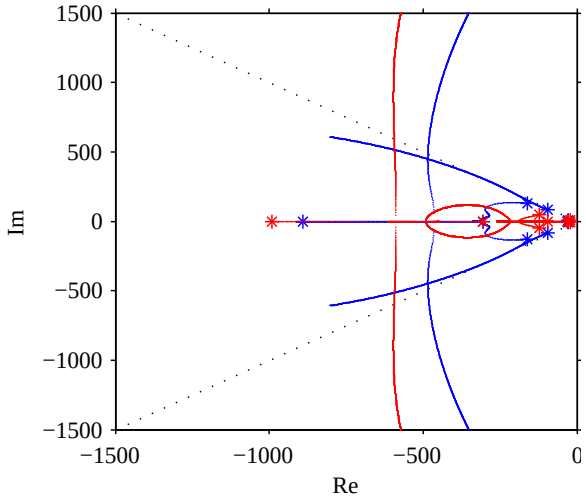

Fig. 5.4 Pole displacement when varying α_{e} is from 250 to 2500 [rad/s]. The blue and red traces correspond to displacement of the system poles when the active damping reduced to 10% ($G_{\mathrm{A}} = 0.1\alpha_{\mathrm{e}}C_{\mathrm{f}}$), and to 50% ($G_{\mathrm{A}} = 0.5\alpha_{\mathrm{e}}C_{\mathrm{f}}$), respectively. The wind turbine power is 0.9 pu.

5.3.3 Impact of the feed-forward of the grid current in close-loop PCC voltage controller

The filtering stage applied to the feed-forward of the estimated grid current $\hat{\underline{i}}_{\mathrm{g}}$ in the close-loop voltage control is required to be fast enough to guarantee good system dynamics. In Fig. 5.5 is shown the displacement of the system poles when increasing the low-pass filter bandwidth α_{fil} in (4.27) and in (4.38) for P-based and PI-based controller, respectively, from 250 [rad/s] to 2500 [rad/s].

In Fig. 5.5(a) it is shown the pole displacement when varying α_{fil} and the P-controller is implemented in the test equipment. The blue curves correspond to the pole location when the wind turbine power is set at 0 pu. Observe that when α_{fil} = 250 [rad/sec], all poles are well-damped. When increasing α_{fil}, the frequency and the damping of the poles vary while maintaining the poles within the well damped area. Note that when the power of the wind turbine is set at 0.9 pu (corresponding to the red traces in Fig. 5.5(a)), a reduced bandwidth of the filter immediately leads to an unstable system. In this scenario, it is crucial to have fast filtering on the feed-forward of the gird current, especially if a pure P-controller is used. The poles become well damped when α_{fil} is set above 1000 [rad/s].

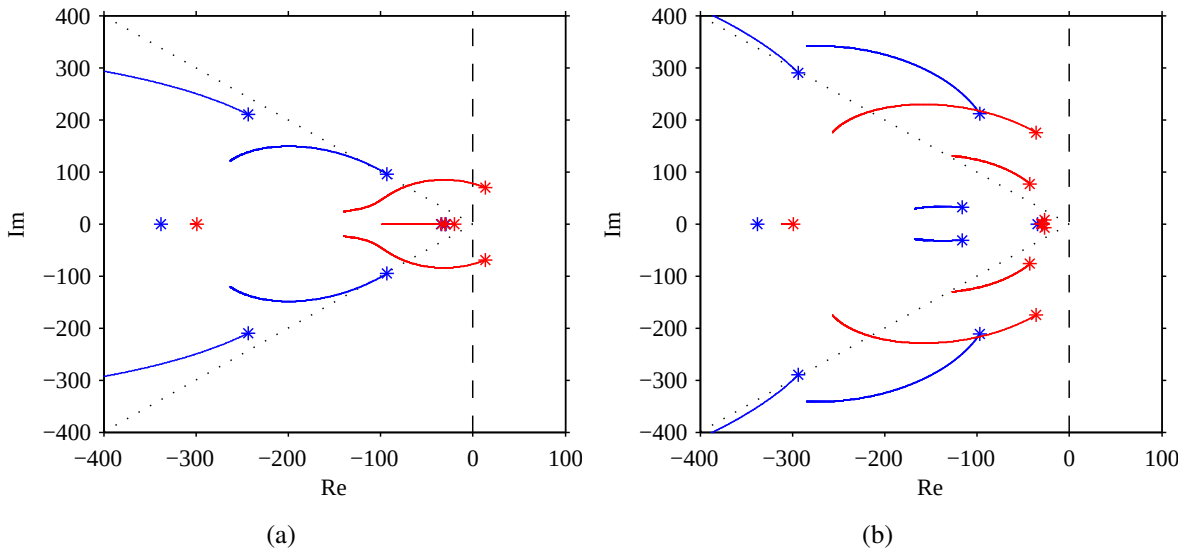

Fig. 5.5 Pole displacement when increasing the LPF bandwidth α_{fil} from 250 [rad/s] to 2500 [rad/s] using Plot (a): P-controller; and Plot (b): PI-controller with active damping; for P^{*}_{GEN} set at 0 pu (blue traces) and P^{*}_{GEN} set at 0.9 pu (red traces).

Figure 5.5(a) shows the pole location when using PI-based controller with active damping for the same sweeping of α_{fil}. Observe that in this scenario, all the poles are located in the left-hand side of the plane, independently of the wind turbine power. When the wind turbine is set to 0 pu (blue traces), two pair of complex poles moves towards the left while still being poorly damped. If the turbine operates at full power (red traces), the two pair of complex poles become well damped when increasing α_{fil} to 2500 [rad/s]. Note that for small values of α_{fil}, the integrator term of the PI controller and the active damping term G_{A} has a beneficial effect on the system performance.

5.4 Dependency of system poles with respect to wind turbine parameters

As previously said, different wind turbine manufacturers have implemented their own control settings as well as control strategies for operation during a voltage dip. For this reason, the stability of the test system must also be investigated for variation on external parameters which are not necessarily related to the control settings of the testing equipment. In the investigated setup, two main parameters has been identified: the bandwidth of the DC-link voltage controller of the wind turbine, which governs the power flow between the wind turbine and the grid , and the interface impedance between the tested object and the testing device. In the following, a sensitivity analysis is carried out, focused on the parameters previously mentioned.

5.4.1 Impact of the DC voltage controller bandwidth of the test object, when using closed-loop and open loop control in test equipment

In this section, the focus is on the impact of the bandwidth of the DC voltage controller of the tested wind turbine. The main control parameter that governs the power flow between the wind turbine and the grid is the bandwidth of the DC voltage controller $\alpha_{\mathrm{DC,w}}$. Here the wind turbine is set to full power operation.

In Fig. 5.6(a) it is shown the pole movement when the $\alpha_{\mathrm{DC,w}}$ is varied from 300 [rad/s] to 3000 [rad/s], for the two investigated close-loop PCC voltage controllers. It is clearly shown that the control bandwidth of the test object impacts mainly the characteristic frequency of two complex poles. These poles become poorly damped when the bandwidth of wind turbine DC voltage

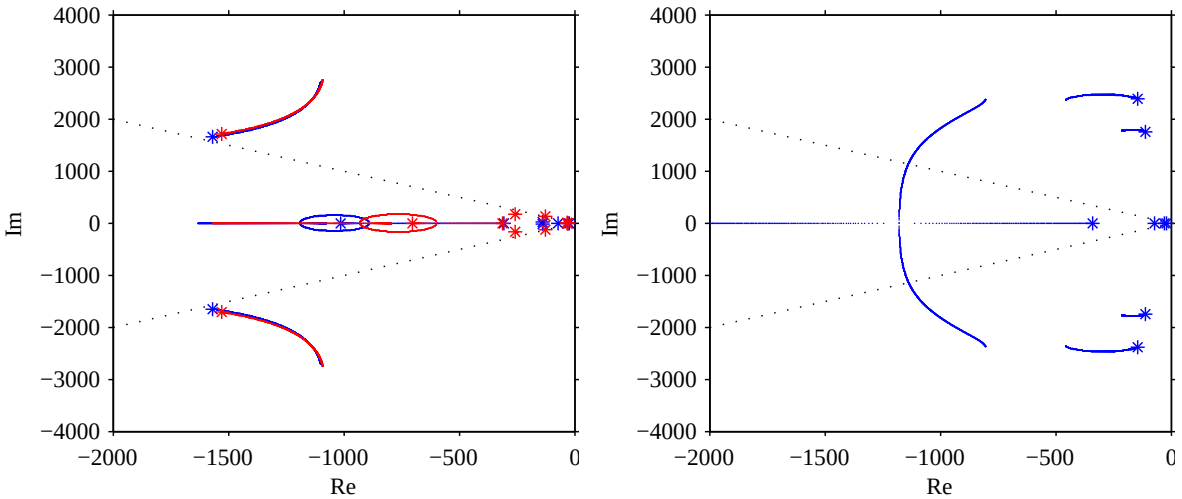

Fig. 5.6 Pole displacement when increasing the bandwidth $\alpha_{\mathrm{DC,w}}$ from 300 [rad/s] to 3000 [rad/s] when using: Plot(a) CL-controller with P (blue) and with PI (red); and Plot (b) OL-control in collector-VSC.

controller $\alpha_{\mathrm{DC,w}}$ increases above 300 [rad/s]. Observe, however, that the topology of the close loop controller has a minor impact on the location of the majority of the poles. Moreover, the damping of the poles located in proximity to the real axis increases when $\alpha_{\mathrm{DC,w}}$ reaches 1500 [rad/s], while the poles located in proximity to the origin remain unchanged against variation of $\alpha_{\mathrm{DC,w}}$.

In Fig. 5.6(b) it is shown the pole movement when varying $\alpha_{\mathrm{DC,w}}$ from 300 [rad/s] to 3000 [rad/s] when using open-loop controller in the test equipment. As seen from the figure, the number of poles has been reduced as compared with the use of close-loop controller, decreasing the order of the system. Observe that when using open-loop control in the test equipment, only high-frequency poles are affected when varying $\alpha_{\mathrm{DC,w}}$. Moreover two pair of poorly damped complex poles appear in proximity to the imaginary axis. Note that the system is more damped against variation of $\alpha_{\mathrm{DC,w}}$ when close-loop controller is used.

5.4.2 Impact of the interface impedance between the testing equipment and the wind turbine

As mentioned earlier, the total inductance and resistance of the wind turbine output transformer, AC cable and coupling transformer of the VSC-test equipment is here represented by an equivalent series branch R_{eq} and L_{eq}. If a third power collector transformer is present in the AC circuit or if a relatively long cable used to interconnect the wind turbine with the testing device, the total impedance between these two objects can increase. For this reason, it is of interest to investigate the impact of the interface impedance between the wind turbine under test and the testing equipment in the location of the system poles. Observe that under the assumption that the test equipment is in proximity to the wind turbine (similar to the case when the impedance-based

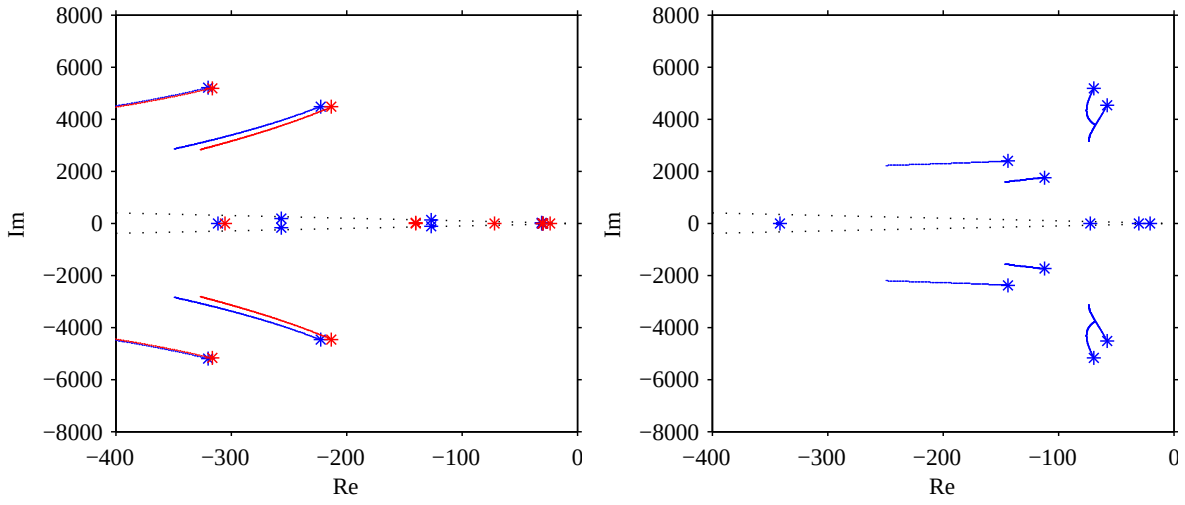

Fig. 5.7 Pole displacement when increasing the interface impedance R_{eq} and L_{eq} from 0.1 pu to 0.25 pu. Plot(a) pole location when using CL-controller with P (blue) and with PI (red); and Plot (b): pole location when using OL-control in collector-VSC.

test equipment is used for on-site test of wind turbines), the resonant frequency of the cables can be neglected. Thus, only the total impedance of the two transformers is considered in this analysis. In the following, the magnitude of R_{eq} and L_{eq} is varied for the case when the PCC voltage is controlled in close-loop (P-based and PI-based controller) and in open-loop. Here, the wind turbine is operated at full power.

Figure Fig. 5.7(a) shows the poles displacement of the system when varying the impedance from 0.1 pu to 0.25 pu. Observe that the selection of the close-loop controller (red traces for P-controller and blue traces for PI-controller) has a minor impact on the location of the poles. In this regard, the high-frequency poles are the most affected, becoming more damped as the impedance increases. Note in Fig. 5.7(b) that when open-loop controller at the collector-VSC is used, two high-frequency complex poles in proximity to the imaginary axis tend to approach the real axis, while the other two affected complex-poles become more damped. Finally, as shown in Fig. 5.7(a) and Fig. 5.7(a), the displacement of the low-frequency well damped poles is negligible.

In practice, increasing the impedance means to create more physical decoupling between the test equipment and the wind turbine system. Instead of using a direct coupling between the two devices, a reasonable impedance level brings the whole test system more stable. However, it is important to keep in mind that high impedance means high voltage drop between the two devices, affecting the resulting voltage at the terminals of the wind turbine when testing for LVRT.

5.5 Conclusion

In this chapter, the impact of control settings on the location of the system poles have been investigated through small-signal analysis. Here, it has been found that the selection of the topology of the voltage controller impacts the order of the system. In addition, the selection of the bandwidth of the controller determines the pole position, and thus, has a mayor impact on the stability of the system. When using a P-based controller in the PCC voltage control, the system poles become more damped, as compare with PI-based controller. However, the lack of integrator term does not necessarily benefits the performance of the system. In addition, the stability of the system is compromised if a strong filter is applied when feed-forwarding the grid current in the control-loop. In this regard, the PI-based controller is found to be more robust against different bandwidth of the LPF applied to the grid current. Moreover, a fast filtering of the grid current is always beneficial for the stability of the system.

The use of PI controller with active damping increases the order of the system. However, as also discussed in the previous chapter, the addition of the virtual resistor and integrator term gives a better dynamic performance, especially when removing steady-state error in a system with unknown losses. In this analysis it has been found that the size of the virtual resistor can be reduced while maintaining stability, compromising the ability of the controller in rejecting voltage disturbances.

External parameters such as controller bandwidth of the test object, or interface impedance between the tested object and the testing equipment will also impact the position of the poles.

However, if these parameters are kept within its nominal range, the stability of the system is maintained. Finally, time domain simulations must be carried out to guarantee the stability of the system in case of large disturbances. Thus, in the following section, a validation of the testing methodology is presented.

Chapter 6

Validation of the proposed grid code testing methodology

6.1 Introduction

In the previous chapters, the overall control strategy for the VSC-based testing equipment and for the wind turbine including LVRT control strategy have been discussed. Hence, a validation of the investigated grid code testing methodology is presented in this section. Starting from the evaluation of different ramp rates when varying the PCC voltage in open-loop, the evaluation of the close-loop controller will be carried out and the algorithm for emulating the short-circuit impedance of the grid by the test equipment will be derived. Moreover, part of the controllers will be validated through laboratory experiment. Finally, filed test results of a 4 MW wind turbine and a 8 MW testing equipment will be presented.

6.2 Simulation verification

This section is dedicated to the simulation of the test system shown in Fig. 4.2 interconnected to the wind turbine system given in Fig. 4.15. The data of the parameters of the test-bench is given in Table 4.1. First, an evaluation of different ramp rates when varying the PCC voltage with open loop control is given. Afterwards, different PCC voltage controllers including open-loop, close loop P-based and close loop PI-based will be compared in terms of effectiveness in following the reference voltage. In addition, an analysis on the simulation results of the complete test bench is given for a voltage dip test and LVRT test. Moreover, the algorithm for short circuit impedance emulation and the capability of the testing equipment in representing different grid scenarios is investigated. Additionally, phase-angle shift test and unbalanced voltage dip test performed on the wind turbine by the investigated VSC-based testing equipment are also presented. In the following, the electrical system has been modelled in the simulation platform PSCAD/EMTDC v4.2 [45].

6.2.1 Impact of different ramp-rates when using open-loop control of the PCC voltage

The use of open-loop control has been widely used when controlling the collector-side in HVDC collector systems. For this reason, the first approach in controlling the PCC voltage when performing the step is to manually control the modulation index of the collector-VSC. However, uncontrolled transients might occur if a step function is used when reducing the voltage. For

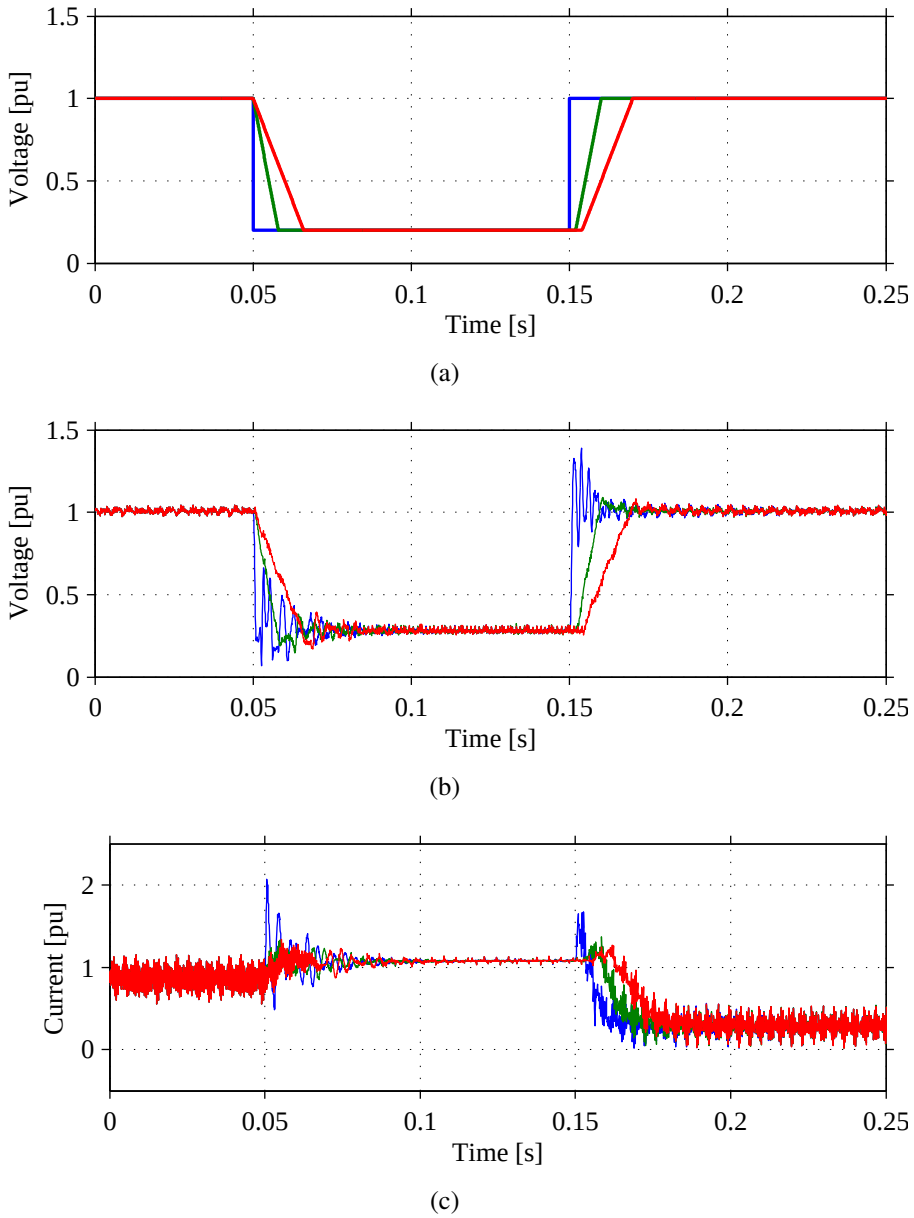

Fig. 6.1 Ramp-rate comparison when using open-loop control of PCC voltage: step function (blue), voltage dip with rate of 0.1 [pu/ms] (green), and voltage dip with 0.05 [pu/ms] (red). Plot (a): voltage reference $|\underline{u}^*|$; Plot (b): magnitude of PCC voltage $|\underline{e}|$; Plot (c): magnitude of converter current $|\underline{i}_t|$.

this reason, the effect of different ramp-rates applied to the voltage reference, including a step change when applying a voltage dip in the PCC, will be investigated.

Zero voltage ride through test by VSC has been successfully performed using open-loop control of the VSC in [37], [38] and [48] by setting the modulation index to zero. To cope with zero-voltage ride through, here the controller on the wind turbine needs to be further improved by limiting (to non-zero) the feed-forward of the grid voltage $\hat{\underline{e}}_{\mathrm{w}}^{(\mathrm{dq})}$ in the DC voltage controller, in the PLL and in the LVRT control among other modifications. On the other hand, the LVRT profile of the majority of the selected grid codes are defined within a minimum dip of 0.15 pu, as shown in Fig. 3.2. For these reasons, in order to demonstrate the performances of the different controllers when testing the modelled wind turbine, here the minimum dip has been set to 0.2 pu. In the following, the open-loop control given in Section 4.4.2 has been implemented in the collector-side VSC of the test equipment. The voltage is reduced from 1 pu to 0.2 pu and maintained for 100 ms.

As shown in Fig. 4.10(a) and also discussed in Section 5.3.1, when given a step change directly in the PWM of the VSC, the system presents an oscillatory response. When the wind turbine is connected (and thus, $\underline{i}_{\mathrm{g}} \neq 0$), the system becomes more damped due to the fact that the majority of the current comes from the wind turbine and not from the resonance introduced by the filters. Furthermore, in order to mitigate the transient behavior produced by the resonance, a predefined rate limiter on the VSC voltage can be implemented. For this reason, it is of interest to investigate the effect of different ramp-rates applied to the voltage reference $\underline{u}^*$ when testing for voltage dip using open-loop control of the VSC-based test equipment, which can result in a less oscillatory system response. In the simulated scenario, the wind turbine is operating at full power production. Furthermore, the LVRT control strategy described in Section 4.6.2 has been also implemented.

In Fig. 6.1(a) is shown the waveform of the voltage reference magnitude $|\underline{u}^*|$ for different rate of change of the reference converter voltage. Observe that blue traces correspond to a step variation, while green and red traces correspond to a ramp-rate of 0.1 [pu/ms] and 0.05 [pu/ms], respectively. The resulting PCC voltage magnitude $|\underline{e}|$ is shown in Fig. 6.1(b), and the magnitude converter terminal current $|\underline{i}_{\mathrm{t}}|$ is shown in Fig. 6.1(c).

As shown in Fig. 6.1(b), when using a step function in the reference converter voltage, the PCC voltage reaches a minimum peack of approximately 0.08 pu in the first transient, while in the second transient peaks at 1.4 pu. Observe that the frequency of the oscillations depicted in blue traces is 432 Hz, similar to the average resonant frequency of the high-frequency poles given in Fig. 5.3. Moreover, according to Table 5.1, the resonant frequency between C_{f} and L_{f} present in the reduced model shown in Fig. 5.1 is in proximity to 400 [Hz].

The current shows a similar transient response, reaching 2 pu when the voltage is reduced and 1.7 pu when the voltage is increased back to normal condition. This uncontrollable transient response can lead to tripping of both devices due to the action of a protection system. Moreover, over-voltages and over-current can damage the power electronic devices and reduce the lifetime of the capacitors and inductors present in the electrical circuit [29], [33]. For this reason, the use of step variation in the reference voltage is not recommended when performing LVRT test.

When using a ramp rate of 0.05 [pu/ms] (corresponding to the red traces in Fig. 6.1), the PCC voltage responds in a safer way and no over-currents nor over-voltages are induced. Although a

smooth response of the system can be obtain, the PCC voltage requires 25 ms to reach steady state during the voltage dip and during the recovery.

In [49] it is shown in detail the simulation and field test results of a LVRT test for certification process of a DFIG wind turbine using the impedance-based test equipment shown in Fig. 3.5. The resulting rate of change of the voltage at the terminals of the wind turbine is found to be is 0.05 [pu/ms]. Similarly, the rate of change at the LV side of the coupling transformer is 0.03 [pu/ms].

As compared with the case scenario given in [49], here the system benefits from a wider controllability of the system voltage when using VSC-based testing equipment. In order to have an acceptable transient dynamic behavior, the maximum ramp-rate is here selected to be 0.1 [pu/ms]. Observe that for the green traces in Fig. 6.1, the resulting voltage and current magnitudes are within the rated values.

6.2.2 Analysis on the impact of the topology of the PCC voltage control

As previously discussed, the use of open-loop control can produce undesired transients in the system, if the use of a suitable ramp-rate is not considered. In addition, if the current of the collector-VSC is not controlled in close-loop, these transients can be propagated into the DC-link producing undesired stress in the hardware. For these reasons, as proposed in Section 4.4.2, two type of close-loop PCC voltage controllers have been investigated in this thesis: a P-based controller and a PI-based controller.

Here, a comparison of the performance of the open-loop control (without compensation of the voltage drop across the interface inductor) and both close-loop controllers is given. The focus is on the dynamic of the waveform of the PCC voltage $\underline{e}$ and the converter current $\underline{i}_{\mathrm{t}}$. The voltage reference is a voltage dip with a retained voltage of 0.2 pu. The voltage reference is reduced with a ramp-rate of 0.1 [pu/ms] and maintained for 250 ms. The wind turbine is equipped with the LVRT control strategy described in Section 4.6.2 and it is operated at full power production and at unity power factor.

In Fig. 6.2 is shown the transient response of the PCC voltage. In particular, a zoom of the transient during the voltage dip and during the recovery are given in Fig. 6.2(a) and Fig. 6.2(b), respectively. In the figures it is possible to observe that the PCC voltage is controlled in proximity of 1 pu when open-loop control (red traces) as well as PI-based close-loop (blue traces) controllers are used. For P-based controller (green traces), the pre-fault voltage is 0.85 pu. As expected, the P-based controller cannot fix the steady state error present in the voltage.

At the moment of the dip, the LVRT response of the wind turbine creates a transient at 0.51 s when reducing its active power output and immediately injecting reactive current in order to support the voltage. When open-loop controller is used, the steady-state PCC voltage during the dip is boosted, reaching a maximum of 0.3 pu, mainly due to the action of the wind turbine. For the case when PI-controller is used, the PCC voltage is controlled exactly at 0.2 pu within 20 ms after the dip. Observe at the green traces that when the P-based controller is implemented, the steady-state voltage during the dip is in proximity to 0.2 pu only due to the reactive power support from the wind turbine.

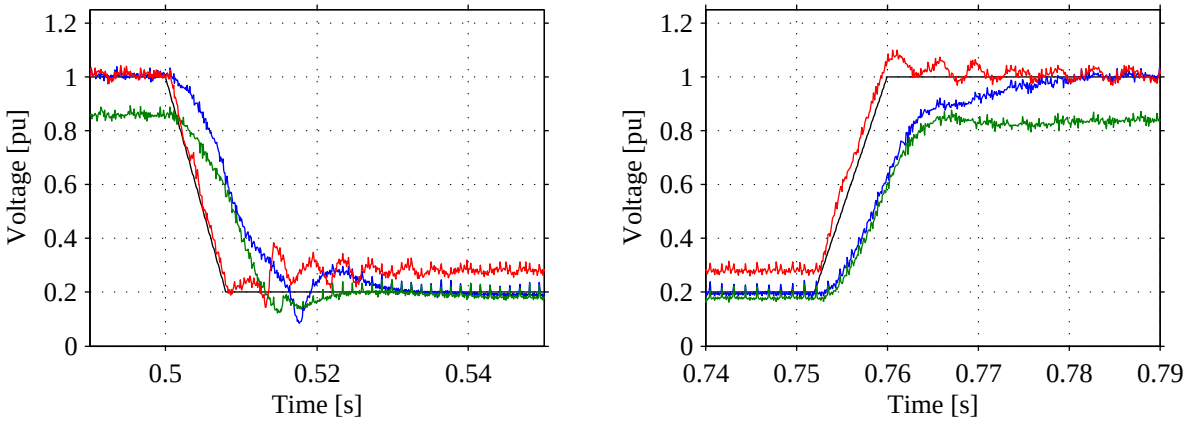

Fig. 6.2 Impact of the topology of the PCC voltage controller. In plots: voltage reference $\underline{e}^*$ (black), response of the PCC voltage $\underline{e}$ when it is controlled by a PI-based controller (blue), P-based controller (green), and open-loop control (red). Plot (a): transient during voltage drop; Plot (b) transients during voltage recovery.

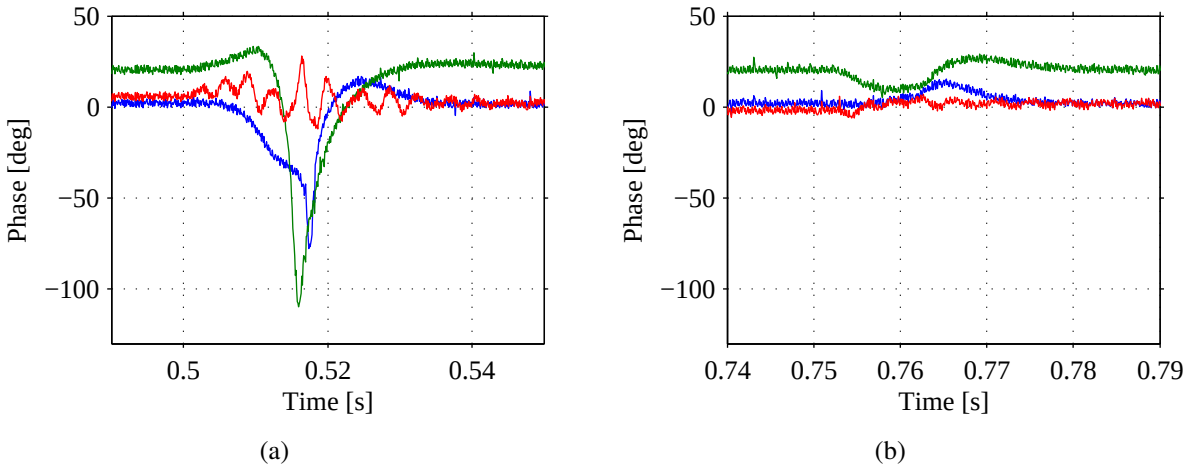

Fig. 6.3 Impact of the topology of the PCC voltage controller on the phase-angle of the voltage $\underline{e}$ when it is controlled by a PI-based controller (blue), P-based controller (green), and open-loop control (red). Plot (a): transient during voltage drop; Plot (b) transients during voltage recovery.

The transient response of the PCC voltage when recovering from the dip is shown in Fig. 6.2(b). When the voltage reference is back to 1 pu, the PCC voltage presents an oscillatory response when open-loop control is used. Moreover, when the PI-controller is used, the integrator takes approximately 30 ms to bring the voltage up to 1 pu. On the other hand, when a proportional controller is used, the post-fault PCC voltage reaches 0.85 pu.

The response of the phase-angle of the voltage $\underline{e}$ when using the three investigated controllers is shown in Fig. 6.3. Observe in Fig. 6.3(a) that when the voltage is reduced, the P-controller (green traces) and PI-controller (blue traces) actively vary the angle of the PCC voltage in order to remove the stored energy in the capacitor. During the initial transient of the dip, the angle

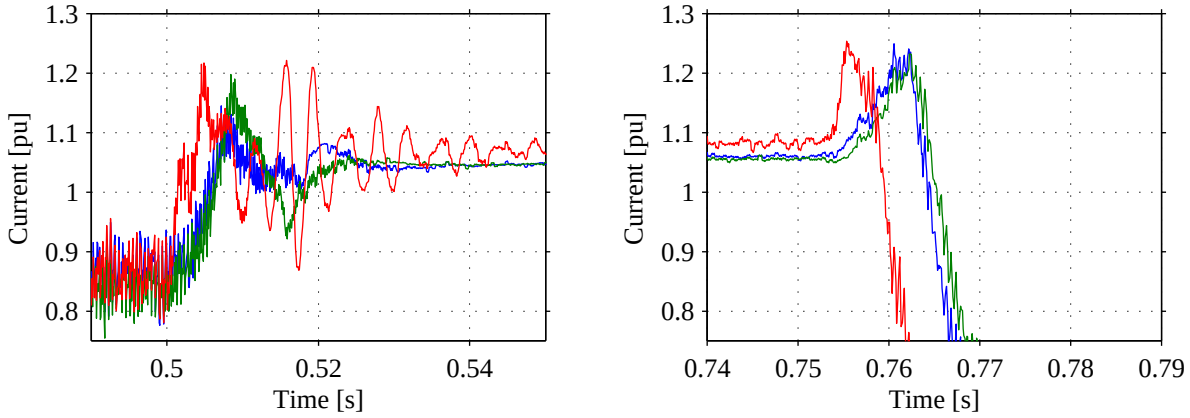

Fig. 6.4 Impact of the topology of the PCC voltage controller. In plots: response of the collector-VSC current $|\underline{i}_{\mathrm{t}}|$ when the PCC voltage is controlled by a PI-based controller (blue), P-based controller (green), and open-loop control (red). Plot (a): transient during voltage drop; Plot (b) transients during voltage recovery.

deviates from 0 degrees for 15 ms. Depending of the bandiwdth of voltage controller, the use of close-loop control introduces a delay when controlling the actual PCC voltage. Observe that since the P-controller lacks of an integrator and active damping term, the angle reaches a minimum of -110 degrees when reducing the voltage, as shown with green traces in Fig. 6.3(a). When using PI-based controller, the angle of the voltage reaches -90 degrees. This transient is also affected by the fact that the wind turbine is rapidly varying its active and reactive power output as soon as the voltage dip is detected at its terminals. Observe that when open-loop is implemented, the frequency of the angle variations during the voltage dip is 350 Hz, similar to the undapmed poles found in Fig. 5.3.

Moreover, the PLL included in the wind turbine control has a bandwidth α_{PLL} equal to 30 [rad/s]. For this reason, the resulting transient in the angle of the wind turbine voltage $\underline{e}_{\mathrm{w}}$ (tracked by the PLL) is fast, allowing the wind turbine to remains synchronized. Observe that once the voltage reaches steady-state at t = 0.53 s, the voltage angle is controlled at 0 degrees. Finally, the red traces correspond to the waveform of the phase-angle when the voltage is controlled in open-loop. The phase of the PCC voltage is maintained in proximity to 0 degrees only as a result of the power flow across the AC-link. Observe, however, that an oscillatory response of the voltage leads to an oscillatory response of the angle.

The waveform of the phase-angle at recovery of the voltage is shown in Fig. 6.3(b). Here, only the OL-controller (red traces) and PI-controller (blue traces) manage to maintain the angle of the voltage in proximity to 0 degrees. Here, the LVRT control strategy of the wind turbine maintains the active power production at 0 pu, while the reactive power is set according to the retained voltage at its terminals. Moreover, during the recovery of the voltage, the wind turbine is slowly decreasing its reactive power output. In these conditions, the PI-controller shows a better dynamic performance in controlling the angle of the voltage at 0 pu.

The response of the current $\underline{i}_{\mathrm{t}}$ is shown in Fig. 6.4. The pre-fault current is controlled in 0.9

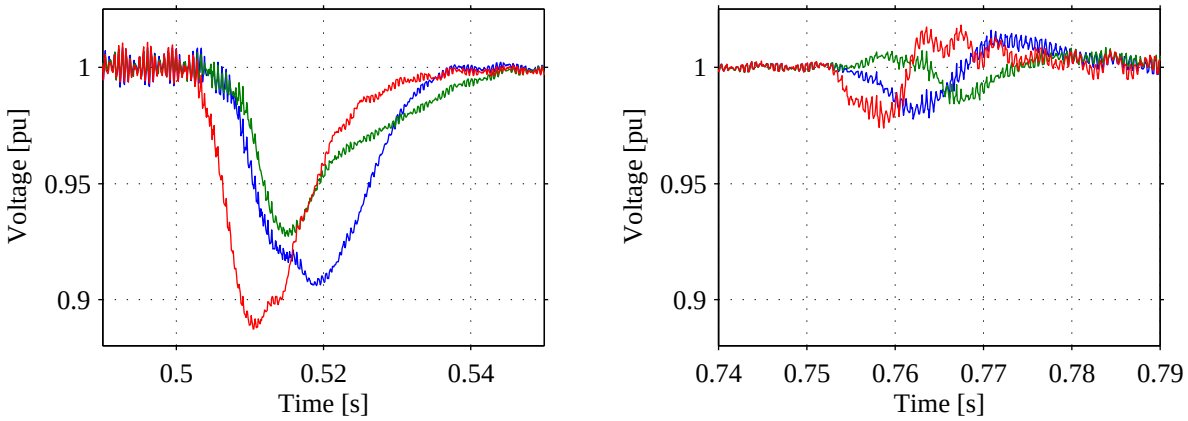

Fig. 6.5 Impact of the topology of the PCC voltage controller. In plots: response of the DC voltage u_{DC} when the PCC voltage is controlled by a PI-based controller (blue), P-based controller (green), and open-loop control (red). Plot (a): transient during voltage drop; Plot (b) transients during voltage recovery.

pu (in the wind turbine base power of 4 MW) by the wind turbine current controller. When the voltage dip occurs at 0.5 s, before the LVRT control strategy comes into place, the DC voltage controller will immediately maximize the current output in order to deliver the produced power. After 10 ms approximately, the LVRT control reacts by injecting reactive current into the system at 0.52 s. In addition, the fast variation of the voltage at the filter capacitor also contributes to the transient seen in the current, especially in the case of open-loop control. In this case, the current reaches a maximum value of 1.21 pu, as shown in Fig. 6.4(a). The current transient is reduced to 1.19 pu when a P-based PCC voltage controller is used. When the PI-controller is implemented, the current reaches a peak value of 1.13 pu. Observe that during the voltage dip, the current is maintained in proximity to 1 pu by the current control in the wind turbine.

For the recovery of the voltage shown in Fig. 6.4(b), the resulting current waveform when three different controllers are used are similar. Here, the wind turbine is not producing active power and it is reducing the reactive current as the retained voltage increases. Observe during the recovery that the selection of the PCC voltage controller has no mayor impact in the current $|\underline{i}_{\mathrm{t}}|$ when recovering from the voltage dip. The maximum peak during the recovery is 1.25 pu for all three voltage topologies.

It is of interest to observe the response of the DC voltage u_{dc} of the test equipment when varying the topology of the PCC voltage controller in the collector-side VSC. As discussed in the previous section, the use of open-loop control of the VSC voltage may create transients at the DC-link of the test equipment. The waveform of the DC-link voltage is shown in Fig. 6.5. When applying a voltage dip, the active power transferred from the wind turbine to the test equipment is drastically reduced. With reference to (4.54), during the first 20 ms of the voltage dip, the input power P_{COL} is lower than the output power P_{GRID}. This unbalanced in DC power will drop the actual DC-link voltage, as shown in Fig. 6.5(a). As expected, the minimum voltage in the DC-link is achieved when the PCC voltage is controlled in open-loop, while the minimum voltage drop occurs when

the proportional controller is used. Similar behavior can be seen in Fig. 6.5(b) when the voltage is recovering. Observe that, according to Section 4.6.2, the wind turbine is not producing power at 0.76 s. Hence, the transients shown in Fig. 6.5(b) are due to the interaction between the DC capacitor of the test equipment and the energy delivered into the AC-link when increasing rapidly the collector voltage.

Finally, as discussed in the previous section, in order to avoid an oscillatory response in both current and voltage at the PCC, an acceptable rate of change of 0.1 [pu/ms] in the voltage reference is found to be sufficient to perform LVRT test. For this analysis, the rate-limiter has also been kept when using P-controller and PI-controller. Moreover, if close-loop control is implemented in the collector-side of the test equipment, the transients in the voltage and current at the PCC are damped. From the previous simulation results it is found that the response of the PCC voltage is acceptable if the PI-based controller with active damping is implemented. In addition, the use of ramp-rate limiter in the reference voltage is helpful, especially if the test object reacts by rapidly varying its output current when detecting a voltage dip. For these reason, in the following simulation results, the PI-based PCC voltage controller has been selected for further investigation.

6.2.3 Voltage dip test

In this section, the case where PI-based controller is used for voltage dip is analysed in detail. Here, the focus will be on the controllability of the dq quantities of the PCC voltage, the response of the wind turbine system when detecting a voltage dip, and on the impact of the test on the DC-link voltage of the test equipment and on the AC grid. Here, the PI-based close-loop controller given in (4.39) has been implemented in the testing equipment. The voltage is controlled to 1 pu followed by a reduction with a rate of 0.1 [pu/ms]. A retained voltage of 0.2 pu is maintained for 250 ms. In the following, the electrical quantities of both the testing equipment and the wind turbine are analysed in detail.

The three-phase terminal voltage of the wind turbine filter $\underline{u}_{\mathrm{w}}$ is shown in Fig. 6.6(a). During the voltage dip, the wind turbine output current $\underline{i}_{\mathrm{t,w}}$ depicted in Fig. 6.6(b) is maintained in 1 pu. Observe in Fig. 6.6(c) that the active power output is reduced to 0 pu in order to give room to the reactive power to be injected in the grid. The excess of produced power boosts the DC-link voltage immediately after the dip, as shown in Fig. 6.7(a). However, the DC crowbar reacts by redirecting the power into the braking resistor. By this means, the DC-link voltage is maintained at a safe value.

Moreover, as depicted in Fig. 6.7(b), a maximum of 1 pu of reactive current is injected during the voltage dip, boosting the AC voltage $\underline{u}_{\mathrm{w}}$ at the terminals of the turbine up to 0.28 pu. Hence, the maximum reactive power during the fault is 0.28 pu. At the moment that the voltage is recovering from the fault, the LVRT control strategy in the wind turbine maintains the reactive current, giving a fast rising of the reactive power at 0.36 s. The reactive current is reduce once the voltage has reached 1 pu at 0.375 s. Furthermore, the AC voltage is monitored for additional 500 ms, as enforced by the German and Danish grid codes. The wind turbine resumes active power production 100 ms after the recovery of the voltage.

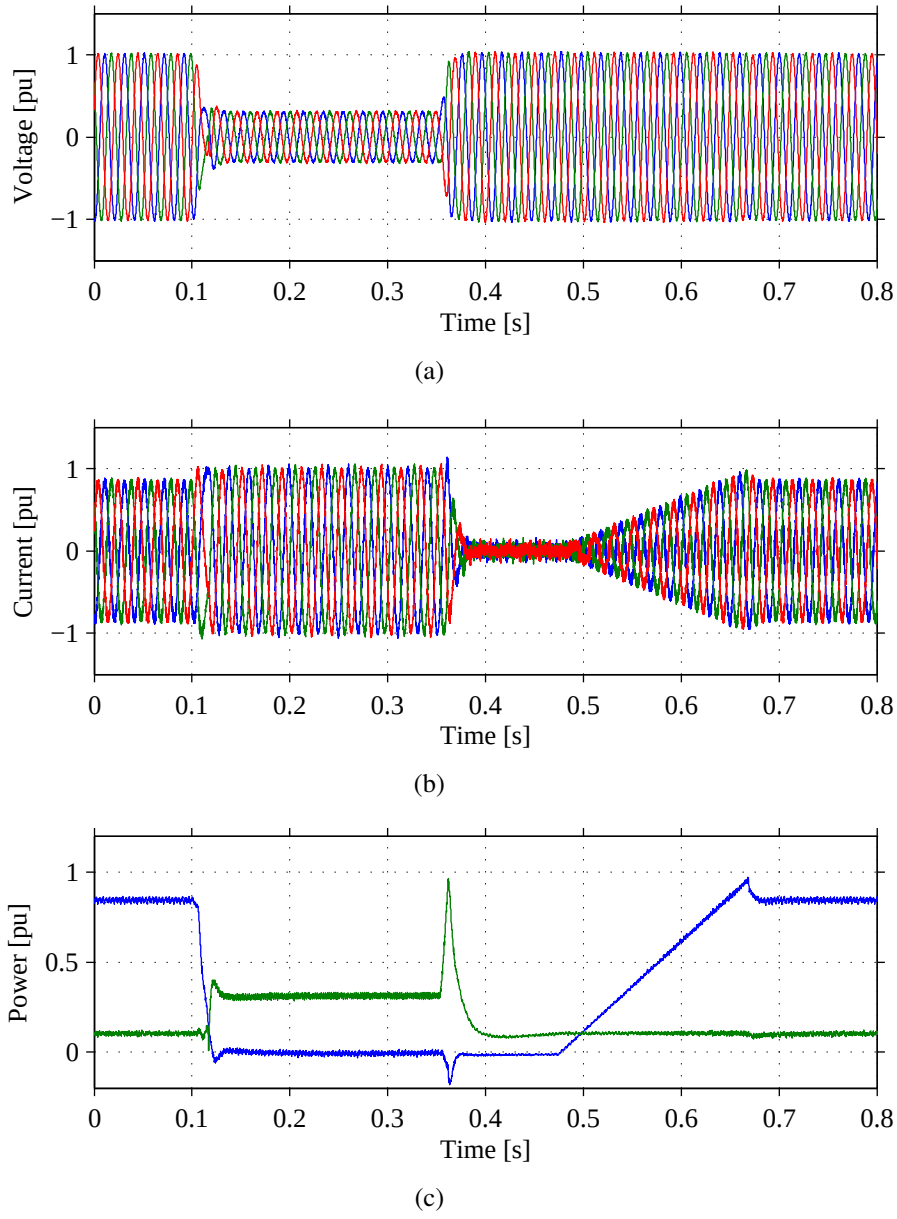

Fig. 6.6 Wind turbine response under a voltage dip. Plot (a): three-phase voltage $\underline{e}_{\mathrm{w}}$; Plot (b): three-phase current $\underline{i}_{\mathrm{t,w}}$; Plot (c): active (blue) and reactive (green) power output.

Moving the focus on the testing equipment, the reference and actual PCC voltage are shown in Fig. 6.8(a). The transient in the actual PCC voltage and wind turbine filter voltage is due to the sudden exchnage between active and reactive power; however, the test equipment manage control the voltage back to its reference value of 0.2 pu. Moreover, the recovery of the voltage is controlled in a smooth way. The reference and estimated d and q voltage components are depicted in Fig. 6.8(b) and Fig. 6.8(c), respectively. Note that the controller in the collector-side VSC of the test equipment lacks of a PLL, meaning that it generates its own reference frequency ω_{s}^{*} and thus its self generated dq transformation angle θ. As shown in the plots, each voltage component is tracked and controlled at their reference values. Observe in Fig. 6.8 at 0.5 s that

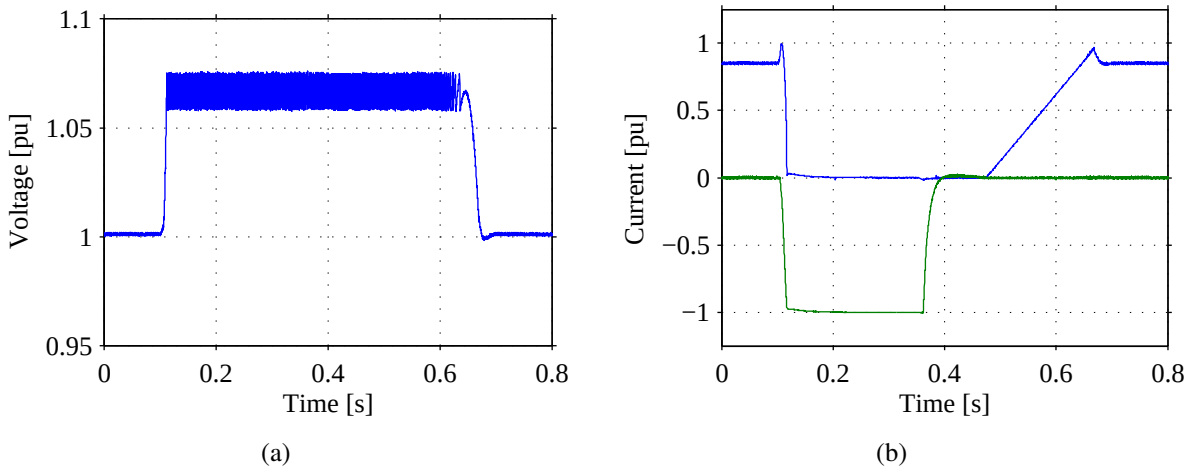

Fig. 6.7 Wind turbine LVRT control under a voltage dip. Plot (a): DC voltage $\underline{u}_{\mathrm{dc,w}}$; Plot (b): active current $\hat{i}_{\mathrm{t,w_d}}$ (blue) and reactive current $\hat{i}_{\mathrm{t,w_q}}$ (green).

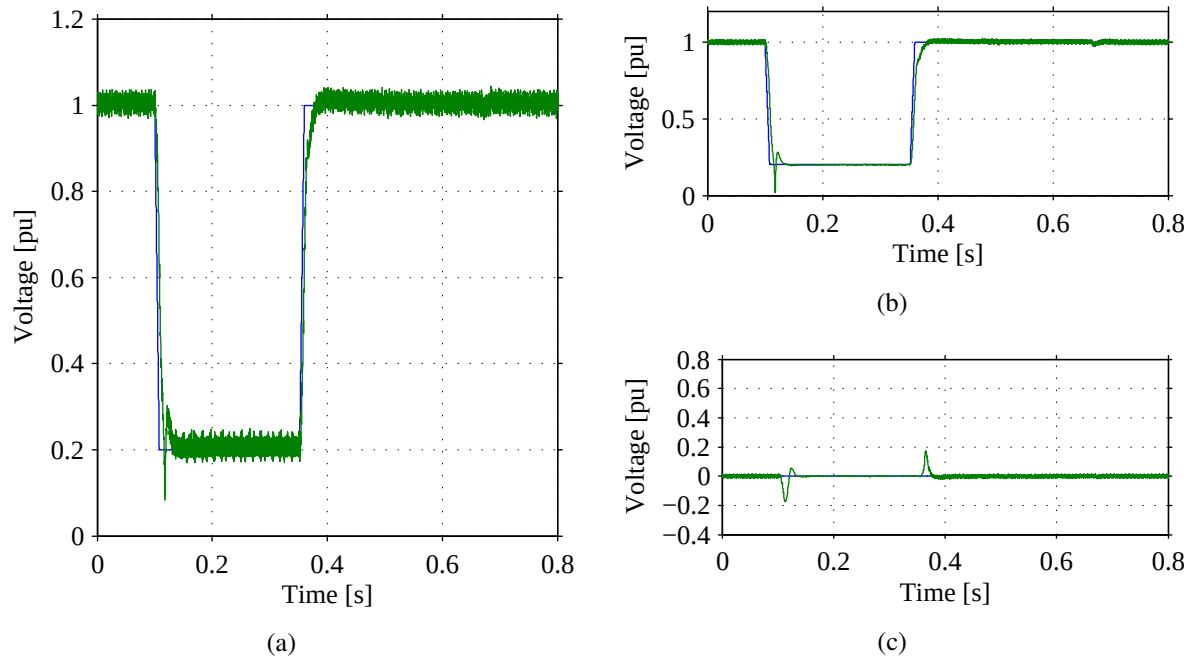

Fig. 6.8 PCC voltage control. Plot (a): reference voltage $|\underline{e}^*|$ (blue) actual magnitude of the PCC voltage $|\underline{e}|$ (green); Plot (b): d-axis PCC reference voltage e_{d}^* (blue) and estimated voltage $\hat{e}_{\mathrm{d}}$ (green); Plot (c) q-axis PCC reference voltage e_{q}^* (blue) and estimated voltage $\hat{e}_{\mathrm{q}}$ (green).

when wind turbine is varying its current output, a transient is seen in both components of the voltage. During this short moment, the phase-angle of the PCC voltage reaches 90 degrees of phase-shift, as shown in Fig. 6.3(a).

The reference and estimated d-axis and q-axis components of the current vector $\underline{i}_{\mathrm{t}}^{(\mathrm{dq})}$ are depicted in Fig. 6.9(b) and Fig. 6.9(c), respectively. The actual tree-phase VSC curret $\underline{i}_{\mathrm{t}}$ is shown in Fig. 6.9(a). During normal operation, the effect of the switching of the VSC and the reactive

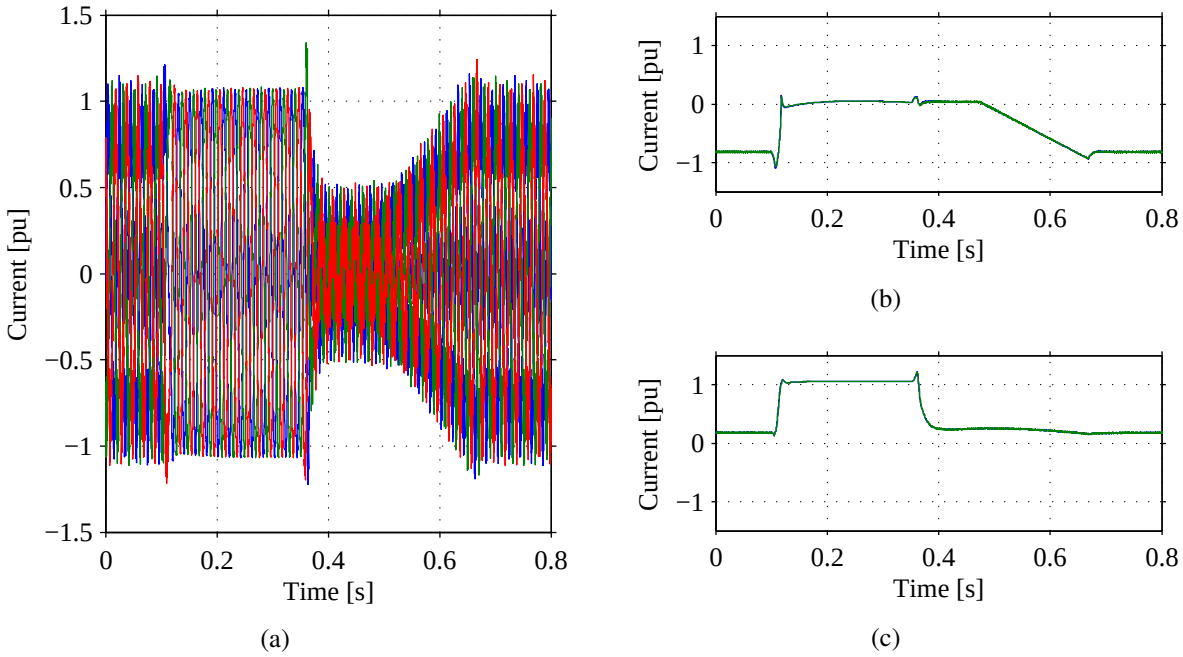

Fig. 6.9 Current control in test equipment. Plot (a): actual three-phase current $\underline{i}_{\mathrm{t}}$; Plot (b): d-axis current reference $i^*_{\mathrm{t_d}}$ (blue) and estimated current component $\hat{i}_{\mathrm{t_d}}$ (green); Plot (c): q-axis current reference $i^*_{\mathrm{t_q}}$ (blue) and estimated current component $\hat{i}_{\mathrm{t_q}}$ (green).

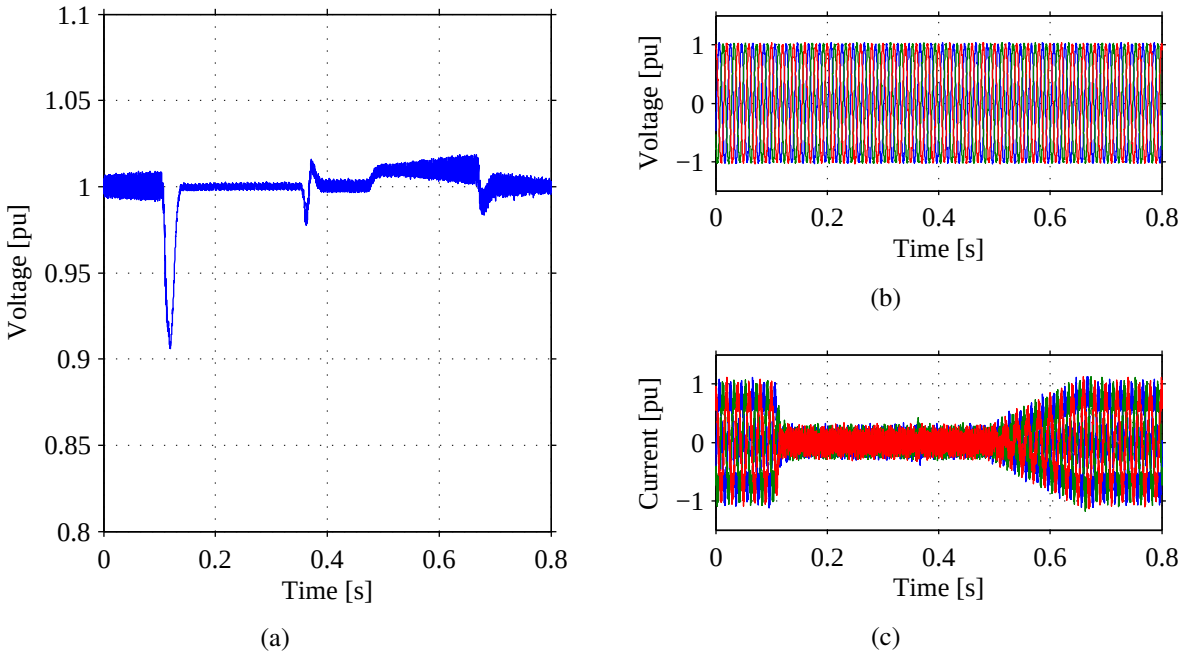

Fig. 6.10 Grid-side VSC in test equipment. Plot (a): DC link voltage U_{dc}; Plot (b): actual three-phase grid filter voltage $\underline{e}_{\mathrm{g}}$; Plot (c): actual three-phase grid-VSC terminal current $\underline{i}_{\mathrm{t,g}}$.

current introduced by the capacitor filter banks both in the wind turbine and test equipment increases the actual peak value of the three-phase current slightly above 1 pu (see Table 4.2 for

wind turbine base values). The current at the test equipment reaches a peak value of 1.25 pu in the first transient and 1.4 pu at the recovery of the voltage. This current peak is the result of the response of the response of the current control on the wind turbine when a fast voltage variations occurs at its terminals. However, the rating of the test equipment, given in Table 4.1, doubles the rating of the wind turbine. For this reason, a 1.4 pu transient current is not harmful for the test equipment. Observe that if the wind turbine is 60% larger (7 MW), this current would be in proximity to the rating of the testing equipment. In this case, special consideration bust be taken on the selection of a minimum dip and on the selection of a suitable ramp-rate in order to limit the transient current.

Finally, it is of interest to analyse the response of the grid-VSC of the test equipment. Here, the focus is on the DC voltage control, and the impact of the testing towards the AC grid. In Fig. 6.10(a) is shown the DC-link voltage u_{dc} and the three-phase filter voltage $\underline{e}_{\mathrm{g}}$. From the figure, it is possible to observe that the DC link voltage drops at 0.1 s approximately. This is due to the slow time constant of the DC-link controller of the grid VSC in changing the output power reference, when a fast reduction of active power from the wind turbine is applied.

Moreover, from Fig. 6.10(b) is shown the voltage at the grid connection point of the testing equipment. As seen from the figure, the voltage is unaffected by the performance of the test. Although the current is varied according to the active power variation of the wind turbine, as shown in Fig. 6.10(c), the current does not present any transients, and is controlled by the VSC during the complete event.

In this example, the PCC voltage is controlled in a stiff manner, meaning that the reactive power injected by the wind turbine does not affect the setpoint of the PCC voltage. Hence, an interesting alternative could be to include the dynamics of a virtual impedance when testing for LVRT, thus having the ability to emulate the short-circuit impedance of a grid. This concept will be explored in the following section and demonstrated with simulation results.

6.2.4 Short circuit impedance emulation

A control feature to emulate the impact of the grid short-circuit power during LVRT operations has been implemented. Under the assumption that the test equipment is operated within its voltage limits, both active and reactive power production of the test object will impact the set point of the system voltage $\underline{e}$, if the impedance emulation algorithm is enabled.

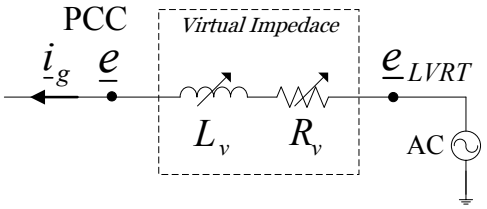

Fig. 6.11 Equivalent representation of the VSC-based test equipment for grid impedance emulation.

In Fig. 6.11 it is shown an equivalent representation of the test equipment used to emulate the

short-circuit power of the grid at the connection point, where the dynamic of the current $\underline{i}_{\mathrm{g}}$ in the dq frame is described by the expression:

$$\underline{e}_{\mathrm{LVRT}}^{(\mathrm{dq})} - \underline{e}^{(\mathrm{dq})} = L_{\mathrm{v}} \frac{d\underline{i}_{\mathrm{g}}^{(\mathrm{dq})}}{dt} + \underline{i}_{\mathrm{g}}^{(\mathrm{dq})}(R_{\mathrm{v}} + j\omega_{\mathrm{s}} L_{\mathrm{v}}) \tag{6.1}$$

labelling R_{v} and L_{v} as the inductance and resistance part, respectively, of the virtual grid impedance shown in Fig. 6.11, the voltage $\underline{e}_{\mathrm{LVRT}}^{(\mathrm{dq})}$ is the selected LVRT profile of a stiff voltage regulation and $\underline{e}^{(\mathrm{dq})}$ is the PCC voltage evaluated after the voltage drop over the virtual impedance.

The inductor L_{v} in Fig. 6.11 contributes as a smoothing factor on the dynamic of the current $\underline{i}_{\mathrm{g}}$. Observe that L_{v} also impacts the amount of voltage drop across the virtual impedance in (6.1), especially if the derivative term is included when calculating the reference voltage $\underline{e}^{*}$ for the PCC voltage controller. In addition, when implementing (6.1) in a digital controller, the discrete calculation of the derivative term when sampling the current $\hat{\underline{i}}_{\mathrm{g}}$ can be very sensitive to noise, especially if the sampling time is relatively small [50], [39].

In order to investigate impact of the derivative term on the dynamics of the voltage $\underline{e}^{(\mathrm{dq})}$ in (6.1), the system shown in Fig. 6.11 has been simulated. In this study, the reference voltage vector $\underline{e}^{(\mathrm{dq})^*}$ of the test equipment here represented as the three-phase voltage source labelled as "AC". The voltage is here varied in order to represent a stiff grid voltage or a grid with a predefined grid impendace. In addition, an RL load has been connected at the other end of the circuit in order to set the current denoted as $\underline{i}_{\mathrm{g}}$ at nominal value. Here, three different case scenarios has been simulated:

First, an actual impendace R_{actual} and L_{actual} of 0.15 pu has been interconnected between the RL load and the AC voltage source. A LVRT test has been performed to the load: the voltage $\underline{e}^{(\mathrm{dq})^*}$ = $\underline{e}_{\mathrm{LVRT}}^{(\mathrm{dq})}$ at the AC source is varied from 1 pu to 0.5 pu for 300 ms. The phase A of the resulting three-phase load voltage $\underline{e}$, which includes the dynamics produced by the actual impedance, is plotted in blue traces in Fig. 6.12.

Second, the actual impedance is removed and a virtual impendace R_{v} and L_{v} of 0.15 pu is set when calculating the voltage $\underline{e}^{(\mathrm{dq})*}$ according to the following expression:

$$\underline{e}^{(\mathrm{dq})^*} = \underline{e}_{\mathrm{LVRT}}^{(\mathrm{dq})} - \frac{d\underline{i}_{\mathrm{g}}^{(\mathrm{dq})}}{dt} L_{\mathrm{v}} + \underline{i}_{\mathrm{g}}^{(\mathrm{dq})}(R_{\mathrm{v}} + j\omega_{\mathrm{s}} L_{\mathrm{v}}) \tag{6.2}$$

Note that (6.2) is (6.1) rearranged in order to obtain the reference voltage $\underline{e}^{(\mathrm{dq})^*}$ and that the $\underline{e}^{(\mathrm{dq})^*}$ of the AC source includes the complete dynamic of voltage drop across the virtual impedance. Here, the same LVRT voltage profile has been applied to the load. The resulting load voltage $\underline{e}$ is plotted in red traces in Fig. 6.12.

Third and final case scenario. Here the dynamic of the voltage drop across the virtual impendace is removed from the reference voltage $\underline{e}^{(\mathrm{dq})^*}$, thus, only the static voltage drop is emulated as

$$\underline{e}^{(\mathrm{dq})^*} = \underline{e}_{\mathrm{LVRT}}^{(\mathrm{dq})} - \underline{i}_{\mathrm{g}}^{(\mathrm{dq})}(R_{\mathrm{v}} + j\omega_{\mathrm{s}} L_{\mathrm{v}}) \tag{6.3}$$

The waveform of the load voltage $\underline{e}$ is shown in green traces in Fig. 6.12.

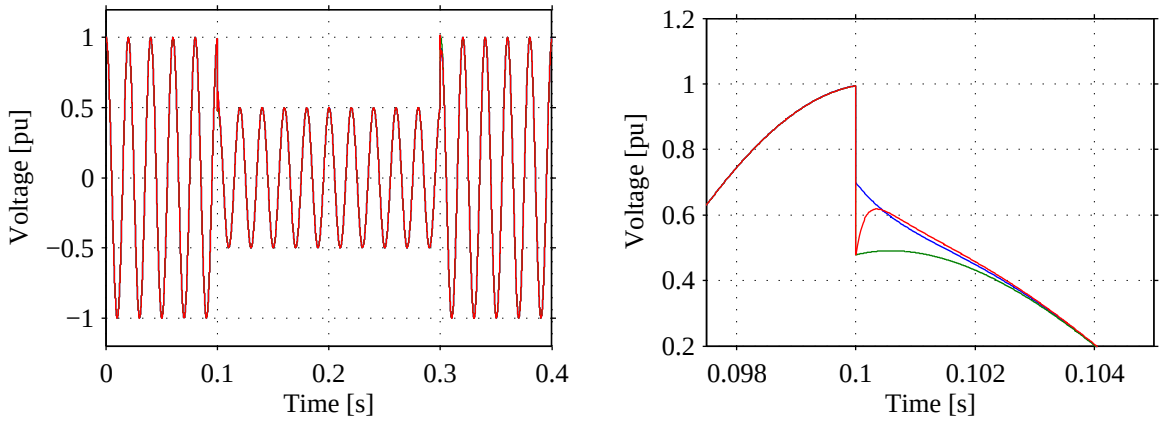

Fig. 6.12 Response of the load voltage $\underline{e}$ when a voltage dip is applied. In plots: load voltage when interconecting an actual grid impendace (blue) and when using dynamic voltage drop (red) and when using static voltage drop (blue) of an equivalent virtual impendace. Plot (a): Resulting voltage waveform of phase A during the complete event; Plot (b): Zoom of phase A during the voltage dip.

Observe Fig. 6.12(a) that for steady-state condition, when using virtual impedance emulation (with and without dynamic term) there is no difference with respect to the voltage waveform resulting when connecting the load through an actual grid impedance. During the transient, however, a mismatch between the emulated and actual grid voltages is clearly seen, as shown in Fig. 6.12(b). Note that when the derivative term of the voltage drop in L_v is included in (6.2) (red traces), the effect of the short-circuit impedance is emulated accurately within less than 0.5 ms. On the other hand, when the derivative term is not included (green traces), thus, using static voltage drop as in (6.3), the emulated voltage drop takes 2 ms to recreate the effects of an actual impedance.

Finally, it is important to observe that the dynamics of the emulated voltage drop in the virtual impedance is here constrained by the bandwidth of the voltage controller i.e.: in Fig. 6.8(a) the voltage takes 12 ms approximately to reach steady-state during the dip. Therefore, when calculating the reference PCC voltage, the derivative term (6.1) is chosen to be neglected. To emulate the effect of the grid impedance only by using steady-state voltage drop, the calculated voltage reference in Laplace form can be formulated as:

$$\underline{e}^{(\mathrm{dq})*} = \underline{e}^{(\mathrm{dq})}_{\mathrm{LVRT}} - \left(\frac{\alpha_{\mathrm{fil}}}{s+\alpha_{\mathrm{fil}}}\right)\hat{\underline{i}}^{(\mathrm{dq})}_{\mathrm{g}}(R_\mathrm{v} + j\omega_\mathrm{s}L_\mathrm{v}) \tag{6.4}$$

with α_{fil} = 2500 [rad/s] as the bandwidth of the LPF used to remove high-frequency content in the estimated grid current. Finally, the discrete implementation of the short-circuit impedance emulation algorithm is written as

$$\underline{e}^{(\mathrm{dq})*}(k) = \underline{e}^{(\mathrm{dq})}_{\mathrm{LVRT}}(k) - \hat{\underline{i}}^{(\mathrm{dq})}_{\mathrm{g,fil}}(k)(R_\mathrm{v} + j\omega_\mathrm{s}L_\mathrm{v}) \tag{6.5}$$

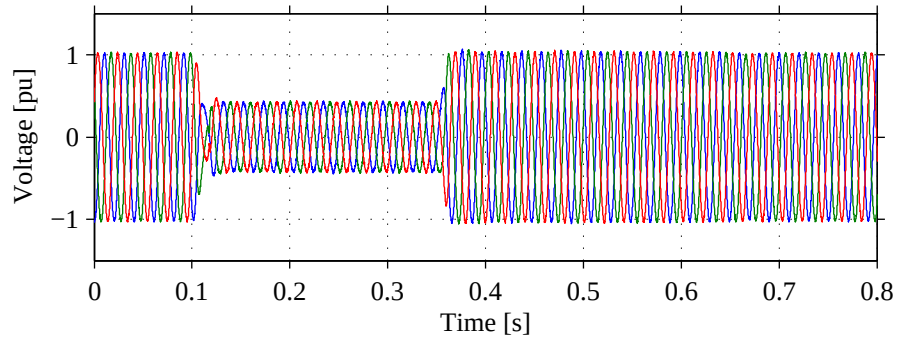

(a)

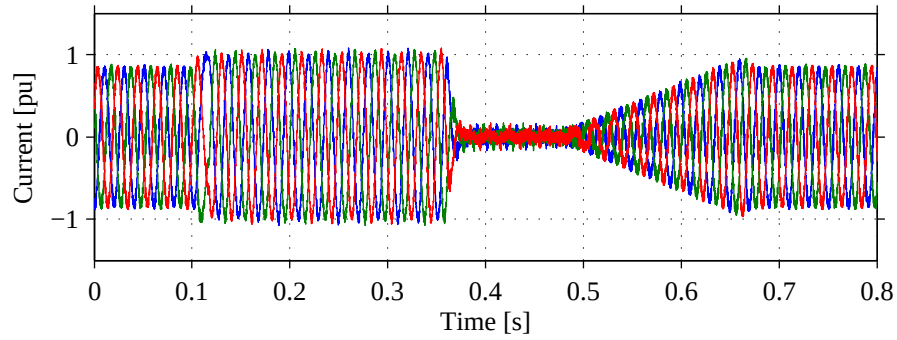

(b)

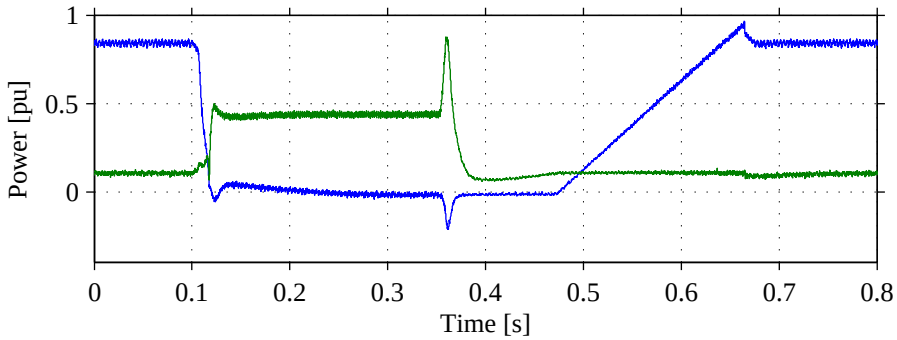

(c)

Fig. 6.13 Wind turbine response under a voltage dip with emulated short circuit power of 10 pu. Plot (a): three-phase voltage $\underline{e}_{\mathrm{w}}$; Plot (b): three-phase current $\underline{i}_{\mathrm{t,w}}$; Plot (c): active (blue) and reactive (green) power output.

with $\hat{\underline{i}}_{\mathrm{g,fil}}$ calculated in (4.31).

In the following, a virtual impedance of 0.1 pu corresponding a short circuit power of 10 pu (45 MVA) is simulated. Here, the focus will be on the dependency of the controlled PCC voltage (using PI-based close-loop controller) with respect of the reactive power exchanged between the wind turbine and the test equipment.

The pre-fault voltage is 1 pu, and the retained voltage reference is 0.2 pu for 250 ms. The resulting three-phase wind turbine voltage and output current is shown in Fig. 6.13(a) and Fig. 6.13(b),

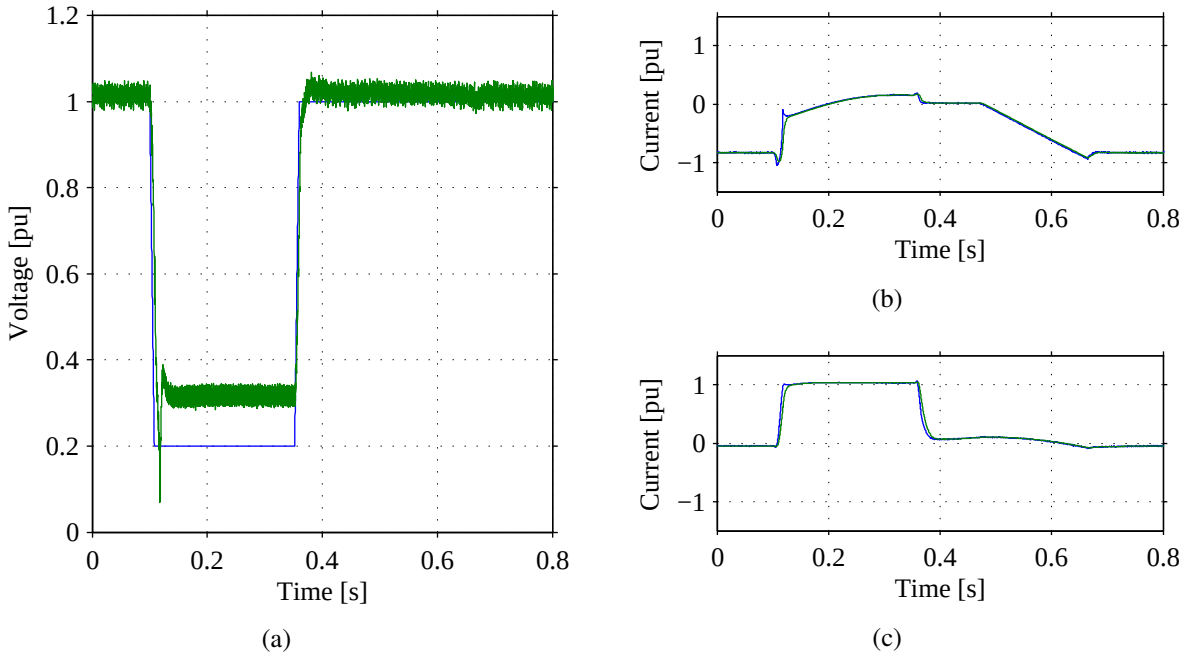

Fig. 6.14 PCC voltage control with emulated short circuit power of 10 pu. Plot (a): LVRT reference $|\underline{e}_{\mathrm{LVRT}}|$ (blue) actual magnitude of the PCC voltage $|\underline{e}|$ (green); Plot (b): estimated d-axis grid current $\hat{i}_{\mathrm{g_d}}$ (blue) and filtered current $\hat{i}_{\mathrm{g_{d,fil}}}$ (green); Plot (c): estimated q-axis current $\hat{i}_{\mathrm{g_q}}$ (blue) and filtered current $\hat{i}_{\mathrm{g_{q,fil}}}$ (green).

respectively. When the short-circuit impedance emulation is enabled, the active and reactive power output from the wind turbine shown in Fig. 6.13(c) affect the set point of the voltage reference in the test equipment, according to the discrete voltage reference calculation given in (6.5). In Fig. 6.13(a) it is possible to see that the $\underline{e}_{\mathrm{w}}$ reaches a peak of 0.45 pu during the dip, as compared with 0.28 pu in Fig. 6.6(a) when a stiff regulation of the PCC is applied. Similarly to the previous case , the wind turbine is injecting 1 pu of reactive current during the dip, thus, the maximum injected reactive power is 0.45 pu, as depicted in Fig. 6.13(c).

The resulting PCC voltage is boosted up to 0.33 pu during the dip, as shown in Fig. 6.14(a), due to the action of the wind turbine. Observe that there is a difference of 0.13 pu between the actual PCC voltage and the LVRT profile. This is due to the effect of the static voltage drop across the virtual impedance $R_{\mathrm{v}} + j\omega_{\mathrm{s}}L_{\mathrm{v}}$ when calculating reference signal $\underline{e}^{(\mathrm{dq})^*}$ for the voltage controller, according to (6.5). The d and q component of the current $\hat{\underline{i}}_{\mathrm{g}}$ are plotted in Fig. 6.14(b) and Fig. 6.14(c), respectively. Observe that for both plots, the non-filtered and filtered currents components are shown in blue and green traces, respectively. According to (6.5), the filtered current $\hat{\underline{i}}^{(\mathrm{dq})}_{\mathrm{g,fil}}$ is used to modify the voltage reference $\underline{e}^{(\mathrm{dq})^*}$. Moreover, the pre-fault and post-fault PCC voltage is also increased due to the reactive power injected by the wind turbine and test equipment filter banks.

In the following, the interest is on the wind turbine response when the recovery ramp given in grid code is included in the voltage reference of the test equipment.

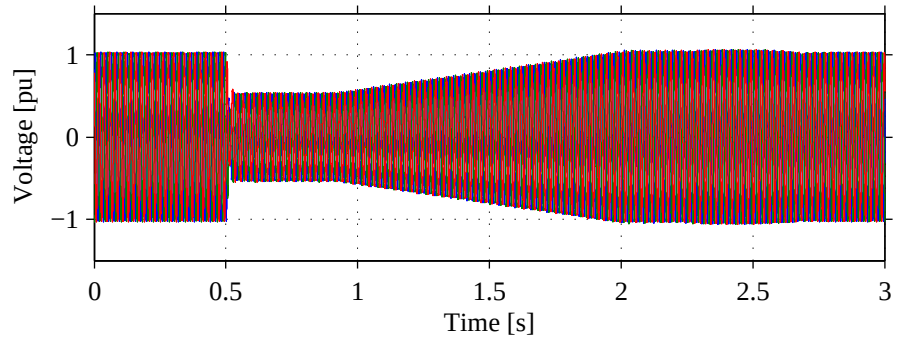

(a)

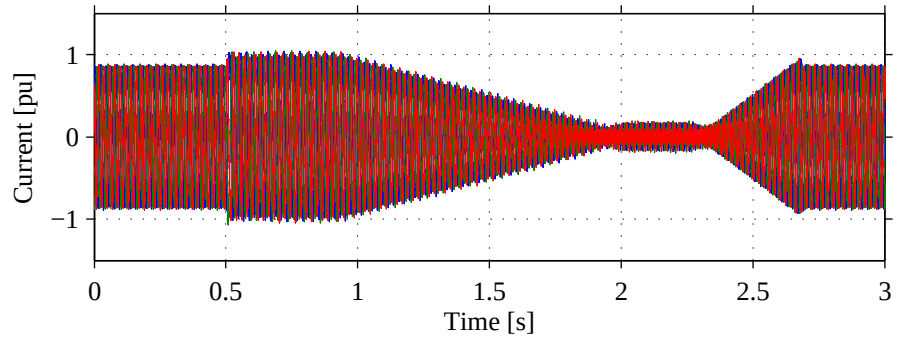

(b)

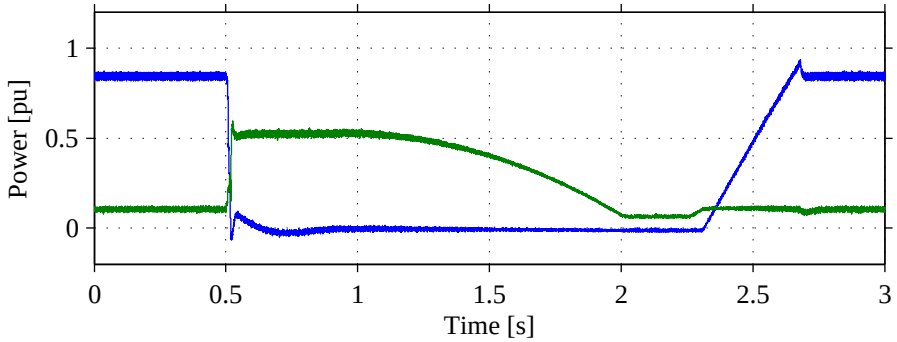

(c)

Fig. 6.15 Wind turbine response under a voltage dip. Plot (a): three-phase voltage $\underline{e}_{\mathrm{w}}$; Plot (b): three-phase current $\underline{i}_{\mathrm{t,w}}$; Plot (c): active (blue) and reactive (green) power output.

6.2.5 Test on wind turbine using the complete LVRT profile

Here, the wind turbine operates at full power and at unity power factor. The virtual short-circuit impedance is set to 0.2 pu, corresponding a short-circuit power of 5 pu (20 MW) at the PCC. The selected grid code LVRT profile is given in the German off-shore grid code [18]. The LVRT profile corresponds to a retained voltage of 0.2 pu for 400 ms, and a recovering ramp to 1 pu in the next 1 s.

The resulting three-phase wind turbine voltage is shown in Fig. 6.15(a). From the figure, it is possible to observe that the magnitude of the wind turbine voltage reaches 0.5 pu during the

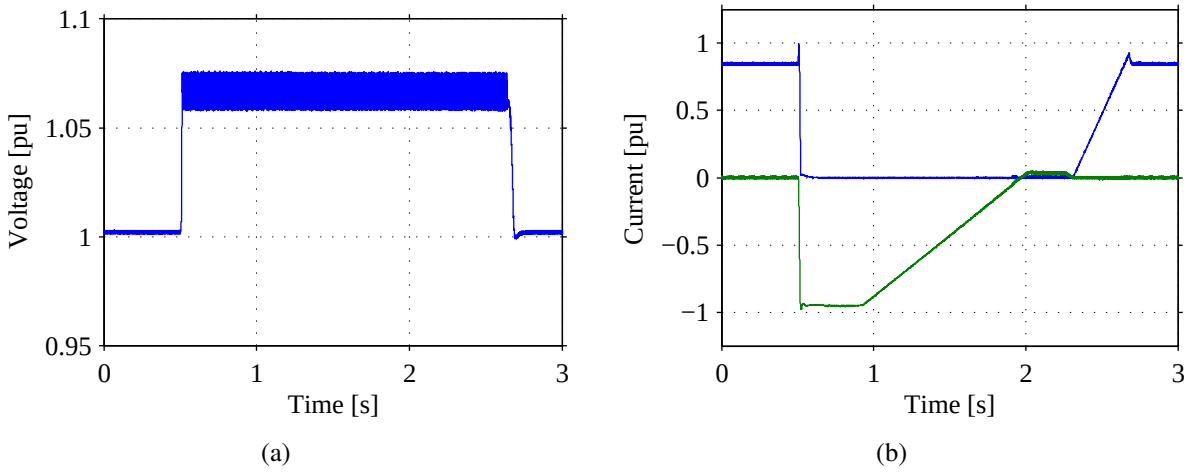

Fig. 6.16 Wind turbine LVRT control under a voltage dip. Plot (a): DC voltage $\underline{u}_{\mathrm{dc,w}}$; Plot (b): active current $\hat{i}_{\mathrm{t,w_d}}$ (blue) and reactive current $\hat{i}_{\mathrm{t,w_q}}$ (green).

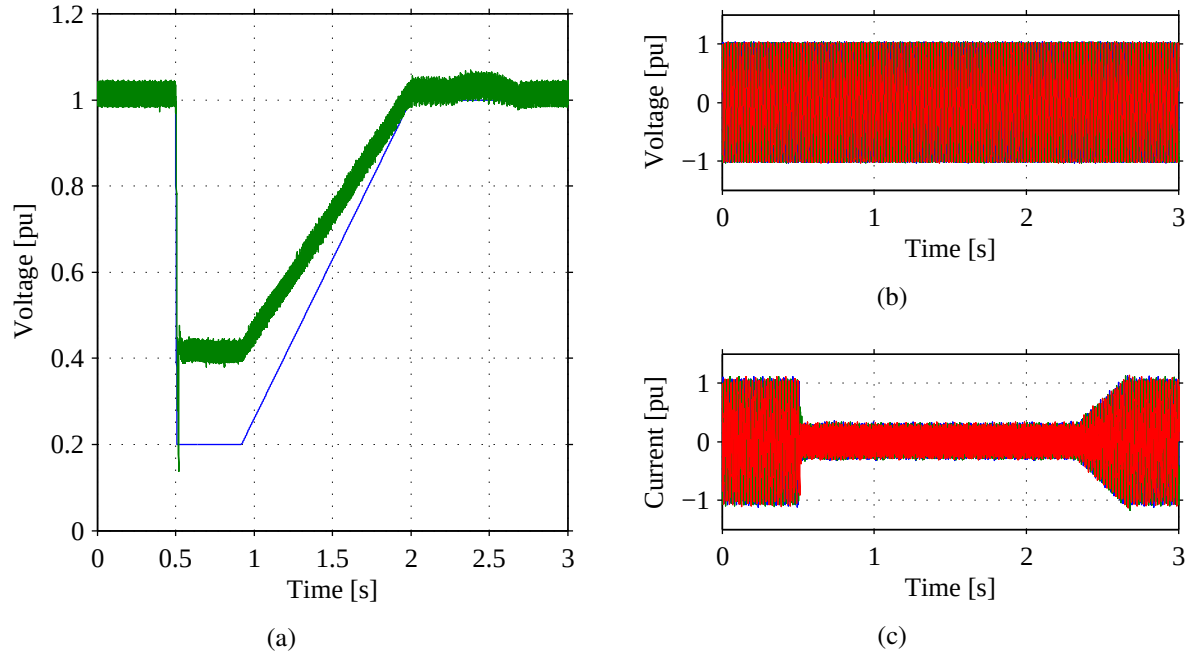

Fig. 6.17 PCC voltage control. Plot (a): reference voltage $|\underline{e}^*|$ (blue) actual magnitude of the PCC voltage $|\underline{e}|$ (green); Plot (b): actual three-phase grid filter voltage $\underline{e}_{\mathrm{g}}$; Plot (c): actual three-phase grid-VSC terminal current $\underline{i}_{\mathrm{t,g}}$.

dip. The active current of the wind turbine $\hat{i}_{\mathrm{t,w_d}}$ shown in Fig. 6.15(b) is controlled to 1 pu. The injected reactive power is 0.5 pu, as depicted in Fig. 6.15(c). Observe in Fig. 6.17(a) that the resulting PCC voltage is controlled above 0.4 pu, when the LVRT profile is in 0.2 pu.

As soon as the wind turbine voltage is recovering above 0.5 pu at 1 s, the reactive current $\hat{i}_{\mathrm{t,w_q}}$ shown in Fig. 6.16(b) is decreasing. For this reason, the resulting reactive power also decreases. Observe that, due to the reduction of reactive current between 1 s and 2 s, the actual PCC voltage

approaches the LVRT profile. The active power output is maintained in zero during the voltage dip and increases after 500 ms of the complete returning of the wind turbine voltage, at 2.3 s approximately.

The DC-link voltage of the wind turbine VSC is depicted in Fig. 6.16(a). The voltage increases rapidly when the wind tubine current $\hat{i}_{\mathrm{t,w_d}}$ is reduced to zero, as shown in Fig. 6.16(b). The crowbar protection of the wind turbine maintains the DC voltage below 1.075 pu. As soon as the limitation in the active current is removed, at 2.5 s approximately, the DC voltage controller manages to bring the DC-link voltage back to its reference.

Finally, the voltage at the grid connection point of the test equipment $\underline{e}_{\mathrm{g}}$ is depicted in Fig. 6.17(b). The three-phase current of the grid-VSC of the test equipment is also show in Fig. 6.17(b). Observe that when performing the test, there are no transients in the voltage nor the current. This is expected due to the decoupling that exists between the grid-side and collector-side. As seen in the figure, the grid voltage is practically unaffected, during the whole LVRT test. The current is mostly active current, resulting of the active power production of the wind turbine. The small amount of current between 0.5 and 2.5 s is due to the reactive power injection by the filter bank at the grid-side VSC of the test equipment.

6.3 Test of phase-angle jump during voltage dip

In this simulation, the ability of the test equipment in varying the phase angle of the PCC voltage during a voltage dip test is investigated. Here, the voltage is controlled at 1 pu and at 0.1 s it is dropped to 0.5 pu for 300 ms approximately. The angle θ of the reference voltage $\underline{e}^*$ is varied from 0 degrees to 30 degrees during the dip. The results are shown in Fig. 6.18.

Observe in Fig. 6.18(a) that the actual three-phase voltage $\underline{e}$ is zoomed during the dip and during the recovery. From the figure it is possible to observe that the voltage actually changes its phase. In Fig. 6.18(b) it is shown the d and q components of the PCC reference voltages $\hat{e}_{\mathrm{d}}$ (blue) and $\hat{e}_{\mathrm{q}}$ (green), respectively and also its references (black). The d component is controlled at its reference within 10 ms. The q is affected by the reaction of the wind turbine and it is controlled at its reference within 15 ms. Observe that in order to create a phase shift, the q component must be controlled at a value different than 0 pu, as compared with the case shown in Fig. 6.8 where only the d component is varied. Figure 6.18(c) shows the reference (blue traces) and the actual (green traces) phase-angle of the PCC voltage. The actual phase-angle of the voltage is controlled at its reference within 10 ms. An overshoot is seen at 0.11 s due to the dynamic of the voltage component $\hat{e}_{\mathrm{q}}$ shown in Fig. 6.18(b). The variation of the angle θ_{w} (red traces) tracked by the wind turbine PLL measured at the voltage $\underline{\hat{e}}_{\mathrm{w}}$ is also shown. Observe at 0.1 s that as soon as the reference phase-angle is varied, the PLL of the wind turbine takes 180 ms approximately to track the voltage vector $\underline{\hat{e}}_{\mathrm{w}}$. This is also delayed due to the fact that the actual phase-angle of the PCC voltage is 10 ms delayed with respect to its reference.

The magnitude of the wind turbine voltage is shown in Fig. 6.19(a) in blue traces. The magnitude of the PCC voltage and its reference value are also plotted in the figure in green and black traces, respectively. The PCC voltage is controlled at its reference within 12 ms after applying and after

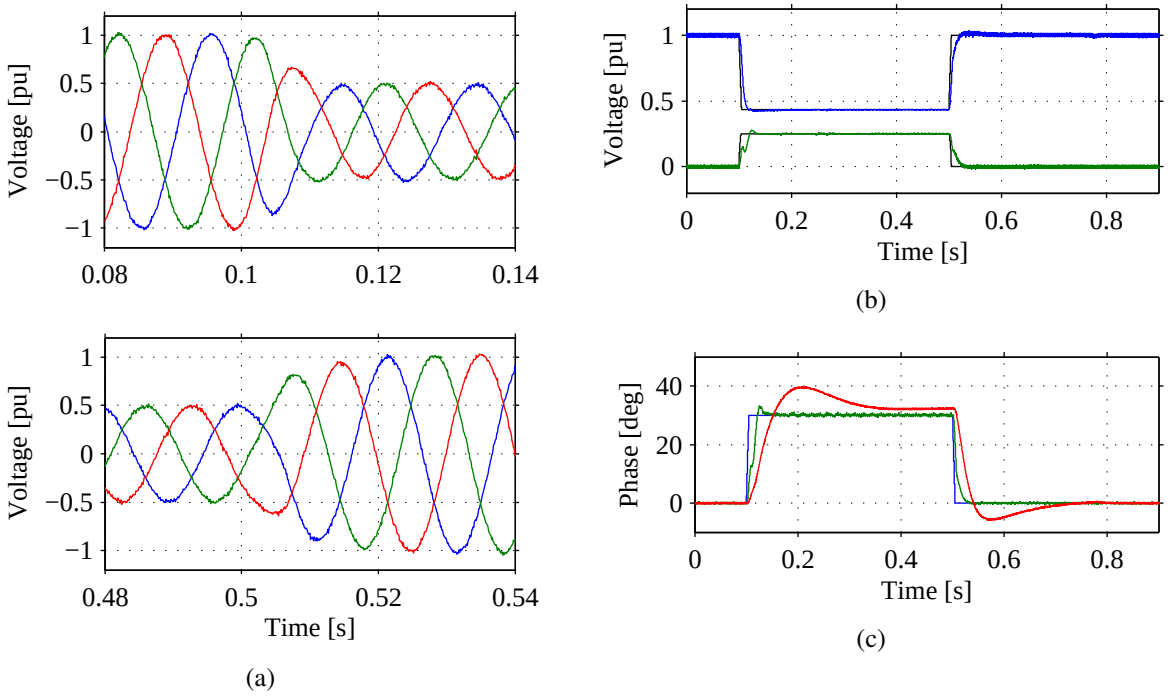

Fig. 6.18 Test equipment perfomance when testing for phase-angle jump during voltage dip: Plot (a): three-phase voltage voltage $\underline{e}^{\mathrm{abc}}$; Plot (b) d and q PCC reference voltages $\hat{e}_{\mathrm{q}}$ (blue) and $\hat{e}_{\mathrm{q}}$ (green), respectively, and its references (black). Plot (c): reference (blue) and actual (green) phase-angle in PCC voltage $\underline{e}$. Variation of the angle θ_{w} during the voltage dip, tracked by wind turbine PLL (red) at the voltage $\hat{\underline{e}}_{\mathrm{w}}$.

the recovery. The wind turbine d and q currents are shown in Fig. 6.19(b) in blue and green traces, respectively. Observe that the d and q currents are controlled properly to 0.8 pu and -0.85 pu, respectively, and that the magnitude of the current (black) is controlled to 1 pu during the dip, meaning that the wind turbine controller is able to control the current during the phase shift. However, when a phase shift is applied in the AC-link, the rotating dq frame of the wind turbine controller is not in synchronism with the angle of the voltage $\underline{e}_{\mathrm{w}}$ due to the delay introduced by the PLL. For this reason, the current $\hat{i}_{\mathrm{t,w_d}}$ does not represent the active current and the current $\hat{i}_{\mathrm{t,w_q}}$ does not represent the reactive current, at least for the first 140 ms after the phase shift. The effect of the transitory asynchronism of the dq frame is clearly shown in Fig. 6.19(c) where the active (blue traces) and reactive (green traces) power are depicted. Observe at 0.12 s that the active power is decreased to 0.25 pu and that the reactive power peaks at 0.55 pu while the d and q components of the wind turbine currents and PCC voltage are controlled without transients. Note that the resulting wind turbine voltage is boosted by the reactive power injected by the wind turbine, as shown in Fig. 6.19(a). Moreover, the active and reactive power set-point impact the resulting phase-angle of the wind turbine voltage, which is dependent of the impedance across the AC-link. For this reason, the angle variation measured by the PLL of the wind turbine is greater than 30 degrees, as shown in red traces in Fig. 6.18(c). At 0.5 s the angle is restored to 0 degrees and the wind turbine increases the active power output to 0.65 pu while decreasing the reactive power to 0 pu. Observe that the d and q currents are controlled at 0.65 pu and 0 pu

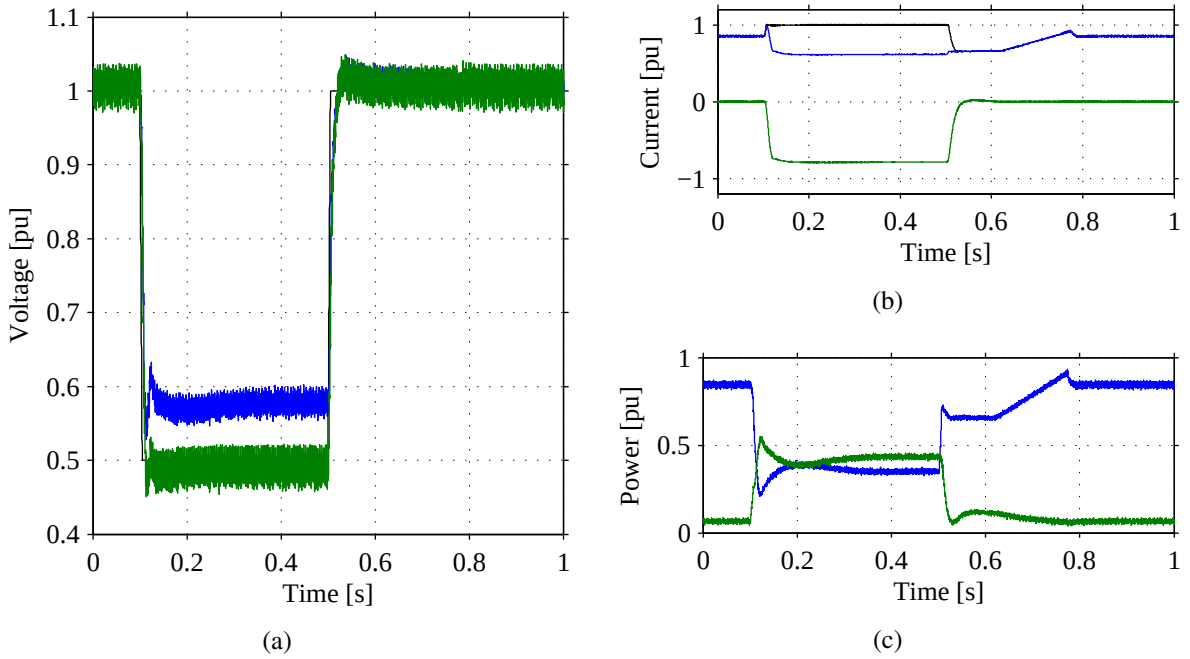

Fig. 6.19 Wind turbine test for phase-angle jump during voltage dip: Plot (a): reference voltage $|\underline{e}^*|$ (black) actual magnitude of the PCC voltage $|\underline{e}|$ (blue) and actual magnitude of the wind turbine voltage $\underline{e}_{\mathrm{w}}$ (blue); Plot (b): active current $\hat{i}_{\mathrm{t,w_d}}$ (blue), reactive current $\hat{i}_{\mathrm{t,w_q}}$ (green) and current magnitude $|\underline{\hat{i}}_{\mathrm{t,w}}|$ (black); Plot (c): active (blue) and reactive (green) power output.

respectively.

6.4 Test of single-phase voltage dip

In addition to the three-phase LVRT requirement given in the majority of grid codes, some of the most elaborated grid code require wind turbines to withstand asymmetric voltage dips. For instance, the Danish grid code [22] states that the wind turbine unit must be tested against single-phase and two-phase voltage dip for a duration of 150 ms. In [51] it is given a methodology to replicate phase-to-ground faults by feed-forwarding a pre-calculated zero sequence voltage. Observe in Fig. 4.2 that here the test equipment is interfaced by a delta-star transformer, decoupling the zero sequence equivalent circuit between the PCC and the wind turbine circuit. For this reason, only the positive and negative sequence voltage can be effectively regulated by the VSC in the investigated setup. In order to demonstrate the flexibility of the VSC-based testing equipment in reproducing unbalance voltage dips, a single-phase voltage sag test is presented in this section. Here, the open-loop control given in Section 4.4.2 has been implemented in three-phase form, meaning that the magnitude of each phase voltage is selected independently [52]. In this simulation, only phase C of the collector-VSC voltage is dropped to 0.5 pu for 150 ms while phase A and B are maintained at 1 pu. The resulting three-phase voltage at the PCC and three-phase current output of the wind turbine system are shown in Fig. 6.20.

As experted, the unbalanced voltage at the collector-VSC leads to an unbalanced PCC voltage

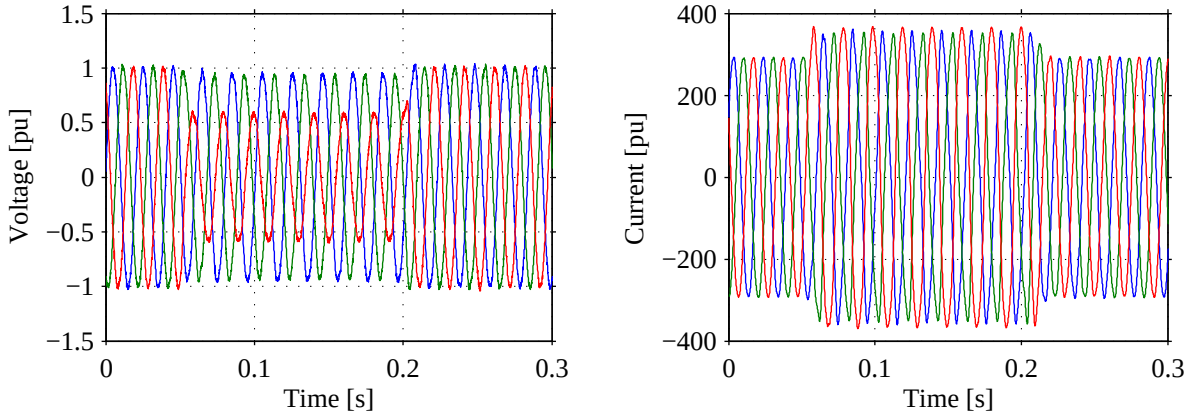

Fig. 6.20 Test for single-phase voltage dip: Plot (a): three-phase PCC voltage $\underline{e}^{(\mathrm{abc})}$. Plot (b): three-phase current $\underline{i}_{\mathrm{w,g}}^{(\mathrm{abc})}$.

$\underline{e}$ and an unbalanced wind turbine current output $\underline{i}_{\mathrm{wg}}$ as shown Fig. 6.20(a) and Fig. 6.20(b), respectively. Moreover, due to the unbalanced voltage drop across the filter inductance of the collector-VSC, the resulting PCC voltage in phase A (blue) and B (green) are slightly phase-shifted and the peak values are reduced to 0.97 pu, while phase C (red) drops to 0.5 pu.

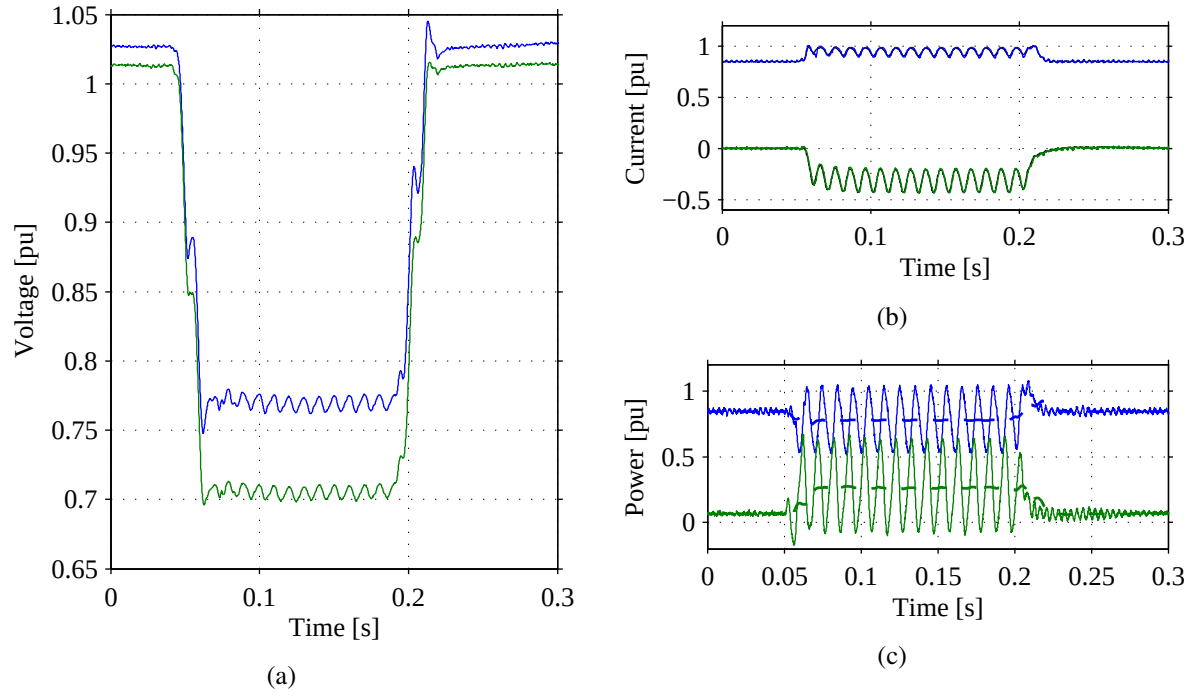

Fig. 6.21 Wind turbine performance during single-phase voltage dip: Plot (a): WT voltage (blue) and PCC voltage (green) RMS values. Plot (b): active current $\hat{i}_{\mathrm{t,w_d}}$ (blue), reactive current $\hat{i}_{\mathrm{t,w_q}}$ (green) and references (black); Plot (c): active (blue) and reactive (green) power output of the wind turbine and its average values (dashed).

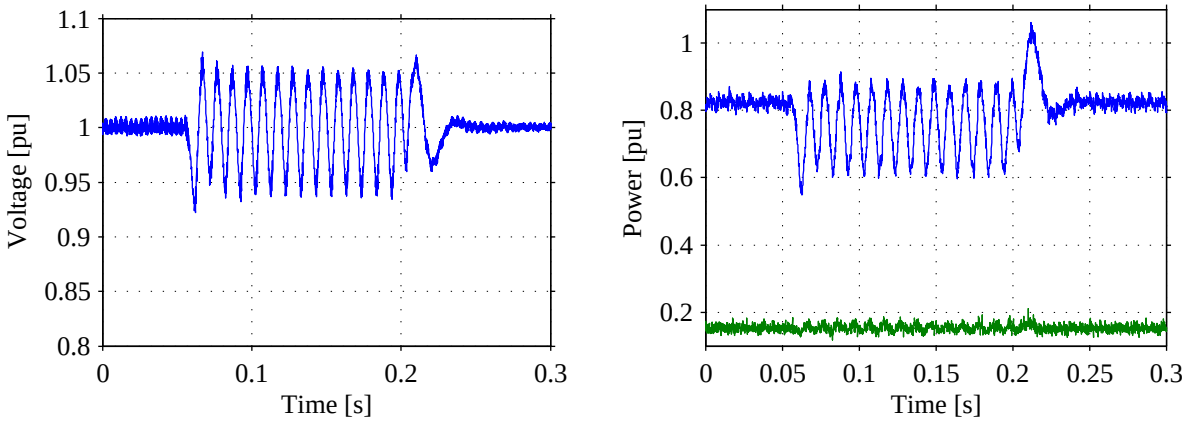

(a) (b)

Fig. 6.22 Grid-side VSC performance during single-phase voltage dip: Plot (a): three-phase PCC voltage u_{DC}. Plot (c): active (blue) and reactive (green) power output of test equipment towards the the AC grid.

As expected, the wind turbine current in the MV side of the output transformer $\underline{i}_{\mathrm{w,g}}$ is also unbalanced.

The RMS magnitude of the wind turbine voltage $\underline{e}_{\mathrm{w}}$ and the PCC voltage are shown in blue and green traces, respectively, in Fig. 6.21(a). Observe that the LVRT control action of the wind turbine boost the RMS value of the voltage to 0.77 pu and the RMS value of the PCC voltage is at 0.71 pu. Since the implemented open-loop control imposes the voltage only at the terminals of the collector-VSC of the test equipment, both the PCC voltage and wind turbine voltage are boosted. The active and reactive current output are depicted in Fig. 6.21(b) in blue and red traces, respectively, and its references are shown in black. As shown in the figure, in case of unbalanced condition of the grid, the current and also the voltage will show an oscillatory component at frequency equal to double the grid frequency. This is due the fact that the three-phase current and voltage vectors have a negative-sequence component which rotate in the opposite direction with respect to the synchronously rotating dq reference frame. An alternative to improve the performance of the controller of the VSC during unbalance condition is to modify the control system in order to control separately positive-sequence and negative-sequence current. These modifications are presented in [53].

Observe that the active and reactive power output shown in Fig. 6.21(c) in blue and green traces, respectively, exhibit an oscillatory response. In the figure it is also shown the average value of both powers. Note that even during an unbalance voltage dip, the modeled wind turbine can still provide reactive power support. Moreover, since the resulting voltage dip at the terminals of the wind turbine is not severe, the generating unit can sill deliver active power into the grid.

Finally, it is of interest to analyze the effect oscillatory power across the AC-link in the grid-side VSC the test equipment. In Fig. 6.22(a) it is shown the DC-link voltage u_{DC} of the testing equipment. From the figure it is possible to observe that the power oscillation experienced by the wind turbine leads to a second harmonic oscillatory response of the DC voltage. It is well known that VSC are sensitive to 2nd order harmonics in the DC-link when connected to an unbalanced

AC system [54]. Note that the amplitude of the oscillation is strictly related to the operating point of the wind turbine and to the nature of the test. Moreover, in Fig. 6.22(b) it is shown the active and reactive power output in blue and green traces, respectively, of the test equipment. Observe that the power fluctuation is propagated into the AC gird. In order to ensure a reliable operation and increased lifespan of the testing equipment, a proper mitigation strategy must be implemented either by hardware or in the controller of the grid-VSC.

6.5 Test of two consecutive two-phase voltage dips

A TSO can also require to wind turbines manufactures to withstand two consecutive voltage drops at the point of common coupling of the wind power plant. Note that if the fault in the AC system is not cleared, the action of an automatic reclosure at the point of the fault will lead to a second voltage drop at the wind turbine terminals. The requirements given in the Danish grid code [22] specifically says that the wind power plant must be designed to withstand recurring faults. In particular, two consecutive single-phase to ground and two-phase (with and without earth contact) voltage drops of 150 ms each, separated by 0.5 to 3 seconds

The impact of a single-phase voltage dip test in the testing equipment and wind turbine system has been covered in the previous section. In this final scenario, the test equipment is used to generate two recurring two-phase voltage dips. Similarly to the previous case, the three-phase open-loop control given in [52] has been implemented. Here, Phase A is controlled at 1, and phases B and C are dropped to 0.3 pu for 150 ms. In order to show the dynamic behavior of the system within a reasonable time resolution, the second voltage dip is programmed 150 ms after the first voltage dip is restored. The wind turbine is injecting 0.9 pu of active power into the AC-link. The resulting three-phase PCC voltage is given Fig. 6.23(a) and the current output of the wind turbine system is shown in Fig. 6.23(b). In the figure it is possible to observe that both the current and the voltage become severely unbalanced. Observe that under an two-phase voltage dip, the wind turbine manage to control the current below 1 pu.

The power output from the wind turbine is also heavily distorted, similar to the waveforms shown in Fig. 6.21(c). For this reason, only the average of the active and reactive power output has been plotted in Fig. 6.23(c), in blue and red traces, respectively. Note that the LVRT control strategy manages to reduce active power production and increase the injection of reactive power during the voltage dip. The resulting RMS value of the PCC voltage and wind turbine voltage are shown in Fig. 6.24(a), in green and blue traces, respectively. Observe that due to the control action of the wind turbine during dip, the resulting RMS voltage at the wind turbine terminals is 0.48 pu and the PCC voltage is 0.35 pu.

The active and reactive current are shown Fig. 6.24(b) in blue and green traces, respectively.The LVRT control strategy varies the reactive current according to the magnitude of the voltage dip, while the active current is maintained at 0.45 pu. The reference current is shown in black traces in the figure. Observe that the controller manages to control both d and q current during unbalanced conditions. The 100 Hz oscillation in both actual and reference currents are due to the feed-forward of the d and q component of the voltage when calculating the references.

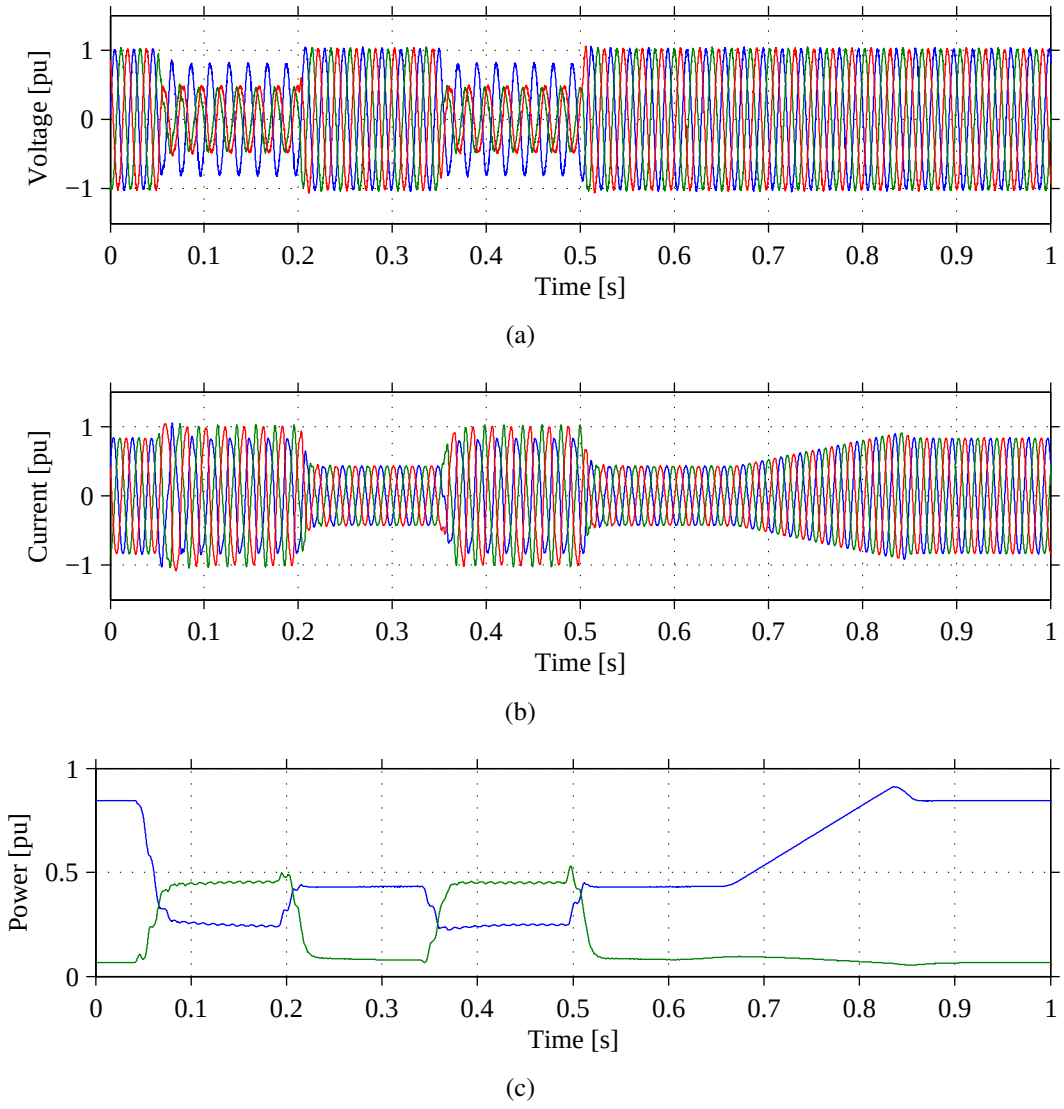

Fig. 6.23 Test for two-phase voltage dip: Plot (a): three-phase PCC voltage $\underline{e}^{(\mathrm{abc})}$. Plot (b): three-phase current $\underline{i}_{\mathrm{w,g}}^{(\mathrm{abc})}$; Plot (c): filtered active (blue) and reactive (green) power output of the wind turbine.

Finally, due to the reactive power injected by the AC filters at 0.3 s, the reactive power is maintained at a minimum value of 0.1 pu when the voltage is restored between the dips. Moreover, the q current is set to zero. The second voltage dip is produced by the test equipment at 0.36 s. A similar behavior of the system is expected. Observe that the wind turbine injects 0.4 pu of reactive power, until the recovery of the voltage at 0.5 s. After 150 ms, the wind turbine starts to resume active power production with a smooth ramp function. At 0.89 s, the generating unit resumes normal operation.

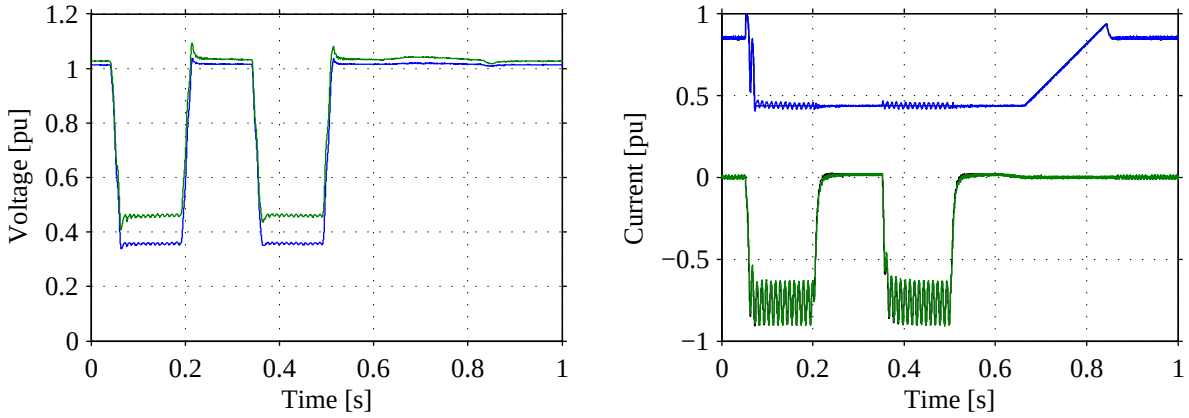

(a) (b)

Fig. 6.24 Grid-side VSC performance during single-phase voltage dip: Plot (a): WT voltage (blue) and PCC voltage (green) RMS values. Plot (b): active current $\hat{i}_{\mathrm{t,w_d}}$ (blue), reactive current $\hat{i}_{\mathrm{t,w_q}}$ (green) and references (black).

6.6 Experimental verification of the testing methodology

The aim of this section is to validate experimentally part of the simulation results obtained in the previous section. Here, a description of the laboratory testing setup together with the experimental results is presented. The complete test-bench is shown in Fig. 6.25, and it is located at the Power System Laboratory placed the Department of Energy and Environment of Chalmers University of Technology, Gothenburg, Sweden.

The grid-VSC of the testing equipment is here represented by the the DC-sourced VSC. In order to replicate independently the operation and control of the two systems, here the switching signals of each converter are generated by two dedicated DS1103 dSPACE board. The voltage is controlled in open-loop. The small scale model of the wind turbine is modelled by a second VSC with a diode-rectifier connected to its DC-link. The AC side of the diode-rectifier is connected to a 400 V AC grid and it is used to transfer active power from the grid into the DC-link of the wind turbine model. The VSC is operated in current control mode in order to inject the power into the AC-link imposed by the test equipment. In order to limit the current that flows into the capacitor $C_{\mathrm{DC,w}}$ when energizing the system, the resistor R_{l} has been placed between the 400 V AC grid and the diode-rectifier of the wind turbine model. When the DC-link voltage reaches 550 V, the parallel contactor is closed and the resistor is bypassed. At this instance, the diode-rectifier is directly connected to the 400 V grid and thus the DC-link voltage is imposed at 556 V. The AC-link is controlled in open loop at 200 V by the collector-VSC. The DC-machine that supply the DC voltage of the testing equipment is controlled at 360 V. In the following, all the sub-modules that constitute the laboratory setup are first verified independently. Afterwards, the sub-system and controllers are integrated in one complete test-bench as shown in Fig. 6.25.

The physical implementation of the laboratory setup is shown in Fig. 6.26, where the main parts that constitute the test system are highlighted. Similarly, in Fig. 6.27 it is shown the inductive and capacitive filters used to interface the wind turbine model with the test equipment. Note

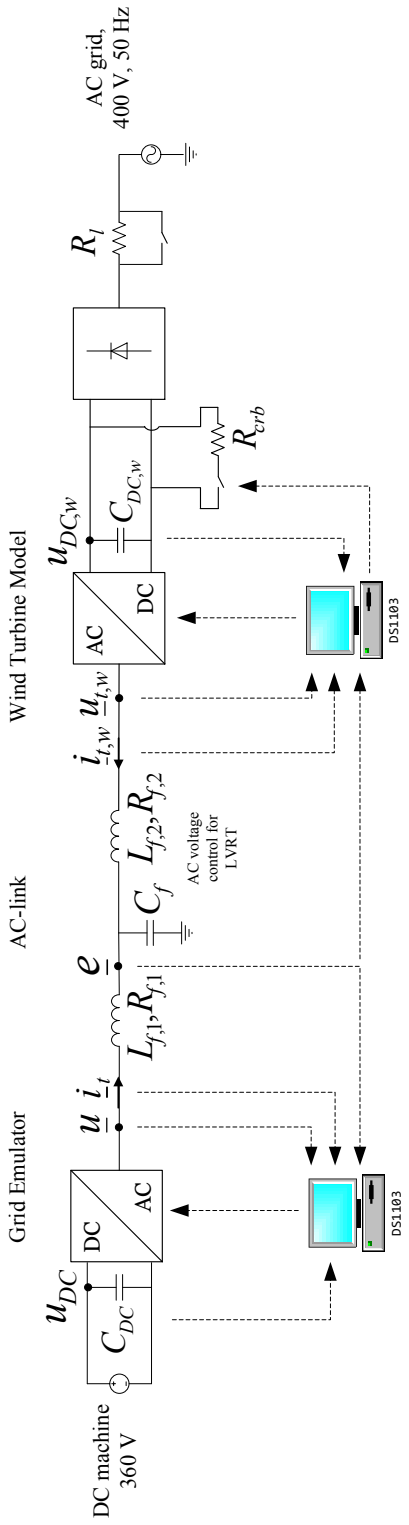

Fig. 6.25 Single line diagram of the laboratory setup fo LVRT test of the wind turbine model by VSC-based testing equipment.

TABLE 6.1. PARAMETERS OF THE LABORATORY SETUP.

Base parameters in AC-link		200 V, 3 kVA
Frequency		50 Hz
DC voltage (Machine)		360 V
DC voltage (Diode-rectifier)		650 V
DC capacitor test equipment	C_{DC}	6.6 mF
Filter inductance	$L_{\mathrm{f},1}$	3 mH
Filter internal resistance	$R_{\mathrm{f},1}$	5.3 mΩ
Filter capacitance	C_{f}	64 μF
Filter inductance	$L_{\mathrm{f},2}$	2 mH
Filter internal resistance	$R_{\mathrm{f},2}$	5.0 mΩ
DC capacitor in wind turbine model	$C_{\mathrm{DC,w}}$	2.2 mF
Current control bandwidth in wind turbine model	$\alpha_{\mathrm{cc,w}}$	1500 rad/s
Switching frequency of both VSC	f_{s}	5 kHz
Sampling time	t_{s}	0.2 ms

that the time response of the DC machine shown Fig. 6.27 is slow when changing its operating point, if the incoming power from the wind turbine model is varied. In this scenario, the power is shortly accumulated in the DC-link of the test equipment, leading to a high peak DC voltage transient that trips the converter. For this reason, a capacitor bank of 6.6 mF has been placed at the DC-link of the testing equipment in order to mitigate the dynamic of the DC voltage, as shown in the right-hand side of Fig. 6.27.

6.6.1 Dynamic performance of the derived current controller in a grid-connected VSC

In this section, an experimental verification of the devised current controller controller given in Chapter 4 is given. First, the performance of the current control is evaluated with special focus on the step response as well as in the decoupling of both d and q axis. Observe that the implemented current controller is used in both the testing equipment and in the wind turbine model. For this reason, this experimental setup is also used to test active and reactive power exchange for validation of the LVRT control strategy of the wind turbine model.

A single-line diagram of a reduced laboratory setup used to verify the dynamic performance of the current controller is depicted in Fig. 6.28. The VSC is connected to the grid through an inductor. The VSC is a two-level DC/AC converter, where the DC-link is fed by a DC machine rated in 700 V, 64 A, giving the possibility for the VSC to inject active power into the grid. Observe that the switch sw_{DC} is closed during the complete duration of test. The DC voltage at the terminals of the machine is controlled to 650 V by an external drive system connected in its shaft. The converter is controlled by a DS1103 dSPACE system [55]. The discrete controller is built and compiled in Matlab R2011a [47]. The PWM switching frequency is set to 5 kHz and the sampling time is 0.2 ms. The system parameters of the laboratory testing setup is given in Table 6.2.

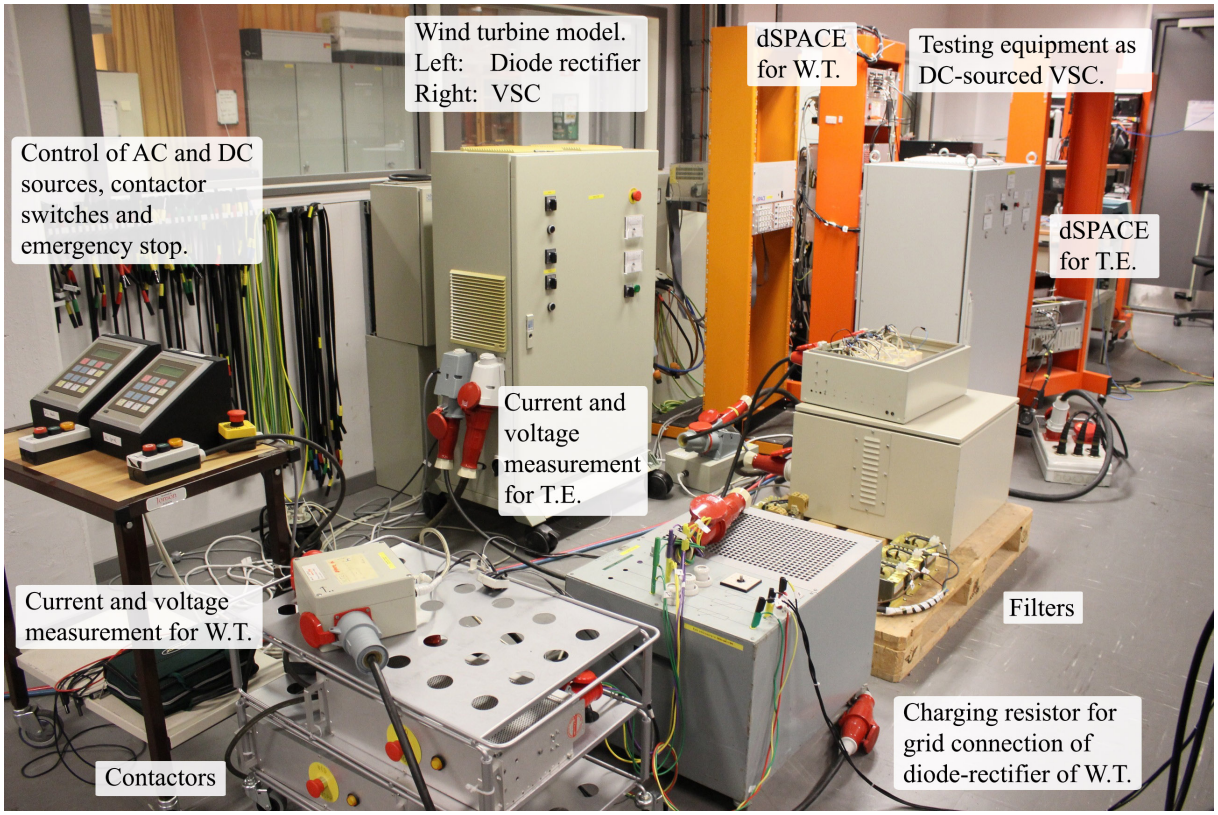

Fig. 6.26 Physical implementation of the laboratory setup.

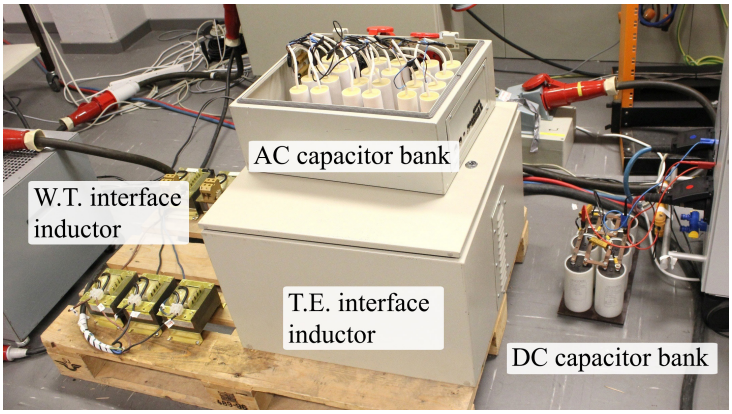

Fig. 6.27 AC and DC filter banks in the laboratory.

Current controller step response

To evaluate the performance of the current controller, the reference current in both d and q axis is varied with a step function. Here, a base power of 3 kW has been set into the VSC controller and the peak value of the steady-state current is limited to 10 A. The resulting waveform of each current component is shown in Fig. 6.29.

From Fig. 6.29(a) and Fig. 6.29(b) it is possible to observe that the d axis component of the

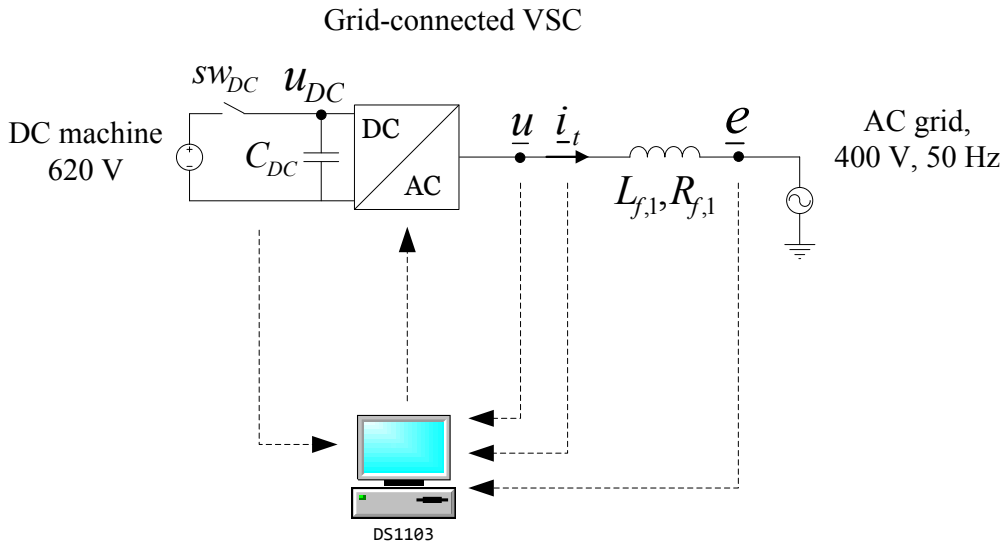

Fig. 6.28 Single line diagram of the laboratory setup used for validation of the close-loop current control and DC voltage control.

current is decoupled from the q axis component, meaning that when the d current is varied, the q current remains unchanged and vice-versa. Moreover both step responses have similar rise times of about 5 ms. Observe, however, due to the harmonic distortion present in the grid voltage at the moment of the test, both current components presents large amount of harmonics. These harmonics are therefore shown as an oscillatory component when the current vector is represented in a 50 Hz synchronously rotating dq reference frame. Moreover, since the controller is implemented in a digital system, delays due to discretization and computational time in the control system result in a phase shift between the actual and feed-forwarded grid voltage $\hat{\underline{e}}^{(\mathrm{dq})*}$, in the control scheme shown in Fig. 4.4 [56]. In [56] and [57] it is discussed the use of an improved harmonic-compensated current controller in order to deal with harmonic disturbances. Here, the performance of the implemented current controller is found to be sufficient in controlling the d and q components of the current vector. Finally, this example validates the ability of the grid-connected VSC in controlling the current by using the discrete controller devised in Section 4.4.1.

TABLE 6.2. PARAMETERS OF THE REDUCED LABORATORY SETUP FOR TESTING OF CURRENT CONTROL AND DC VOLTAGE CONTROL

Base values		400 V, 3 kVA
Grid frequency		50 Hz
DC voltage		620 V
Current control bandwidth	α_{cc}	3000 rad/s
DC voltage control bandwidth	α_{dc}	300 rad/s
Switching frequency of VSC	f_{s}	5 kHz
Sampling time	t_{s}	0.2 ms

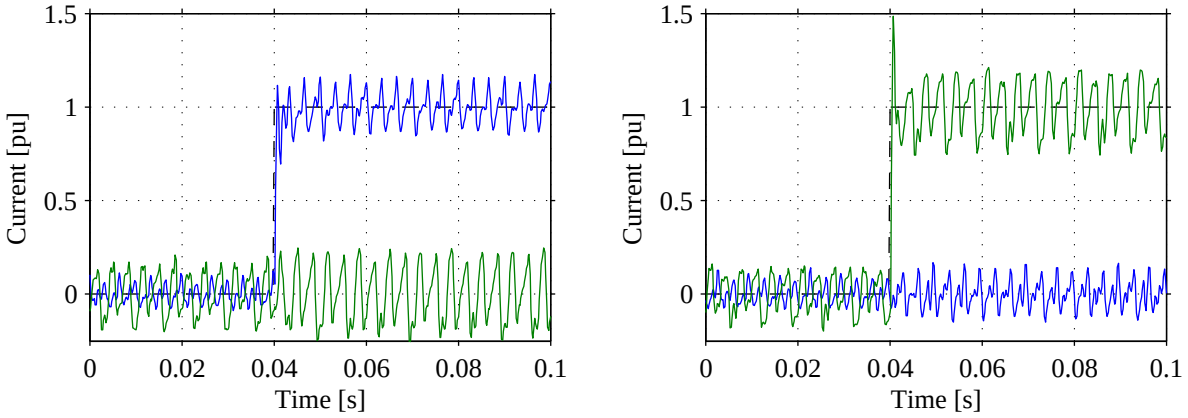

Fig. 6.29 Experimental validation of the implemented current controller. In plots: estimated active current $\hat{i}_{\mathrm{t_d}}$ (blue) and estimated reactive current $\hat{i}_{\mathrm{t_q}}$ (green). Plot (a): step response when reference current $i^*_{\mathrm{t_d}}$ (black-dashed) is varied. Plot (b): step response when reference current $i^*_{\mathrm{t_q}}$ (black-dashed) is varied.

Current control in wind turbine model when detecting a voltage dip.

In this experiment, the current controller validated in the previous section is used to inject active and reactive power into the grid, when a voltage dip is detected by the wind turbine. Here, the VSC is connected to an infinite bus, as depicted in Fig. 6.28. Moreover, for this test, the signal that encloses the grid voltage magnitude is varied internally and is sent into the LVRT control strategy of the wind turbine controller, shown in the control diagram in Fig. 4.16. Observe that for this experiment the grid voltage is fixed by the AC grid at 400 V. The LVRT control strategy implemented in the wind turbine model is set according to the German grid code. In simple words, if the grid voltage decreases below 0.9 pu, the wind turbine must inject reactive current enabling 1 pu current when the voltage is below 0.5 pu. Active current must be limited accordingly, in order to give room for reactive current support. The latter means that for 1 pu reactive current, active current must set to 0 pu if the wind turbine does not have over-current capability.

In Fig. 6.30 it is shown the wind turbine control strategy when a virtual voltage dip is detected at its terminals. The left figures correspond to the wind turbine response when a voltage dip of 0.8 pu is detected, while the right figures correspond to the wind turbine response when a voltage dip of 0.4 pu is detected. Observe in Fig. 6.30(b) that for a small variation of the voltage signal, the LVRT control strategy sets the reactive current to -0.2 pu. The active current reference remains unchanged. In the second scenario (which corresponds to the plots the right-hand side of Fig. 6.30), the active current is decrease from 0.9 pu to 0 pu in order to give room to a reactive current of -1 pu. Observe in Fig. 6.30(b) that the converter is injecting full reactive current into the grid when the voltage (control signal) is below 0.5 pu. For voltages above 0.5 pu, the reactive current is linearly varied. The change in active and reactive current set-point are set in order to maintain the VSC current at 1 pu. The resulting active and reactive power in Fig. 6.30(c) are the results of the controlled current when the VSC is connected to a grid at nominal voltage.

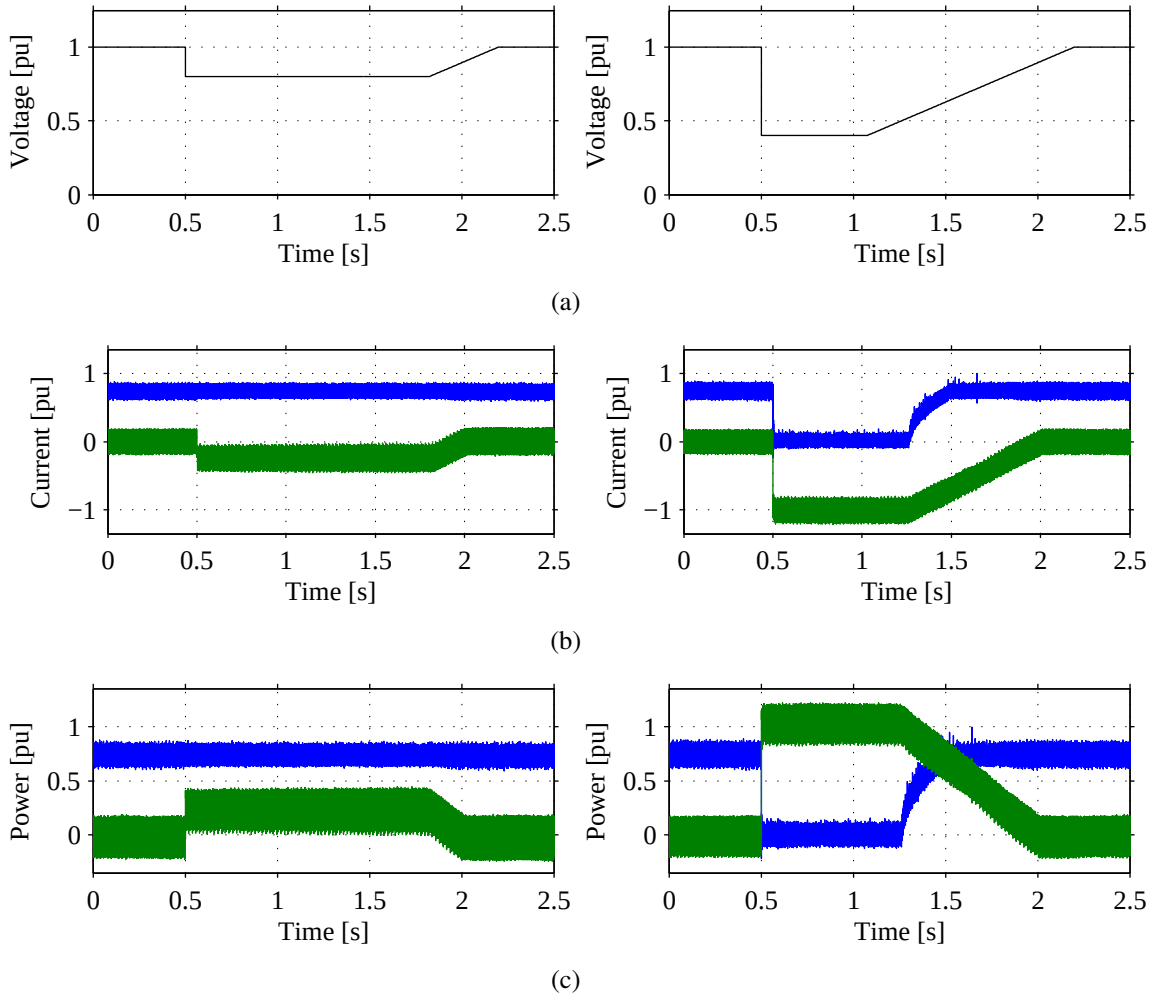

Fig. 6.30 Experimental verification of the LVRT control strategy of the wind turbine model. Left figures: voltage dip to 0.8 pu. Right figures: voltage dip to 0.4 pu. Plot (a): control signal $|\ \hat{\underline{e}}\ |$; Plot (b): converter current $\hat{i}_{\mathrm{t_d}}$ (blue) and $\hat{i}_{\mathrm{t_q}}$ (green). Plot (c): active (blue) and reactive(green) power output.

6.6.2 DC voltage control in grid-side of the test equipment

In this section, the implemented DC voltage controller given in Section 4.5.3 is validated through experimental verification. The utilized laboratory setup is shown in Fig. 6.28. Observe that for this experiment, the switch sw_{DC} is opened once the DC-link is at 630 V. The DC voltage reference is set to 620 V and varied with a step function to 630 V. In Fig. 6.31 is shown the step response of the implemented controller.

As shown in the figure, the voltage across the DC-link capacitance of the VSC is controlled in an smooth way. With a selected bandwidth of 300 [rad/s] (see section Section 4.5.3), the step response shows a rise time of 12 ms which is longer than expected. If the capacitance $\hat{C}_{\mathrm{DC}}$ used in the controller is underestimated with respect to the actual capacitance C_{DC}, the actual bandwidth of the close-loop DC controller is lower, leading to a longer rise-time when a step is applied at the reference DC voltage.

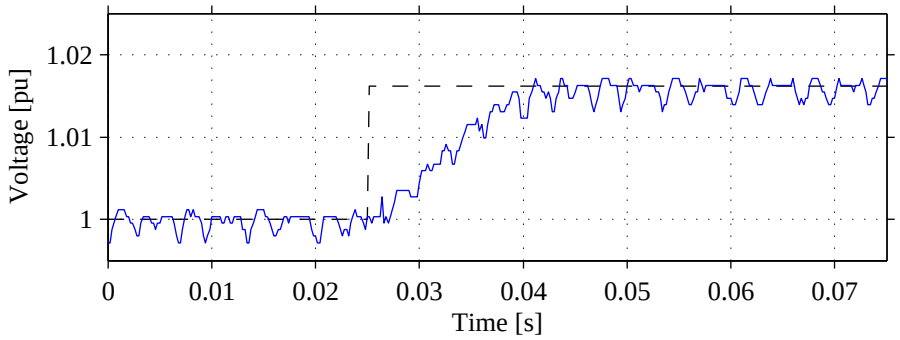

Fig. 6.31 Normalized step response of the implemented DC-link voltage controller: voltage reference (black dashed) and sampled voltage $\hat{v}_{\mathrm{DC}}$ of the VSC (blue).

6.6.3 AC voltage control in collector-side of test equipment

In this section, the open-loop PCC voltage control given in Section 4.4.2 is validated. The laboratory setup used in this experiment is shown in Fig. 6.32. The VSC is fed by a DC machine and the AC side is connected to a resistive load R_{l} of 45 Ω through an LCL filter. The system parameters for this experiment are given in Table 6.1. Here, no filter compensation is used, meaning that the voltage reference $\underline{e}^{(\mathrm{dq})*}$ is fed into the reference output voltage of the VSC.

A voltage dip test is performed by applying a voltage variation with a step function at PCC where a resistive load is connected. In order to avoid a fast variation of the converter voltage that can lead to undesired stress in the system, as discussed in Section 6.2.2, the reference voltage is low-pass filtered with bandwidth of 300 [rad/s]. Meaning that the reference converter voltage is varied with a ramp-rate of 0.1 pu/ms, approximately, as selected in Section 6.2.2.

As discussed in Section 6.2.2, the open-loop control has been found to be robust when performing

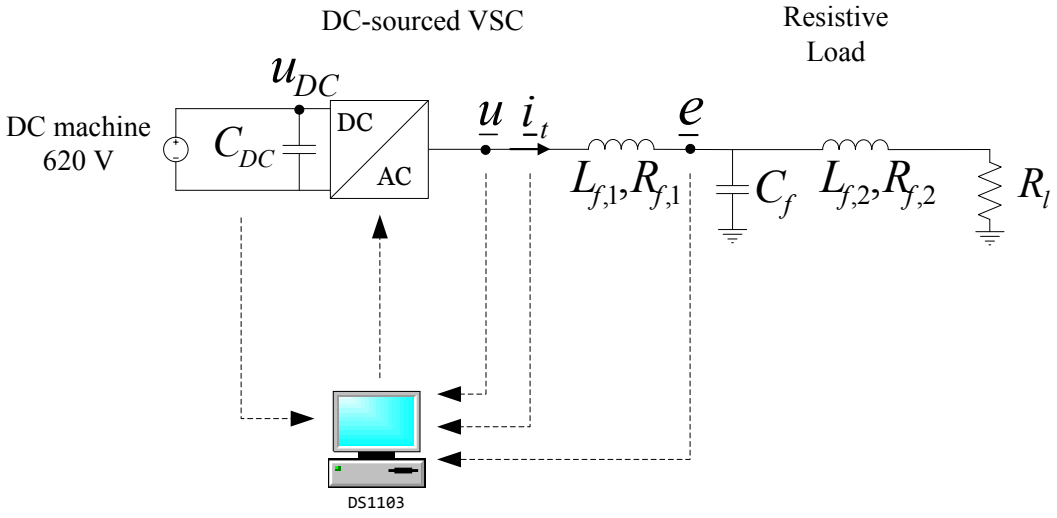

Fig. 6.32 Single line diagram of the laboratory setup for testing open-loop AC voltage control.

a LVRT test and gives a acceptable dynamic performance if the ramp-rate of converter reference voltage is properly selected. Moreover, this type of controller has been used to test a 4 MW FPC wind turbine by using the back-to-back HVDC station placed at Gothenburg's harbour [41]. For these reasons, the open-loop controller without filter compensation given in (4.41) has been selected for implementation in the laboratory.

In Fig. 6.33 is shown the resulting load voltage when testing for a voltage dip and LVRT tests. Observe in Fig. 6.33(a) that for the first experiment the voltage is dropped to 0.3 pu during 200 ms. Afterwards, the voltage is restored with a step function and not with a recovery ramp as given in the majority of the grid codes.

In order to demonstrate the flexibility of the investigated methodology, in the following, the load is tested against a full LVRT profile which includes the recovery ramp when the voltage is restored. The LVRT test is performed by varying the PCC voltage according to a desired LVRT profile. Here, German grid code for off-shore wind turbines has been selected for testing. The reference voltage is dropped to a retained value of 0.3 pu and maintained approximately 400 ms. Afterwards, the voltage is brought back to 1 pu with a rate of 0.77 pu/s. The voltage profile is also given in Fig. 6.35(b). The resulting load voltage is shown in Fig. 6.33(b). Observe that the actual load voltage is slightly below 0.3 pu. This is due to the voltage drop across $L_{\mathrm{f},1}$ that is not being compensated by the open-loop controller. This results demonstrate the capability of the open-loop voltage controller in performing any kind of voltage reference at the terminals of the VSC.

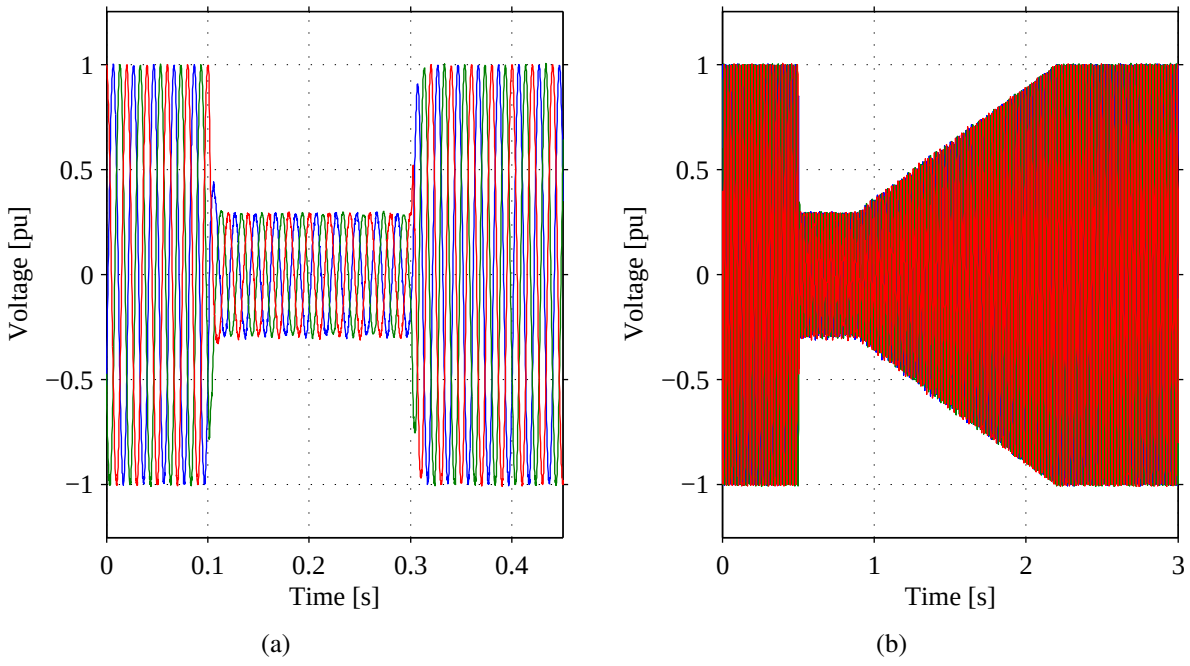

Fig. 6.33 Resulting three-phase LR load voltage when the open-loop PCC voltage controller is performing a: Plot (a) voltage dip; and Plot (b): LVRT profile.

6.6.4 Testing of voltage dip and complete LVRT profile on wind turbine model

In the previous section the independent controllers for the grid-VSC of the test equipment has been verified. The wind turbine controller including PLL, current control and DC voltage control have been also tested. Here, all the sub-modules that constitute the testing bench are integrated in one setup as shown in Fig. 6.25. In the following, the wind turbine model is tested against voltage dips including the recovery ramp, by means of the implemented VSC-based testing equipment.

Voltage dip by VSC with PQ control strategy of wind turbine model

In this scenario, the AC voltage at the terminals of the collector-VSC is reduced from 1 pu to 0.3 pu and maintained for approximately 600 ms. Afterwards, the voltage is restored back to 1 with

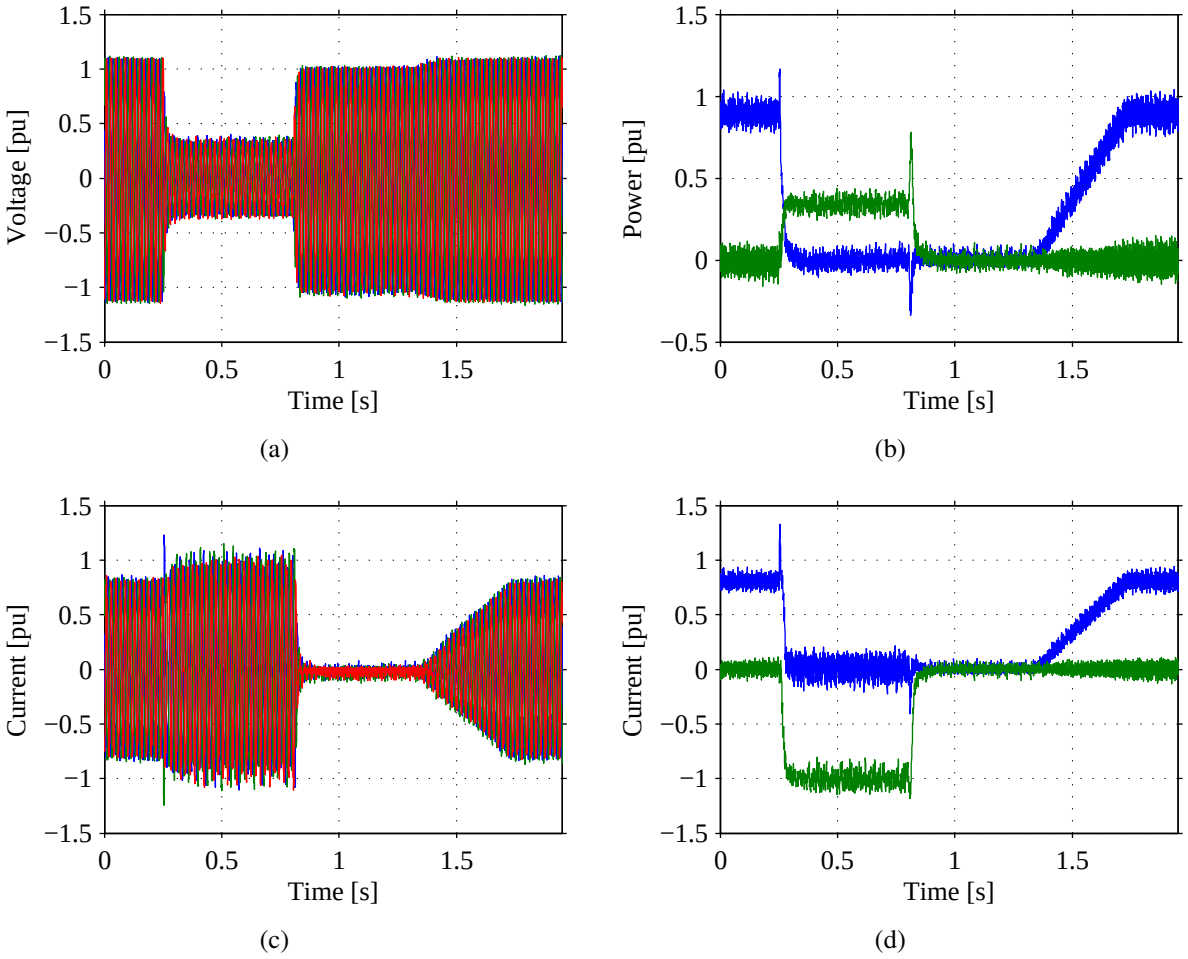

Fig. 6.34 Voltage dip test in laboratory setup: Plot (a): Three-phase voltage $\underline{e}^{(\mathrm{abc})}$; Plot (b): Active power P_{w} (blue) and reactive power Q_{w} (green) output of the wind turbine model. Plot (c): Three-phase current $\underline{i}_{\mathrm{t,w}}^{(\mathrm{abc})}$; Plot (b): Active current $\hat{i}_{\mathrm{t,w_d}}$ (blue) and reactive current $\hat{i}_{\mathrm{t,w_q}}$ (green).

a step. The three-phase voltage at the PCC is shown Fig. 6.34(a).

The pre-fault active power output is set to 0.9 pu with at power factor, as depicted in Fig. 6.34(b). Hence, three-phase current $\underline{i}_{\mathrm{t,w}}^{(\mathrm{abc})}$ and the active current $\hat{i}_{\mathrm{t,w_d}}$ are controlled in 0.9 pu, as shown in Fig. 6.34(c) and Fig. 6.34(d) respectively. The reactive current $\hat{i}_{\mathrm{t,w_q}}$ is set to 0 pu prior the emulated fault. The wind turbine model is equipped with the LVRT control strategy for current control as given in the German grid code.

Observe that is the terminal voltage $\underline{u}$ of the testing equipment shown in Fig. 6.25 that is controlled at 1 pu before applying the voltage dip. In addition, the excess of voltage drop across the inductances $L_{\mathrm{f},1}$ and $L_{\mathrm{f},2}$ implemented in the laboratory setup are not being compensated in the open-loop voltage controller. Moreover, the capacitor bank C_{f} is boosting the voltage at the PCC during the test. For this reason, with reference to Fig. 6.34 at 0 s, the resulting PCC voltage $\underline{e}^{(\mathrm{abc})}$ shown in Fig. 6.34(a) is found to be 1.1 pu.

At 0.25 s the terminal voltage $\underline{u}$ is dropped to 0.3 pu. The PCC voltage is also in proximity to 0.3 pu slightly boosted by the reactive power injected by the wind turbine model. In order to increase the reactive current to 1 pu after detecting the fault, the active current must is kept in 0 pu. The maximum reactive power injected during the fault is 0.32 pu approximately. When the voltage is restored at 0.85 s, the wind turbine model cease of injecting reactive power into the grid, however, the algorithm of voltage/reactive power compensation (described in the German grid code) is still active for 500 ms after the voltage is back to normal operation. As discussed in previous section, two voltage dips can be experienced at the terminals of the wind turbine if a grid fault in the power system is not cleared. For this reason, the active current is still set to 0 pu while the LVRT control strategy actively monitoring the PCC voltage in order to supply reactive current if a second voltage dip is observed. After 500 ms it is assumed that the system is back into normal operation. At 1.35 s is resumed active power production by slowly removing a limiter in the active current set-point. Finally, within the next 400 ms the active current is restored back to its pre-fault value.

In the following, the testing equipment performs a voltage dip with the inclusion of the recovery ramp as given in grid codes.

LVRT test by VSC with PQ control strategy of wind turbine model

In this scenario, a complete LVRT profile is tested against the wind turbine model. Similar to the previous case, here the voltage is reduced from 1 pu to 0.3 pu and maintained for 600 ms. Afterwards, the voltage is brought back to 1 pu with a ramp function. The LVRT control strategy is also implemented in wind turbine model and the initial conditions are maintained (full active power production at unity power factor). The results from this experiment are given in Fig. 6.35.

The PCC voltage shown in Fig. 6.35(a) follows the LVRT voltage profile given as a reference in the collector-VSC of the testing equipment. As shown in Fig. 6.35(b), at 0.5 s when the voltage is reduced, the wind turbine model injects reactive power. Moreover, the reactive current $\hat{i}_{\mathrm{t,w_q}}$ shown in Fig. 6.35(d) is controlled in 1 pu at the moment of the voltage dip and the active current is $\hat{i}_{\mathrm{t,w_d}}$ set to 0 pu. As a result, the PCC voltage is boosted by the reactive power injected by the wind turbine model, reaching a value of 0.4 pu during the deepest of the fault while the

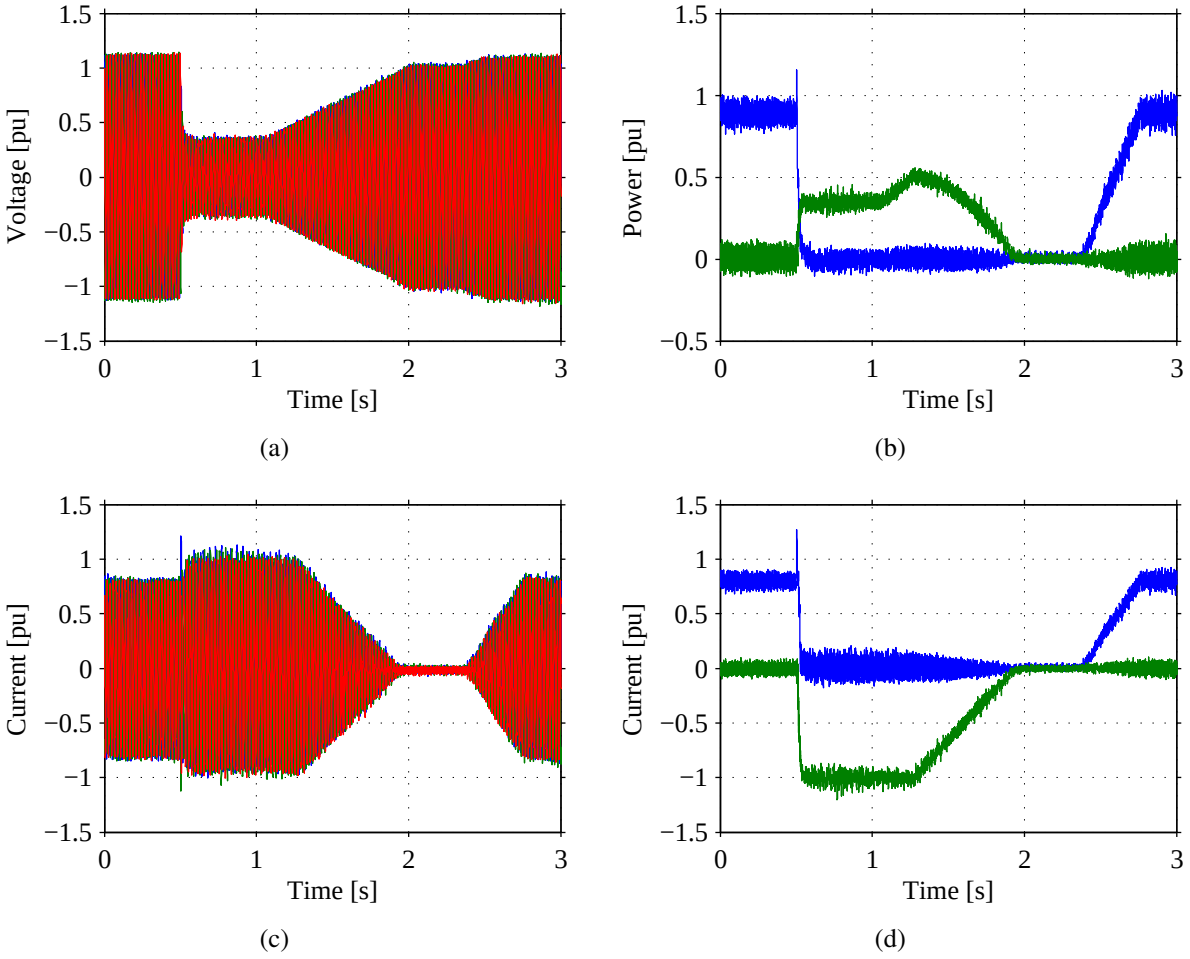

Fig. 6.35 LVRT test in laboratory setup: Plot (a): Three-phase voltage $\underline{e}^{(\mathrm{abc})}$; Plot (b): Active power P_{w} (blue) and reactive power Q_{w} (green) output of the wind turbine model. Plot (c): Three-phase current $\underline{i}_{\mathrm{t,w}}^{(\mathrm{abc})}$; Plot (b): Active current $\hat{i}_{\mathrm{t,w_d}}$ (blue) and reactive current $\hat{i}_{\mathrm{t,w_q}}$ (green).

three-phase current $\underline{i}_{\mathrm{t,w}}^{(\mathrm{abc})}$ is maintained within 1 pu.

The recovery of the voltage start at 1.2 s when the voltage is ramped from 0.3 pu to 1.0 pu. Observe that the reactive current reference is maintained at 1 pu for all times when the PCC voltage is below 0.5 pu. For this reason, the reactive power is increasing with the voltage reaching its maximum of 0.5 pu at 1.35 s. Afterwards, the reactive current $\hat{i}_{\mathrm{t,w_q}}$ is linearly reduced, as depicted in Fig. 6.35(d), according to the retained voltage at the PCC when this is above 0.5 pu. As a consequence, the reactive power decreases when the voltage increases towards 1 pu.

At 1.8 s the reactive current is set to 0 pu, meaning that the PCC voltage is recovered from the fault. After 500 ms, the wind turbine model resumes active power production by removing a limitation over $\hat{i}_{\mathrm{t,w_d}}$ with a controlled ramp function. Full active power production is achieved at 1.75 s.

In the next experiment, the response of the modelled wind turbine is studied when no LVRT control strategy is implemented and the power reference is maintained during the complete event.

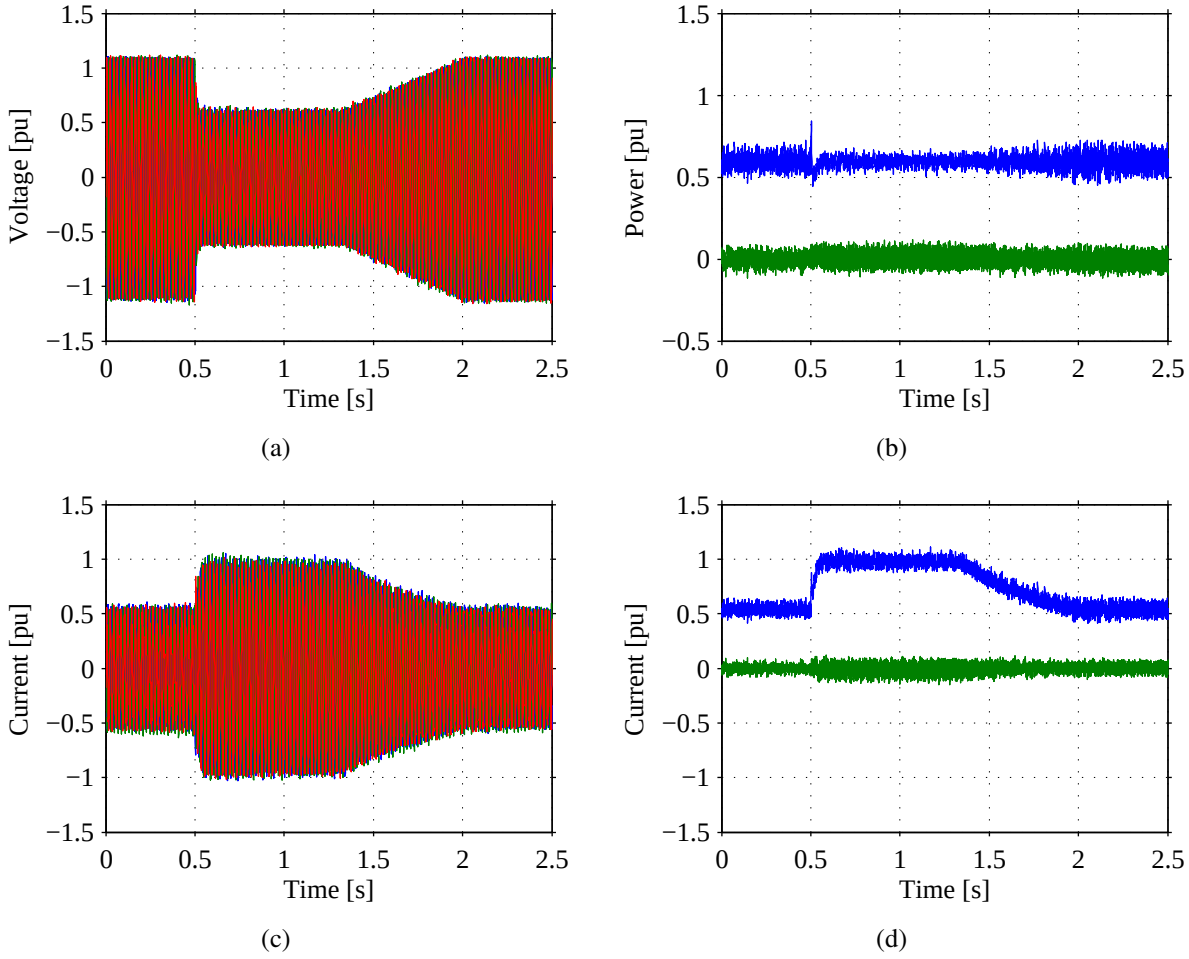

Fig. 6.36 LVRT test with constant power in laboratory setup: Plot (a): Three-phase voltage $\underline{e}^{(\mathrm{abc})}$; Plot (b): Active power P_{w} (blue) and reactive power Q_{w} (green) output of the wind turbine model. Plot (c): Three-phase current $\underline{i}_{\mathrm{t,w}}^{(\mathrm{abc})}$; Plot (b): Active current $\hat{i}_{\mathrm{t,w_d}}$ (blue) and reactive current $\hat{i}_{\mathrm{t,w_q}}$ (green).

LVRT test by VSC with constant power output from wind turbine model

In this point, the response of a wind turbine that does not have implemented a LVRT control strategy is studied. For this experiment, the wind turbine is operating with a power reference of 0.6 pu. The voltage is controlled at 1 pu and reduced to 0.6 pu for 1.3 s, followed by a recovery ramp for 700 ms towards 1 pu. The results of this experiment are given in Fig. 6.36.

The resulting PCC voltage is shown in Fig. 6.36(a). The minimum voltage at the PCC is 0.65 pu slightly boosted by the capacitor bank C_{f}. From Fig. 6.36(b) it is possible to observe that the active power is kept at 0.6 pu during the voltage dip. In order to deliver the generated power during a voltage reduction, the active current $\hat{i}_{\mathrm{t,w_d}}$ plotted in Fig. 6.36(d) must increase to its maximum permitted value of 1 pu. The three-phase current $\underline{i}_{\mathrm{t,w}}^{(\mathrm{abc})}$ is shown Fig. 6.36(c). Observe that Fig. 6.36(d) there is no reactive current injection, meaning that the reactive power is set at 0 pu during the hole event.

Finally, at 1.3 s the voltage starts to increase. The active current is decrease accordingly so the power output P_{w} is kept constant during the recovery. The voltage reaches 1 pu at 1.2 s. The active current is set to its pre-fault value of 0.6 pu. The variation of the active current allows that the active power is kept constant during the whole event. This control feature on wind turbines is useful when disconnection of the wind turbine is not allowed if a steady-state voltage reduction is present in the grid.

For further validation of the investigated methodology, field test results of a 4 MW wind turbine is given in the following section.

6.7 Field test

Finally, field test results of a 4 MW FPC offshore wind turbine is presented. The testing equipment is an 8 MW back-to-back HVDC station placed in Gothenburg harbour. A picture of the actual wind turbine is given in Fig. 6.37. The wind turbine is located at the edge of the land in proximity to the sea. The wind turbine receives offshore wind coming from the northern part of Denmark. The tests have been performed on the 13th of January 2015.

Fig. 6.37 4 MW FPC “Big Glenn” wind turbine.

(a) (b)

Fig. 6.38 Back-to-back HVDC Station in Gothenburg. Plot (a): collector-VSC station. Plot (b): coupling inductor and AC filters.

Two case scenarios has been tested: case 1 corresponds to a voltage fluctuation where the voltage is reduced from 1 pu to 0.95 pu for 100 ms; case 2 corresponds to a voltage dip of 0.65 pu for 100 ms. Here, only the three-phase voltages and currents at the PCC are sampled. The instantaneous active and reactive power are calculated afterwards. Technical data of the testing setup is given in Table 6.3 and the schematic of interconnection of the wind turbine with the test equipment is shown in Fig. 4.1. The wind turbine is operating at full active power production, and the PCC voltage is controlled in open-loop, meaning that the voltage variation is applied directly at the terminals of the collector-VSC.

TABLE 6.3. PARAMETERS OF FIELD TEST SETUP.

Base values	10 kV, 8.0 MVA
Wind turbine rating	0.5 pu
Testing equipment rating	1.0 pu

In Fig. 6.39 is shown the results for the first case scenario. The three-phase PCC voltage is shown in Fig. 6.39(a). At 0.05 s the voltage is reduced from 1 pu to 0.95 pu and is maintained for 100 ms. At 0.15 s the voltage is brought back to 1 pu with a ramp function. In order to maintain constant power production during to the reduction in voltage, the wind turbine increases the magnitude of the current, as depicted in Fig. 6.39(b). Finally, the injected active and reactive power is given in Fig. 6.39(c). During the voltage variation, the wind turbine maintains its active power set point, injecting a steady 0.5 pu of active power into the grid. The reactive power is varied due to the reduction of voltage across the AC branch between the wind turbine and the testing equipment. In this setup the back-to-back HVDC system includes a filter bank in both of their converter terminals, therefore, it is expected that a certain amount of reactive power is varied when the system voltage is reduced.

In the next scenario, the PCC voltage is reduced to 0.65 pu and maintained for 100 ms while the wind turbine is producing nominal active power. A shown Fig. 6.40(a), the three-phase PCC

voltage is dropped at 0.05 s. It can be seen from Fig. 6.40(b) that the wind turbine takes 20 ms to increase its output current after detecting the voltage dip. However, the active power is decreased to 0.25 pu because of the abrupt reduction of the voltage and it is restored to nominal value once the current has increased, as depicted in Fig. 6.40(c) . At 0.075 s it is possible to observe a transient in both the current and the voltage. In figure Fig. 6.41 the voltage and current waveforms are zoomed at the moment of the dip. Observe that the frequency of the resonance is in proximity to 400 Hz.

In Fig. 5.1 it is shown the reduced model of the test equipment. The capacitor C_{f} represents the total capacitance of the filter bank shown in the full model given in Fig. 4.2. By calculating C_{f} and the series inductor L_{f} with the parameters given in Table 4.1, the resonant frequency between these two objects is also in proximity to 400 Hz. Observe in Fig. 6.41(a) that an extremely sharp voltage variation of approximately 0.05 [pu/ms] is applied at the PCC at 0.06 s. For this reason, as discussed in Section 6.2.1, an oscillatory response of the system is expected. Therefore, the oscillations in the voltage and current shown in Fig. 6.41(a) and Fig. 6.41(b), respectively, can be explained by a possible interaction between the filter inductance and the capacitive element of the filter bank of the on-site testing equipment.

The transient lasts for 10 ms and the wind turbine manages to control its current output during the voltage dip. The wind turbine power is maintained in 0.5 pu in steady-state, while the reactive power is varied. Finally, in Fig. 6.40(c) it is possible to observe that during the voltage dip the wind turbine is injecting reactive power into the grid. As seen from the previous experiment, the reactive power exchange at the terminals of the collector-VSC only due to the filter is 0.1 pu. The wind turbine injects an additional 0.1 pu of reactive power when detecting the voltage dip at its terminals. Therefore, a total of 0.2 pu is maintained until the voltage is increased back to 1 pu.

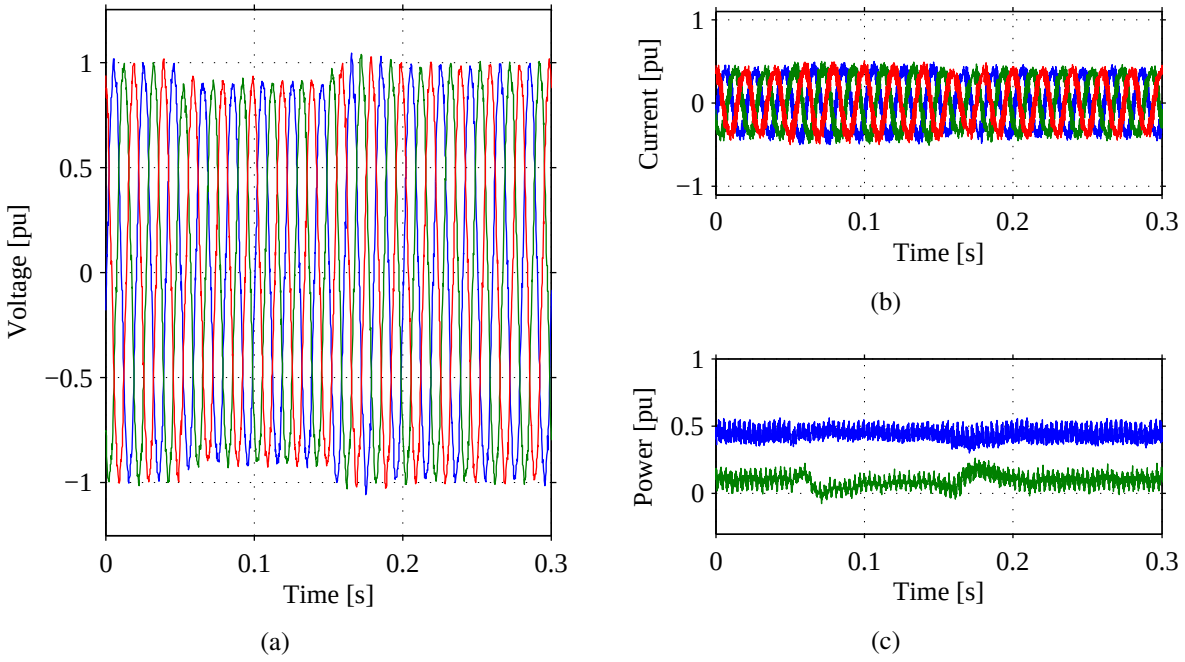

Fig. 6.39 Wind turbine under voltage dip test, case 1. Plot (a): three-phase voltage; Plot (b): three-phase current; Plot (c): active (blue) and reactive (green) power.

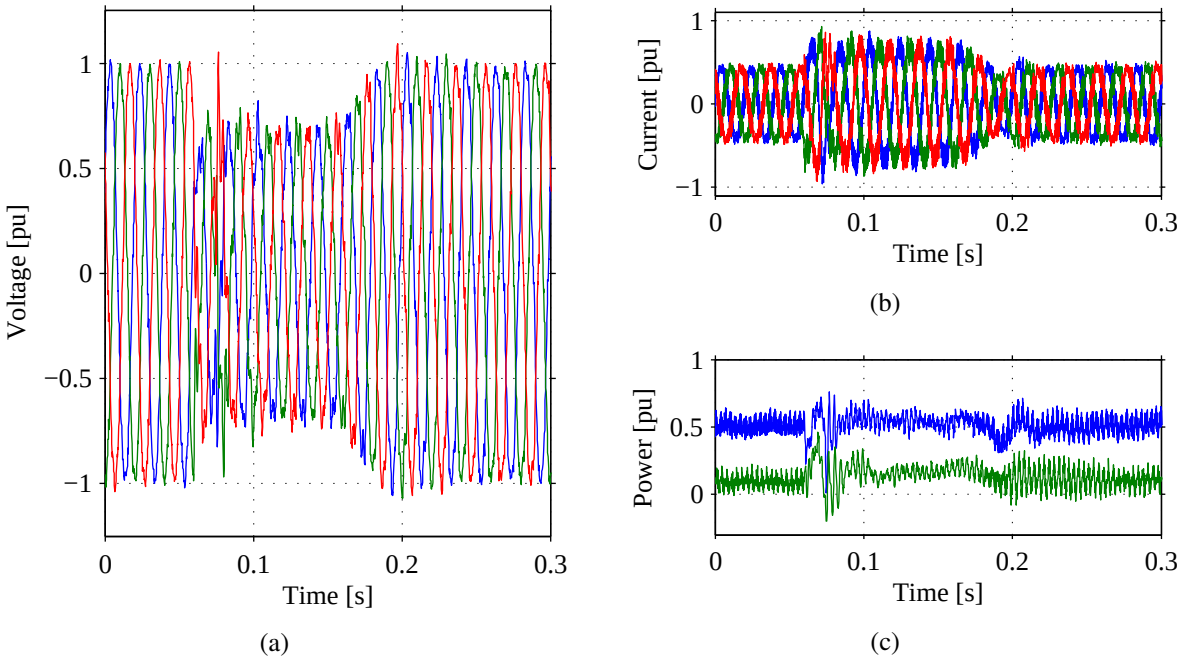

Fig. 6.40 Wind turbine under voltage dip test, case 2. Plot (a): three-phase voltage; Plot (b): three-phase current; Plot (c): active (blue) and reactive (green) power.

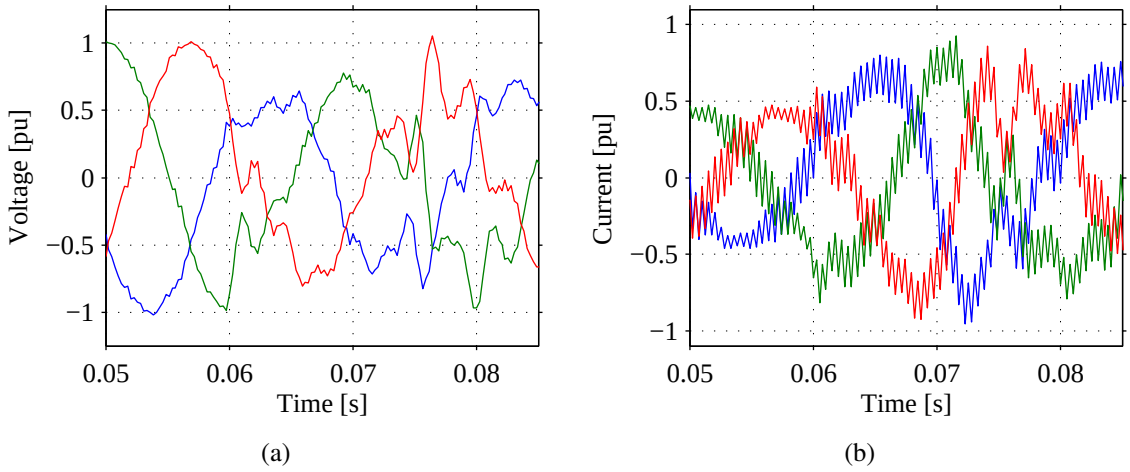

Fig. 6.41 Transient response of the test equipment. Plot (a): zoom in the three-phase voltage; Plot (b): zoom in the three-phase current.

As expected, the average value of the reactive power after the dip is 0.1 pu.

6.8 Conclusions

In this chapter, the investigated grid code testing methodology has been validated through time-domain simulations. Here, three different topologies for PCC voltage control have been compared. On one side, the open loop control shows to be a simple and robust way of controlling

the PCC voltage by means of controlling directly the terminal voltage of the collector VSC. In order to avoid an undesired oscillatory response of the system, an appropriate ramp-rate must be selected when varying the converter voltage. On the other side, the PI-based close loop controller seems to effectively control the PCC voltage while taking care of the filter losses and at the same time controlling the current that flows between the collector converter and the PCC, thus, preventing an oscillatory response of the system. Moreover, focused on the dynamics of both wind turbine and testing equipment during the test, an analysis of the performance of the overall system has been given. The open-loop and P-based and PI-based close-loop controllers have been verified through simulation and a control algorithm to emulate different grid scenarios has been devised and also verified by simulations. The use of PI-based controller gives a smooth response when controlling the PCC voltage, while the open-loop control is more simple and easy to implement, especially when testing for unbalanced voltage dips.

For this reason, the use of open-loop controller has been validated through laboratory experiment. The laboratory result also validates the derived current control, DC voltage control and LVRT control strategy of the modelled wind turbine. Moreover, the open-loop controller is found to be robust in controlling the voltage across the AC-link. If special attention is paid to the selection of ramp-rates when controlling the voltage in open-loop, the PCC voltage can be controlled smoothly without undesired transients, as shown in the laboratory results. Finally, field test results of a 4 MW wind turbine and 8 MW testing equipment has been included, providing invaluable experience on using VSC-based testing equipment for LVRT test of wind turbines. Here, the open-loop control has been implemented and a fast variation in voltage has been applied at the PCC, resulting in an oscillatory response of the system.

Chapter 7

Conclusions and future work

7.1 Conclusions

This thesis has dealt with the use of VSC as a test equipment for grid code testing of wind turbines. In particular, the main focus of the thesis has been on LVRT studies by using a back-to-back VSC as testing device and on the ability of the test equipment in representing a grid with different levels of stiffness.

In order to introduce the wind energy scenario and to give relevance on the issue of testing of wind turbine, the trending of wind park installations has been described in Chapter 2. As wind energy is an inexhaustible source of renewable energy, more and more onshore and offshore wind parks are being installed every day. As a result, the reliability of the electricity grid is increasingly becoming dependent on how well wind turbines are prepared to withstand grid disturbances and in their grid support capabilities. Currently, the testing of wind turbine using impedance-based testing equipment, described in Chapter 3, is limited only to voltage dips and swells. Consequently, other kind of grid conditions remain unverified. For this reason, a new approach of wind turbine testing using VSC-based testing device has been investigated in this thesis.

The electrical modelling of the wind turbine model and of the testing equipment has been presented in Chapter 4. The approach has been to focus on representing the electromagnetic transient dynamic of the testing setup during only voltage disturbances. Therefore, other dynamic behavior of large time constant such as mechanical oscillation were not covered in this thesis. For this reason, only the electrical system of the wind turbine model together with the testing equipment have been considered for simulation and for implementation in the laboratory setup.

Two operating points of the wind turbine have been selected for the stability analysis given in Chapter 5. With focus on the structure of the PCC voltage control of the testing equipment, the stability analysis shows that the minimum order is achieved when the open-loop control is implemented. However, this does not necessarily mean that the system becomes more stable. In fact, simulation and field test results demonstrate that poorly-damped resonances can be easily experienced when testing for voltage dips using open-loop control in test equipment, producing

undesired stress over the power electronic component of the VSC and filters of both the testing device and wind turbine. Close-loop controller, in particular the PI-based controller, increases the order of the system while keeping the dominant poles well-damped. It is also more robust against variations in the bandwidth of the test object.

The dynamic performance of each controller has been discussed in Section 6.2.2. The transients in the AC-system are reduced when the current and the voltage are controlled in close-loop. Similar performance can be achieved with open-loop controller, if special attention on the selection of the ramp-rate when varying the converter voltage is given. Open-loop control is easy to implement, especially when performing unbalanced voltage dip over on the test object. However, better transient response is achieved when PI-based close-loop controller is used.

Furthermore, the impact of parameters unrelated to the test equipment such as bandwidth of the DC voltage control in the wind turbine (placed in the grid-side converter of an FPC wind turbine) or interface impedance between tested object and testing equipment impact the location of the system poles. The investigated close-loop controller of the PCC voltage is found to be more robust against variations of the system parameters. In Chapter 5 it has been demonstrated that the system is stable if these parameters are kept within a certain range. As demonstrated in Chapter 6, the testing equipment is a flexible device that can reproduce a wider variety of voltage profile at the terminals of the tested object. In addition, the close-loop controller provides better damping to the high order transients found when testing for LVRT. Moreover, since the testing equipment is constituted by two VSC in back-to-back configuration, the impact of the testing is constrained between the tested object and the collector-VSC. For this reason, the AC grid is not affected during the test, except for variations in active power provoked by the tested unit. The wind turbine model presented in this thesis has been also verified by simulations, and the current control strategy during LVRT has been validated by laboratory experiment.

Finally, as described in Section 6.7, experimental verification has been carried out on an actual 4 MW FPC wind turbine using a 8 MW 2-level back-to-back VSC system. This provides an experimental validation of the proposed grid code testing methodology, particularly in the case when open-loop controller is used. As expected, an oscillatory response of the system has been observed. The next step on grid code testing by VSC is discussed in the following section.

7.2 Future work

In this thesis, the LVRT test by using VSC has been discussed. The investigated setup has been simplified with focus on the modelling of the electrical system only. This makes the overall analysis easy to conduct. The simplifications adopted in this thesis has been first: to exclude the dynamics of the mechanical system of the wind turbine model, and second, to focus only on the AC link between the wind turbine and the testing equipment for the stability analysis. A next step in this work is then to include the mechanical system of the wind turbine. A two-mass model could be sufficient to represent the impact of the mechanic system into the transferred power between generator and grid. In addition, wind turbine generators with power greater than 4 MW can posses a double winding in the stator [6], meaning that the so called full size converter can be constituted by two set of half-size back-to-back VSC in parallel, before reaching, for instance,

a three-winding step-up transformer at the output of the wind turbine. The introduction of these sub-systems can lead to a different result in the LVRT test of the simulated setup. Thus, further experimental verification is needed to assess the evaluation of the grid code testing methodology investigated in this Thesis.

With focus on the test equipment, the use of VSC-based testing equipment brings more possibilities of tests that can be performed. As explained in Section 3.6.3, in order to investigate the frequency response of the electromechanical system that constitute a drive train, frequency characterization of wind turbines can be performed by introducing asynchronous frequency content into the applied voltage while observing the equivalent admittance at the PCC. In order to conduct these experiments, a simple open-loop PCC voltage control can be useful. This information is of importance, especially when interconnecting a wind power plant with the grid through VSC-HVDC systems. The next step on this analysis would be to investigate if the use of close-loop controller at the collector-VSC can increase the damping of the possible resonances found in the tested wind turbine.

Weak grid simulation by VSC can be used for testing voltage control capabilities on wind turbines. Similarly, further analysis on frequency support capability of wind turbines can be carried out by performing a test where the frequency applied at the PCC is varied. In the same way, a proper emulation strategy of the synchronous generator including its poor mechanical damping can be implemented in the PCC voltage control of the VSC. Here, power oscillation damping capability of wind turbines can also be tested.

References

[1] F. Blaabjerg and K. Ma, "Future on power electronics for wind turbine systems," *Emerging and Selected Topics in Power Electronics, IEEE Journal of*, vol. 1, no. 3, pp. 139–152, Sept 2013.

[2] Global Wind Energy Council (GWEC), *Global Wind Energy Report Annual Market Update Update 2013*. Global Wind Energy Council (GWEC), 2014. [Online]. Available: http://www.gwec.net/

[3] EWEA, *Wind in Power, 2013 European statistics*. The European Wind Energy Association, Feb. 2014. [Online]. Available: http://www.ewea.org/

[4] EWEA, *The European offshore wind industry, key trends and statistics 2013*. The European Wind Energy Association, Jan. 2014. [Online]. Available: http://www.ewea.org/

[5] EWEA, *The European offshore wind industry, key trends and statistics 2012*. The European Wind Energy Association, Jan. 2013. [Online]. Available: http://www.ewea.org/

[6] Joachim Härsjö, *Modeling of PMSM Full Power Converter Wind Turbine with Turn-to-Turn Fault*. Gothenburg, Sweden: Chalmers University of Technoology, 2014. [Online]. Available: http://www.chalmers.net/

[7] Gastón O. Suvire, *Wind Farm - Technical Regulations, Potential Estimation and Siting Assessment*. InTech, 2011.

[8] Abram Perdana, *Dynamic Models of Wind Turbines*. Gothenburg, Sweden: Chalmers University of Technoology, 2014. [Online]. Available: http://www.chalmers.net/

[9] N. Espinoza, M. Bongiorno, and O. Carlson, "Grid code testing of full power converter based wind turbine using back-to-back voltage source converter system," in *EWEA 2013 Annual Event Conference Proceedings*, Feb. 2013. [Online]. Available: http://www.ewea.org/

[10] M. Tsiliand and S. Papathanassiou, "A review of grid code technical requirements for wind farms," in *IET Renewable Power Generation*, vol. 3, no. 3, Sept. 2009, pp. 308 – 332.

[11] M. Mohseni and S. M. Islam, "Review of international grid codes for wind power integration: Diversity, technology and a case for global standard," in *Renewable and*

Sustainable Energy Reviews, vol. 16, no. 6, 2012, pp. 3876–3890. [Online]. Available: http://www.sciencedirect.com

[12] Andreas Petersson, *Analysis, Modeling and Control of Doubly-Fed Induction Generators for Wind Turbines*. Gothenburg, Sweden: Chalmers University of Technoology, 2005. [Online]. Available: http://www.chalmers.net/

[13] M. Bongiorno and T. Thiringer, "A generic dfig model for voltage dip ride-through analysis," *Energy Conversion, IEEE Transactions on*, vol. 28, no. 1, pp. 76–85, Mar. 2013.

[14] A. Beeckmann, V. Diedrichs, and S. Wachtel, "Evaluation of wind energy converter behavior during network faults - limitations of low voltage ride through test and interpretation of the test results," in *9th International Workshop on Large-Scale Integration of Wind Power into Power Systems as well as on Transmission Networks for Offshore Wind Power Plants*, Oct. 2010.

[15] IEC 61400-21 ed2.0, *Wind turbines - Part 21: Measurement and assessment of power quality characteristics of grid connected wind turbines*. Germany: International Electrotechnical Commission, 2008.

[16] M. Molina, J. A. Suul, and T. Undeland, "A simple method for analytical evaluation of lvrt in wind energy for induction generators with statcom or svc," in *Power Electronics and Applications, 2007 European Conference on*, Sept. 2007, pp. 1–10.

[17] E.ON, *Grid Code - High and Extra High Voltage*. Bayreuth, Germany: E.ON Nets GmbH, April. 2006.

[18] ——, *Requirements for Off-Shore Grid Connection in the E.On Nets Network*. Bayreuth, Germany: E.ON Nets GmbH, April. 2008.

[19] National Grid, *The Grid Code, Issue 3, Revision 23, 30th October 2007*. National Grid Electricity Transmission plc, October 2007.

[20] Red Electrica de España, *Resolution-P.O.12.3-Requisitos de respuesta frente a huevos de tensión de las instalaciones de producción de régimen especial*. REE, March 2006.

[21] EirGrid, *EirGrid Grid Code Version 4.0*. EirGrid, December 2011.

[22] ENERGINETDK, *Technical regulation 3.2.5 for wind power plants with a power output greater than 11 kW*. Energinet.dk, September 2010.

[23] Svenska Kraftnät, *The Business Agency Svenska kraftnats regulations and general advice concerning the reliable design of production plants*. Svenska Kraftnat, July 2005.

[24] Nordel, *Nordic Grid Code 2007, Nordic Collection of Rules*. Nordic Grid, Januray 2007.

[25] ENTSO-E, *ENTSO-E Network Code for Requirements for Grid Connection Applicable to all Generators*. ENTSO-E, June 2013.

[26] M. Altın, O. Göksu, R. Teodorescu, P. Rodriguez, B. B. Jensen, and L. Helle, "Overview of recent grid codes for wind power integration," in *Optimization of Electrical and Electronic Equipment (OPTIM), 2010 12th International Conference on*, Sept. 2010, pp. 1152–1160.

[27] I. Erlich and U. Bachmann, "Grid code requirements concerning connection and operation of wind turbines in germany," in *Power Engineering Society General Meeting, 2005. IEEE*, vol. 2, June 2005, pp. 1253–1257.

[28] I. Martinez and D. Navarro, "Gamesa dac converter: the way for ree grid code certification," in *Power Electronics and Motion Control Conference, 2008. EPE-PEMC 2008. 13the*, Sept. 2008, pp. 437–443.

[29] Y. Yang, F. Blaabjerg, and Z. Zou, "Benchmarking of voltage sag generators," in *IECON 2012 - 38th Annual Conference on IEEE Industrial Electronics Society*, Oct 2012, pp. 943–948.

[30] C. Saniter, J. Janning, and A. Bocquel, "Test bench for grid code simulations for multi-mw wind turbines," in *Power Electronics and Applications, 2007 European Conference on*, Sept 2007, pp. 1–10.

[31] C. Wessels, R. Lohde, and F. Fuchs, "Transformer based voltage sag generator to perform lvrt and hvrt tests in the laboratory," in *Power Electronics and Motion Control Conference (EPE/PEMC), 2010 14th International*, Sept 2010, pp. T11–8–T11–13.

[32] J. C. Ausin, D. N. Gevers, and B. Andresen, "Fault ride-through capability test unit for wind turbines," *Wind Energy*, vol. 11, no. 1, pp. 3–12, 2008. [Online]. Available: http://dx.doi.org/10.1002/we.255

[33] S. Hu, J. Li, and H. Xu, "Comparison of voltage sag generators for wind power system," in *Power and Energy Engineering Conference, 2009. APPEEC 2009. Asia-Pacific*, March 2009, pp. 1–4.

[34] I. J. Gabe, H. Grundling, and H. Pinheiro, "Design of a voltage sag generator based on impedance switching," in *IECON 2011 - 37th Annual Conference on IEEE Industrial Electronics Society*, Nov 2011, pp. 3140–3145.

[35] W. Jian, H. Zhihao, X. Dianguo, and H. Ke, "An experimental research on comparison of two kinds of voltage sag generators," in *Power Electronics and Motion Control Conference (IPEMC), 2012 7th International*, vol. 4, June 2012, pp. 2784–2788.

[36] M. Diaz and R. Cardenas, "Matrix converter based voltage sag generator to test lvrt capability in renewable energy systems," in *Ecological Vehicles and Renewable Energies (EVER), 2013 8th International Conference and Exhibition on*, March 2013, pp. 1–7.

[37] R. Lohde and F. Fuchs, "Laboratory type pwm grid emulator for generating disturbed voltages for testing grid connected devices," in *Power Electronics and Applications, 2009. EPE '09. 13th European Conference on*, Sept 2009, pp. 1–9.

[38] R. Pollanen, L. Kankainen, M. Paakkonen, J. Ollila, and S. Strandberg, "Full-power converter based test bench for low voltage ride-through testing of wind turbine converters," in *Power Electronics and Applications (EPE 2011), Proceedings of the 2011-14th European Conference on*, Aug 2011, pp. 1–10.

[39] J. He and Y. W. Li, "Generalized closed-loop control schemes with embedded virtual impedances for voltage source converters with lc or lcl filters," *Power Electronics, IEEE Transactions on*, vol. 27, no. 4, pp. 1850–1861, Apr. 2012.

[40] Y. Liu and Z. Li, Chen, "A flexible power control method of vsc-hvdc link for the enhancement of effective short-circuit ratio in a hybrid multi-infeed hvdc system," *Power Systems, IEEE Transactions on*, vol. 28, no. 2, pp. 1568–1581, May 2013.

[41] Göteborg Energi AB. Göteborg wind lab @ONLINE. [Online]. Available: http://www.goteborgwindlab.se

[42] M. Bongiorno and J. Svensson, "Voltage dip mitigation using shunt-connected voltage source converter," *Power Electronics, IEEE Transactions on*, vol. 22, no. 5, pp. 1867–1874, Sep. 2007.

[43] L. Harnefors, M. Bongiorno, and S. Lundberg, "Input-admittance calculation and shaping for controlled voltage-source converters," *Industrial Electronics, IEEE Transactions on*, vol. 54, no. 6, pp. 3323–3334, Dec 2007.

[44] R. Ottersen, "On control of back-to-back converters and sensorless induction machine drivs," Ph.D. dissertation, Chalmers University of Technology, Gothenburg, Sweden, June 2003.

[45] M. R. Centre. Pscad/emtdc v4.2. [Online]. Available: https://hvdc.ca/pscad/

[46] Wolfram. Wolfram mathematica 8. [Online]. Available: https://www.wolfram.com/

[47] I. The MathWorks. Matlab r2011a/r2013b. [Online]. Available: http://se.mathworks.com/

[48] A. Uphues, K. Notzold, R. Wegener, S. Soter, and R. Griessel, "Inverter based voltage sag generator with pr-controller," in *IECON 2012 - 38th Annual Conference on IEEE Industrial Electronics Society*, Oct 2012, pp. 1037–1042.

[49] S. Seman, J. Niiranen, R. Virtanen, and J.-P. Matsinen, "Low voltage ride-through analysis of 2 mw dfig wind turbine - grid code compliance validations," in *Power and Energy Society General Meeting - Conversion and Delivery of Electrical Energy in the 21st Century, 2008 IEEE*, July 2008, pp. 1–6.

[50] J. He and Y. W. Li, "Analysis, design, and implementation of virtual impedance for power electronics interfaced distributed generation," *Industry Applications, IEEE Transactions on*, vol. 47, no. 6, pp. 2525–2538, Nov./Dec. 2011.

[51] R. Zeng, H. Nian, and P. Zhou, "A three-phase programmable voltage sag generator for low voltage ride-through capability test of wind turbines," in *Energy Conversion Congress and Exposition (ECCE), 2010 IEEE*, Sept 2010, pp. 305–311.

[52] K. Daychosawang and Y. Kumsuwan, "Balanced and unbalanced three-phase voltage sag generator for testing electrical equipment," in *Electrical Engineering/Electronics, Computer, Telecommunications and Information Technology (ECTI-CON), 2014 11th International Conference on*, May 2014, pp. 1–6.

[53] M. Bongiorno and J. Svensson, "Voltage dip mitigation using shunt-connected voltage source converter," in *Power Electronics Specialists Conference, 2006. PESC '06. 37th IEEE*, June 2006, pp. 1–7.

[54] C. Liu, D. Xu, N. Zhu, F. Blaabjerg, and M. Chen, "Dc-voltage fluctuation elimination through a dc-capacitor current control for dfig converters under unbalanced grid voltage conditions," *Power Electronics, IEEE Transactions on*, vol. 28, no. 7, pp. 3206–3218, July 2013.

[55] dSPACE GmbH. dspace system. [Online]. Available: http://www.dspace.com

[56] M. Beza and M. Bongiorno, "Improved discrete current controller for grid-connected voltage source converters in distorted grids," in *Energy Conversion Congress and Exposition (ECCE), 2012 IEEE*, Sept 2012, pp. 77–84.

[57] M. Beza, "Power system stability enhancement using shunt-connected power electronic devices with active power injection capability," Ph.D. dissertation, Chalmers University of Technology, Gothenburg, Sweden, Januaey 2015.

References

Appendix A

Transformations for Three-phase Systems

This appendix reports necessary transformations to calculate voltage vectors from three-phase quantities and vice versa. Expressions of the voltage vector both in the fixed and rotating reference frames are given in the general case of unsymmetrical three-phase quantities.

A.1 Transformation of three-phase quantities into vectors

A three-phase positive system constituted by the three quantities $v_1(t)$, $v_2(t)$ and $v_3(t)$ can be transformed into a vector in a complex reference frame, usually called $\alpha\beta$-frame, by applying the transformation defined by

$$\underline{v}(t) = v_\alpha + \mathrm{j}v_\beta = K\left[v_1(t) + v_2 e^{\mathrm{j}\frac{2}{3}\pi}(t) + v_3 e^{\mathrm{j}\frac{4}{3}\pi}(t)\right] \tag{A.1}$$

where the factor K is equal to $\sqrt{3/2}$ or $3/2$ to ensure power invariance or voltage invariance, respectively, between the two systems. Equation (A.1) can be expressed as a matrix equation as follows

$$\begin{bmatrix} v_\alpha(t) \\ v_\beta(t) \end{bmatrix} = \mathbf{C}_{23} \begin{bmatrix} v_1(t) \\ v_2(t) \\ v_3(t) \end{bmatrix} \tag{A.2}$$

where, using power-invariant transformation, the matrix $\mathbf{C}_{23}$ is equal to

$$\mathbf{C}_{23} = \begin{bmatrix} \sqrt{\frac{2}{3}} & \frac{-1}{\sqrt{6}} & \frac{-1}{\sqrt{6}} \\ 0 & \frac{1}{\sqrt{2}} & \frac{-1}{\sqrt{2}} \end{bmatrix} \tag{A.3}$$

The inverse transformation, assuming no zero-sequence, is given by

$$\begin{bmatrix} v_1(t) \\ v_2(t) \\ v_3(t) \end{bmatrix} = \mathbf{C}_{32} \begin{bmatrix} v_\alpha(t) \\ v_\beta(t) \end{bmatrix} \tag{A.4}$$

where

$$\mathbf{C}_{32} = \begin{bmatrix} \sqrt{\frac{2}{3}} & 0 \\ \frac{-1}{\sqrt{6}} & \frac{1}{\sqrt{2}} \\ \frac{-1}{\sqrt{6}} & \frac{-1}{\sqrt{2}} \end{bmatrix} \tag{A.5}$$

A.2 Transformation between fixed and rotating coordinate systems

Let the vectors $\underline{v}(t)$ and $\underline{u}(t)$ rotate in the $\alpha\beta$-frame with the angular frequency $\omega(t)$ in the positive (counter-clockwise) direction. If the vector $\underline{u}(t)$ is taken as the d-axis of a dq-frame that rotates in the same direction with the same angular frequency $\omega(t)$, both vectors will appear as fixed vectors in that frame. The components of $\underline{v}(t)$ in the dq-frame are thus given by the projections of the vector on the direction of $\underline{u}(t)$ and on the orthogonal direction, as illustrated in Fig.A.1.

The transformation can be written in vector form as

$$\underline{v}^{(dq)}(t) = \underline{v}^{(\alpha\beta)}(t)e^{-\mathrm{j}\theta(t)} \tag{A.6}$$

with the angle $\theta(t)$ in Fig.A.1 given by

$$\theta(t) = \theta_0 + \int_0^t \omega(\tau)d\tau \tag{A.7}$$

The inverse transformation, from the rotating dq-frame to the fixed $\alpha\beta$-frame is defined by

$$\underline{v}^{(\alpha\beta)}(t) = \underline{v}^{(dq)}(t)e^{\mathrm{j}\theta(t)} \tag{A.8}$$

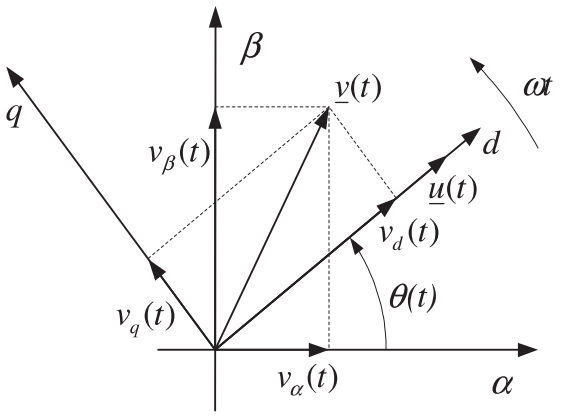

Fig. A.1 Relation between $\alpha\beta$-frame and dq-frame.

The components in the dq-frame can be determined from Fig.A.1. In matrix form, the transformation from the fixed $\alpha\beta$-frame to the dq-frame can be written as

$$\begin{bmatrix} v_d(t) \\ v_q(t) \end{bmatrix} = \mathbf{R}(-\theta(t)) \begin{bmatrix} v_\alpha(t) \\ v_\beta(t) \end{bmatrix} \tag{A.9}$$

while the inverse is given by

$$\begin{bmatrix} v_\alpha(t) \\ v_\beta(t) \end{bmatrix} = \mathbf{R}(\theta(t)) \begin{bmatrix} v_d(t) \\ v_q(t) \end{bmatrix} \tag{A.10}$$

where the projection matrix is

$$\mathbf{R}(\theta(t)) = \begin{bmatrix} \cos(\theta(t)) & -\sin(\theta(t)) \\ \sin(\theta(t)) & \cos(\theta(t)) \end{bmatrix} \tag{A.11}$$

A.3 Voltage vectors for unsymmetrical three-phase systems

The phase voltages for a three-phase system can be written as

$$e_{\mathrm{a}}(t) = \widehat{e}_{\mathrm{a}}(t)\cos\left[\omega(t) - \varphi_{\mathrm{a}}\right] \tag{A.12}$$

$$e_{\mathrm{b}}(t) = \widehat{e}_{\mathrm{b}}(t)\cos\left[\omega(t) - \frac{2}{3}\pi - \varphi_{\mathrm{b}}\right] \tag{A.13}$$

$$e_{\mathrm{c}}(t) = \widehat{e}_{\mathrm{c}}(t)\cos\left[\omega(t) - \frac{4}{3}\pi - \varphi_{\mathrm{c}}\right] \tag{A.14}$$

where $\widehat{e}_{\mathrm{a}}(t)$ and φ_{a} are the amplitude and the phase angle of the phase voltage $e_{\mathrm{a}}(t)$, while ω is the angular frequency of the system.

If the voltage amplitude of the three phases are unequal, the resulting voltage vector $\underline{u}^{(\alpha\beta)}(t)$ in the fixed $\alpha\beta$-coordinate system can be expressed as the sum of two vectors rotating in opposite directions and interpreted as positive- and negative-sequence component vectors

$$\underline{u}^{(\alpha\beta)}(t) = E_{\mathrm{p}} e^{\mathrm{j}(\omega t + \varphi_{\mathrm{p}})} + E_{\mathrm{n}} e^{-\mathrm{j}(\omega t + \varphi_{\mathrm{n}})} \tag{A.15}$$

where E_{p} and E_{n} are the amplitudes of the positive and negative voltage vectors, respectively, and the corresponding phase angles are denoted by φ_{p} and φ_{n}.

When transforming the voltage vector $\underline{u}^{(\alpha\beta)}$ from the fixed $\alpha\beta$-plane to the rotating dq-coordinate system, two rotating frames can be used, accordingly. These two frames are called positive and negative synchronous reference frames (SRFs) and are denoted as dqp- and dqn-plane: the positive SRF rotates counterclockwise with the angular frequency, while the negative SRF rotates clockwise with the same frequency. These two frames can be defined by the following transformations

$$\underline{u}^{(dqp)}(t) = e^{-\mathrm{j}\theta(t)} \underline{u}^{(\alpha\beta)}(t) \tag{A.16}$$

$$\underline{u}^{(dqn)}(t) = e^{\mathrm{j}\theta(t)} \underline{u}^{(\alpha\beta)}(t) \tag{A.17}$$

From the latter, it is straightforward to understand that a positive-sequence component corresponds to a DC-component (zero frequency) in the positive SRF, while a negative-sequence component corresponds to a vector that rotates with 100 Hz clockwise in the positive SRF

$$\underline{u}_{\mathrm{n}}^{(dqp)}(t) = e^{-\mathrm{j}\theta(t)} e^{-\mathrm{j}\theta(t)} \underline{u}^{(dqn)}(t) = e^{\mathrm{j}2\theta(t)} \underline{u}^{(dqn)}(t) \tag{A.18}$$

An analogous relation can be derived for a positive-sequence component in the negative SRF.